Effect of tool geometry on ultraprecision machining of soft-brittle materials: a comprehensive review

OPEN ACCESS
IOP Publishing | IMMT
International Journal of Extreme Manufacturing
Int. J. Extrem. Manuf. **5** (2023) 012003 (39pp)
https://doi.org/10.1088/2631-7990/acab3f

Topical Review

Effect of tool geometry on ultraprecision machining of soft-brittle materials: a comprehensive review

Weihai Huang and Jiwang Yan*

Department of Mechanical Engineering, Faculty of Science and Technology, Keio University, 3-14-1 Hiyoshi, Kohoku-ku, Yokohama 223-8522, Japan

E-mail: yan@mech.keio.ac.jp

Received 26 July 2022, revised 20 October 2022
Accepted for publication 12 December 2022
Published 19 January 2023

Abstract

Brittle materials are widely used for producing important components in the industry of optics, optoelectronics, and semiconductors. Ultraprecision machining of brittle materials with high surface quality and surface integrity helps improve the functional performance and lifespan of the components. According to their hardness, brittle materials can be roughly divided into hard-brittle and soft-brittle. Although there have been some literature reviews for ultraprecision machining of hard-brittle materials, up to date, very few review papers are available that focus on the processing of soft-brittle materials. Due to the 'soft' and 'brittle' properties, this group of materials has unique machining characteristics. This paper presents a comprehensive overview of recent advances in ultraprecision machining of soft-brittle materials. Critical aspects of machining mechanisms, such as chip formation, surface topography, and subsurface damage for different machining methods, including diamond turning, micro end milling, ultraprecision grinding, and micro/nano burnishing, are compared in terms of tool-workpiece interaction. The effects of tool geometries on the machining characteristics of soft-brittle materials are systematically analyzed, and dominating factors are sorted out. Problems and challenges in the engineering applications are identified, and solutions/guidelines for future R&D are provided.

Keywords: ultraprecision machining, soft-brittle materials, ductile machining, tool geometries, material removal mechanisms, surface integrity

1. Introduction

In the industries of optics, optoelectronics, and semiconductors, many important parts are made of brittle materials. One of the most widely known brittle material is single-crystal silicon, due to its wide technological applications. Single-crystal silicon, with a hardness of 10 GPa, is usually recognized as a hard-brittle material [1]. Similarly, most advanced ceramics [2], glasses, and semiconductors [3], whose hardness are comparable to or higher than silicon, are also called hard-brittle materials. On the other hand, those brittle materials whose hardness are considerably lower are usually called soft-brittle materials. Typical soft-brittle materials and their mechanical properties are listed in table 1. Soft-brittle materials have various applications in the manufacturing of high value-added products. For example, CdZnTe substrates (see figure 1(a)), which have a high electro-optic coefficient and transparency

* Author to whom any correspondence should be addressed.

2631-7990/23/012003+39$33.00

Table 1. Mechanical properties of typical soft-brittle materials.

Material name	Hardness H (GPa)	Fracture toughness K_c (MPa·m$^{1/2}$)	Application examples
Cadmium zinc telluride (CdZnTe)	0.45–1.8 [9]	0.13 [10]	Radiation detectors [5]
Mercury cadmium telluride (HgCdTe)	0.55 [11]	0.20 [11]	Infrared detectors [12]
Barium fluoride (BaF_2)	0.80 [13]	0.22 [14]	UV/VIS/IR optical systems [15]
Zinc selenide (ZnSe)	0.90–1.43 [16]	0.87 [17]	High-power infrared laser [7], and night vision systems
Potassium dihydrogen phosphate (KDP)	1.32–1.9 [18]	0.22–0.37 [18]	Laser inertial fusion systems [8]
Calcium fluoride (CaF_2)	1.67–1.86 [19, 20]	0.70 [20]	High-end cameras [21]
Zinc sulfide (ZnS)	1.9 [22]	1 [22]	IR laser systems [23]
Polymethyl methacrylate (PMMA)	0.175 [24]	1.08–1.96 [25]	Camera lens for mobile, and intraocular lens
Silicon (Si) [a]	10 [22]	0.6–0.7 [22]	IR optical systems, and semiconductor [26]

[a] Listed as a reference, which is usually called a hard-brittle material.

in the mid-infrared region, can be used for manufacturing infrared focal plane arrays [4]. The x-ray and gamma-ray detectors made of CdZnTe offer many advantages in medical imaging and security inspection [5]. CdZnTe is also the most promising semiconductor alloy for use in the free space optical communication systems [6]. ZnSe lenses (see figure 1(b)) are most commonly used as windows of high-power infrared laser systems and have the potential to serve for night vision systems of autonomous vehicles, because of the wide spectral range and low absorptivity at infrared wavelengths [7]. CaF_2 lenses (see figure 1(c)) show a low dispersion and anomalous dispersion, as well as a broad transmitted wavelength region from vacuum ultraviolet 125 nm to infrared 8 μm. All these properties encourage wide use in astronomy, photography, microscopy, HDTV optics, and medical laser instruments. Potassium dihydrogen phosphate (KDP) lenses are the key optical elements in laser inertial fusion systems (see figure 1(d)), which are used as harmonic frequency converters in the optical path and enable frequency multiplication and optical switching [8]. Amorphous polymers, such as polymethyl methacrylate (PMMA) and polycarbonates, are widely used in camera lenses for cell phones, intraocular lens, and ophthalmic lenses.

To improve the functional performance, reliability, and lifespan of soft-brittle parts, materials must be machined to extremely low surface roughness and high form accuracy without subsurface damage [30]. However, brittle materials are difficult to machine to a high surface quality due to low fracture toughness, which causes surface microfractures. Therefore, machining must be performed in a ductile mode by precisely controlling the material removal at an extremely small scale (e.g. submicron or ten-nanometer level) to create a high-pressure state in the cutting region and limit the tensile stress below the fracture strength of the workpiece material [31, 32]. Consequently, the material plastically deforms in the local machining region rather than fractures. Extensive experimental research has been conducted on ultraprecision machining various brittle materials for several decades. Multiple literature reviews were published which report the characteristics of ultraprecision ductile mode machining of brittle materials [33, 34], effects of laser or vibration assistance [35, 36], physics of contact deformation and fracture of materials [37–39], mechanism clarification via molecular dynamic (MD) simulation [33, 40, 41], chemical mechanical processing of brittle materials [42, 43].

However, most of the aforementioned review papers focused on hard-brittle materials while less emphasis was placed on soft-brittle materials. The machining of soft-brittle materials has some unique features due to the low-hardness nature of the workpiece. For example, abrasives are easily embedded into the machined surface and thus deteriorate the quality of the machined surface [44]. Furthermore, different types of surface scratches and subsurface damages take place [45, 46]. Soft-brittle crystals show strong anisotropy. As illustrated in figure 2, CdZnTe, HgCdTe, ZnSe, and ZnS crystals have cubic zinc blende structures; BaF_2 and CaF_2 crystals have cubic fluorite structures; KDP crystal has a tetragonal structure. The strong material anisotropy adds more challenges to ductile machining. For example, on the (001) plane of KDP, the largest critical depth for ductile machining is ∼162 nm in 45° direction, 2 times the smallest critical depth in 0° direction [47]. On the (100) plane of CaF_2, the largest critical depth for ductile machining is ∼700 nm in 90° direction, 7 times the smallest critical depth in 30° direction [48]. In contrast, on the (100) plane of silicon, the largest critical depth for ductile machining is ∼300 nm in 0° direction, 1.7 times the smallest critical depth in 45° direction [49]. Gao *et al* [50] reviewed the advances in conventional and unconventional machining methods for soft-brittle crystals and discussed the advantages and limitations of each method. However, the machining mechanisms of those processes were not compared in depth. Different tool geometries in various machining processes lead to distinctly different machining characteristics, such as the deformation behavior of material and the formation of surface/subsurface damages. However, the machining conditions for soft-brittle materials are usually selected empirically based on the experience of hard-brittle materials machining. For this reason, a comparative study on the tool's geometrical effects on soft-brittle materials is urgently necessary.

To fill this gap, this article reviews the research on the effects of tool geometry on chip formation, surface integrity, and subsurface damage during ultraprecision machining of

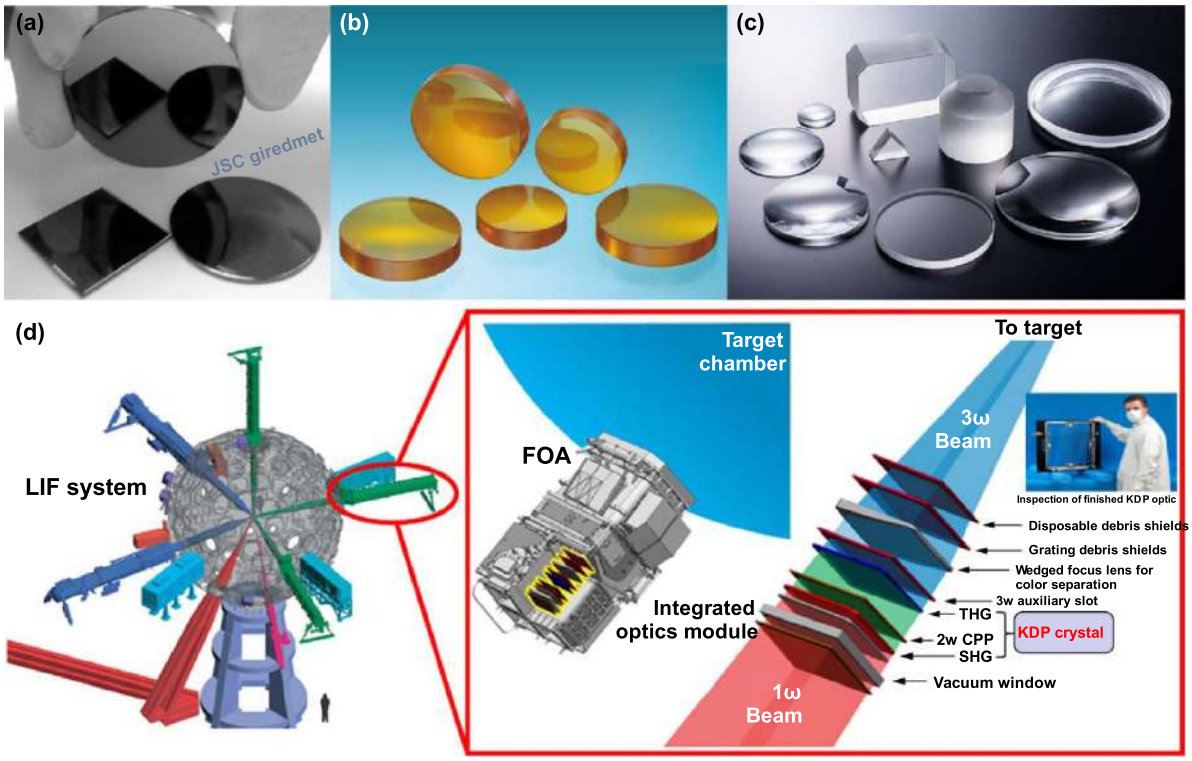

Figure 1. Typical products made of soft-brittle materials: (a) CdZnTe substrates [27] (Reproduced with permission from [27]), (b) ZnSe lenses [28] (Reproduced with permission from [28]), (c) CaF_2 lenses [29] (Reproduced with permission from [29]), and (d) KDP windows in laser inertial fusion (LIF) system [8] (Reprinted by permission from Springer Nature Customer Service Centre GmbH: Springer Nature, The International Journal of Advanced Manufacturing Technology. [8], Copyright 2014).

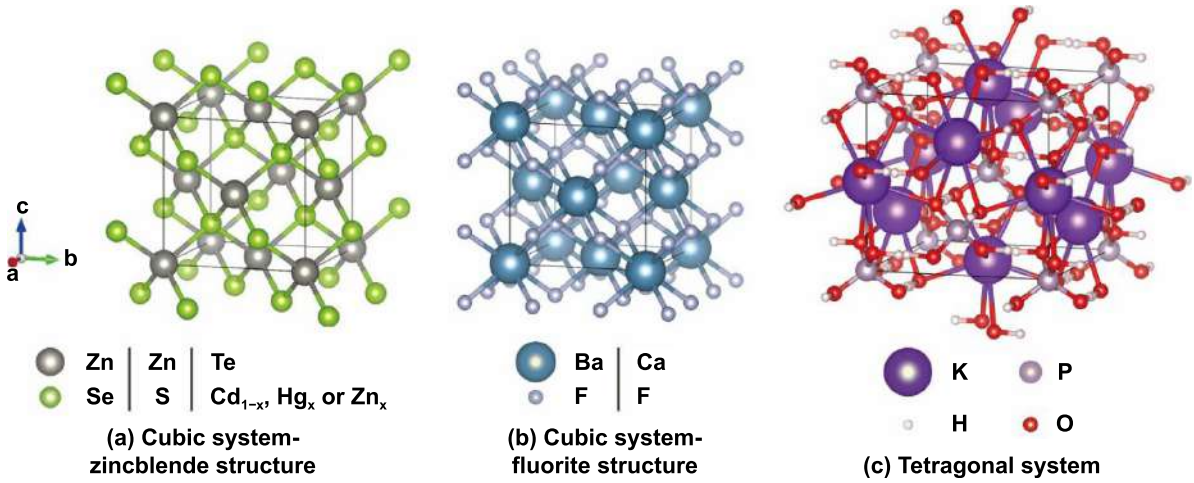

Figure 2. Crystallographic structures of typical soft-brittle materials: (a) cubic zinc blende structures of ZnSe, ZnS, HgCdTe and CdZnTe crystals, (b) cubic fluorite structures of BaF_2 and CaF_2 crystals, (c) tetragonal structure of KDP crystal. Structures drawn in VESTA [51].

soft-brittle materials. Comparisons are made among the mechanisms for four typical machining methods, including diamond turning, micro end milling, ultraprecision grinding, and micro/nano burnishing, as schematically shown in figure 3. A tool featured by a flat rake face with a defined contour is used in diamond turning (see figure 3(a)). The cutting edge is extremely sharp (several tens of nanometers), which is less than or comparable to undeformed chip thickness. Therefore, material removal occurs by shearing and extrusion. In micro end milling (see figure 3(b)), the cutter usually has multiple rake faces with defined contours. The rotation of the tool causes a periodical cut-in and cut-out of the material, leading to an intermittent cutting condition. Due to the different tool materials, the cutting edges of the mill cutter are blunter than the edge of the diamond tool. Thus, the undeformed chip thickness is less than the edge sharpness

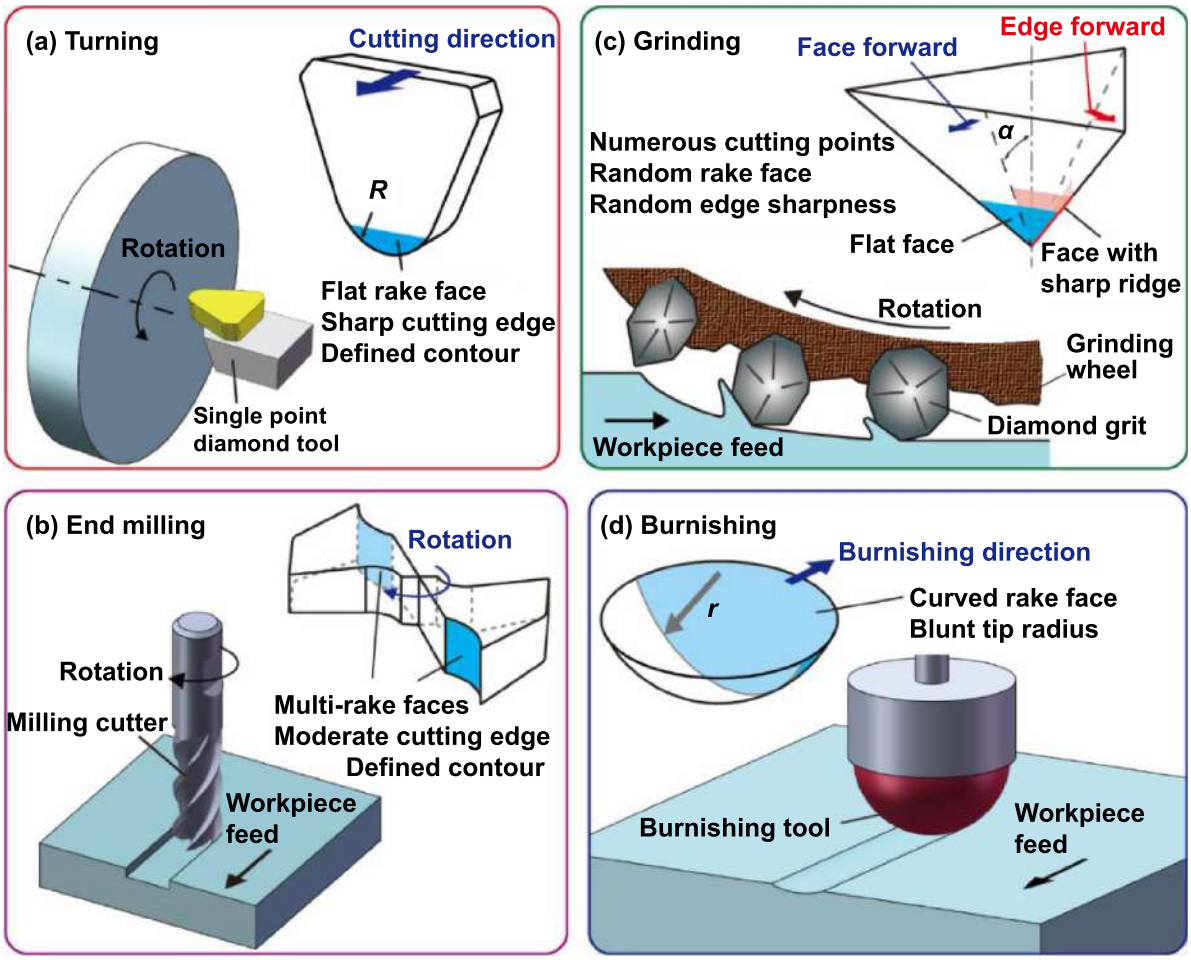

Figure 3. Typical methods for ultraprecision machining of soft-brittle materials.

of the mill cutter, thus, material removal occurs by extrusion and plowing. In ultraprecision grinding (see figure 3(c)), the grinding wheel has a large number of abrasive grits of random shape and orientation. Therefore, the material may come into contact with the flat face, sharp ridge, or round face of abrasive grits. As a result, the material removal behaviors in the grinding process involve shearing, extrusion, plowing, and rubbing, depending on the extent of interaction between the abrasive grits and the workpiece [52]. The surface finish is the statistical result of the above material removal behaviors. In the micro/nano burnishing (see figure 3(d)), the tool is featured by a rounded rake face with an arch contour. The radius of the spherical surface is much larger than the machining depth, making the material deformed by burnishing. The effects of the tool geometry in each of the four types of processes are discussed in sections 2–5, respectively. A comprehensive comparison is made among the four types of processes in section 6 to clarify their common and special features. The differences in material behaviors between soft- and hard-brittle materials are also identified. Finally, in section 7, the problems, challenges, and new possibilities in this technical area are discussed from both scientific research and engineering application aspects, and guidelines for future R&D are provided. This paper helps readers understand the nature of processing soft-brittle materials and select suitable methods and conditions for specific applications.

2. Ultraprecision diamond turning

2.1. Tool shape

Ultraprecision diamond turning is a common method for manufacturing aspherical and freeform surfaces as well as microstructures on brittle materials [53, 54]. Figure 4 presents three typical commercially available diamond tools with different tool shapes, that is, round-nosed tool, straight-nosed tool, and V-shaped tool. The selection of tool shape is important for creating a specific structured surface on workpieces. For example, a round-nosed tool is used for generating a curved surface, such as aspherical or free-form surfaces [55], while a straight-nosed tool is used for cutting flat surfaces or convex aspherical surfaces [56, 57]. When fabricating a Fresnel structure, very straight steps are required. Thus, a round-nosed tool is inappropriate for cutting zones, even if the nose radius is small, because it generates large shadow areas [58, 59], as shown schematically in figure 5(a). In contrast, a V-shaped tool that theoretically has no nose radius can generate Fresnel structures without shadows [60], as shown schematically in figure 5(b).

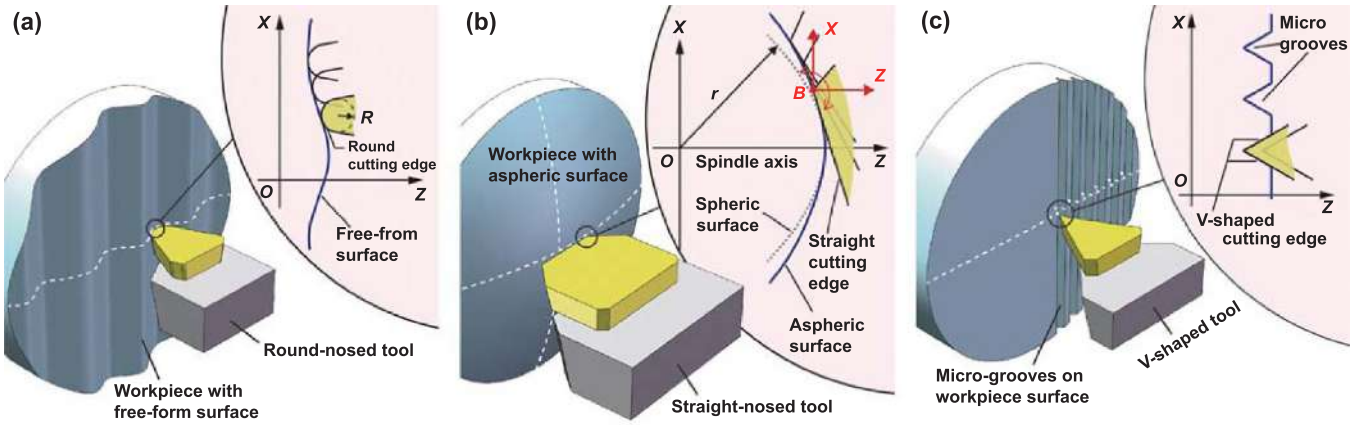

Figure 4. Schematics of different shapes of diamond tools.

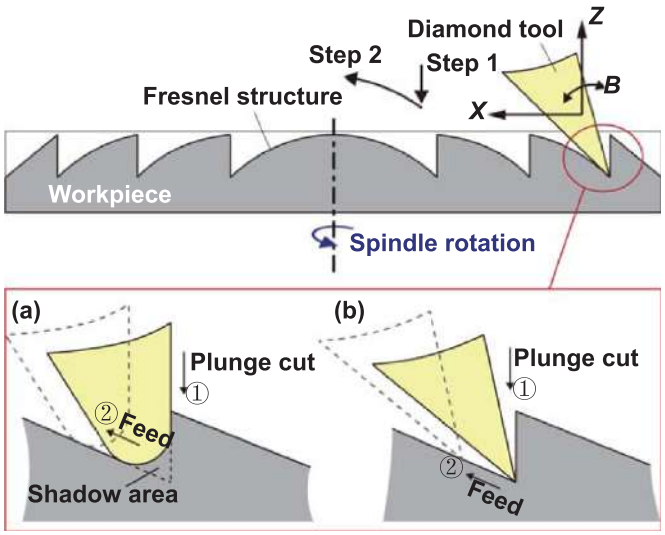

Figure 5. Machining models for the Fresnel structures using (a) a round-nosed tool and (b) a V-shaped tool.

The tool shape affects not only the geometric accuracy of the workpiece but also the machining characteristics. A detailed discussion of each shape of the tool edge is elaborated in the following sub-sections.

2.1.1. Round-nosed tool. In the diamond turning of brittle materials by using a round-nosed tool, the effective chip thickness t_{eff} (i.e. undeformed chip thickness h) varies from zero at the tool center to a maximum value (t_{m}) at the top of the uncut shoulder, as shown in figure 6(a). t_{eff} can be approximately estimated by the following equation [61]:

$$t_{\mathrm{eff}} = f(z+f)/R \tag{1}$$

where f is the feed rate, R is the tool nose radius, and z is the horizontal distance from the tool center to the position where the thickness is estimated.

For the part of the chip where t_{eff} is smaller than the critical value (t_{c}) for brittle-ductile transition, it is formed through plastic deformation; while for the part of the chip

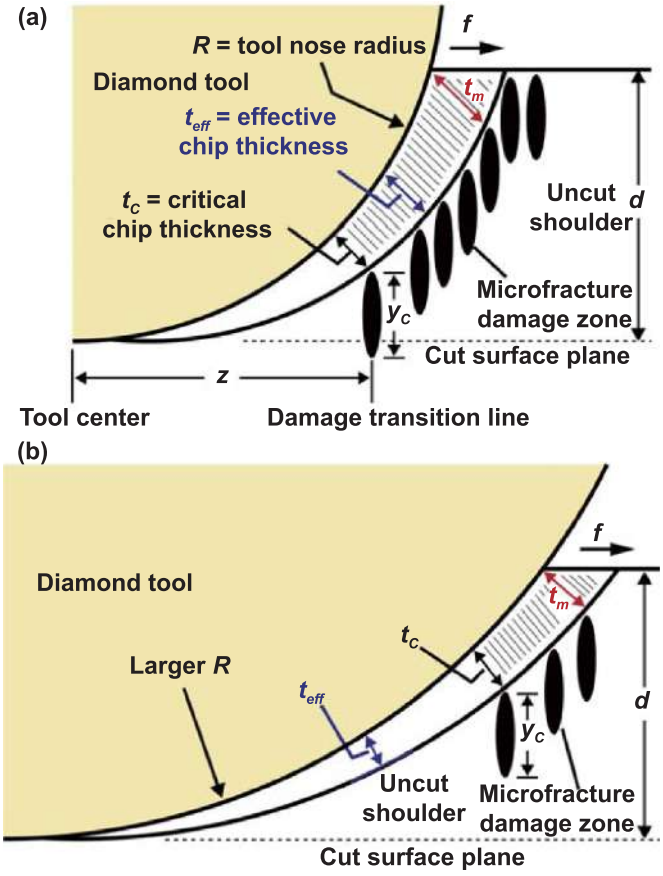

Figure 6. (a) Schematic model of ductile regime machining viewed in the plane normal to the cutting direction [61] (John Wiley & Sons). (b) Ductile regime machining model with a tool having a larger nose radius than the tool in (a).

where t_{eff} is larger than t_{c}, it is generated through brittle fracture, which subsequently causes cracks to spread into workpiece. Therefore, according to equation (1), to fabricate the entire chip in the manner of plastic deformation, the feed rate would have to be set low enough, which consequently limits the machining efficiency. However, as pointed out by Blake and Scattergood [61], the uncut shoulder would be

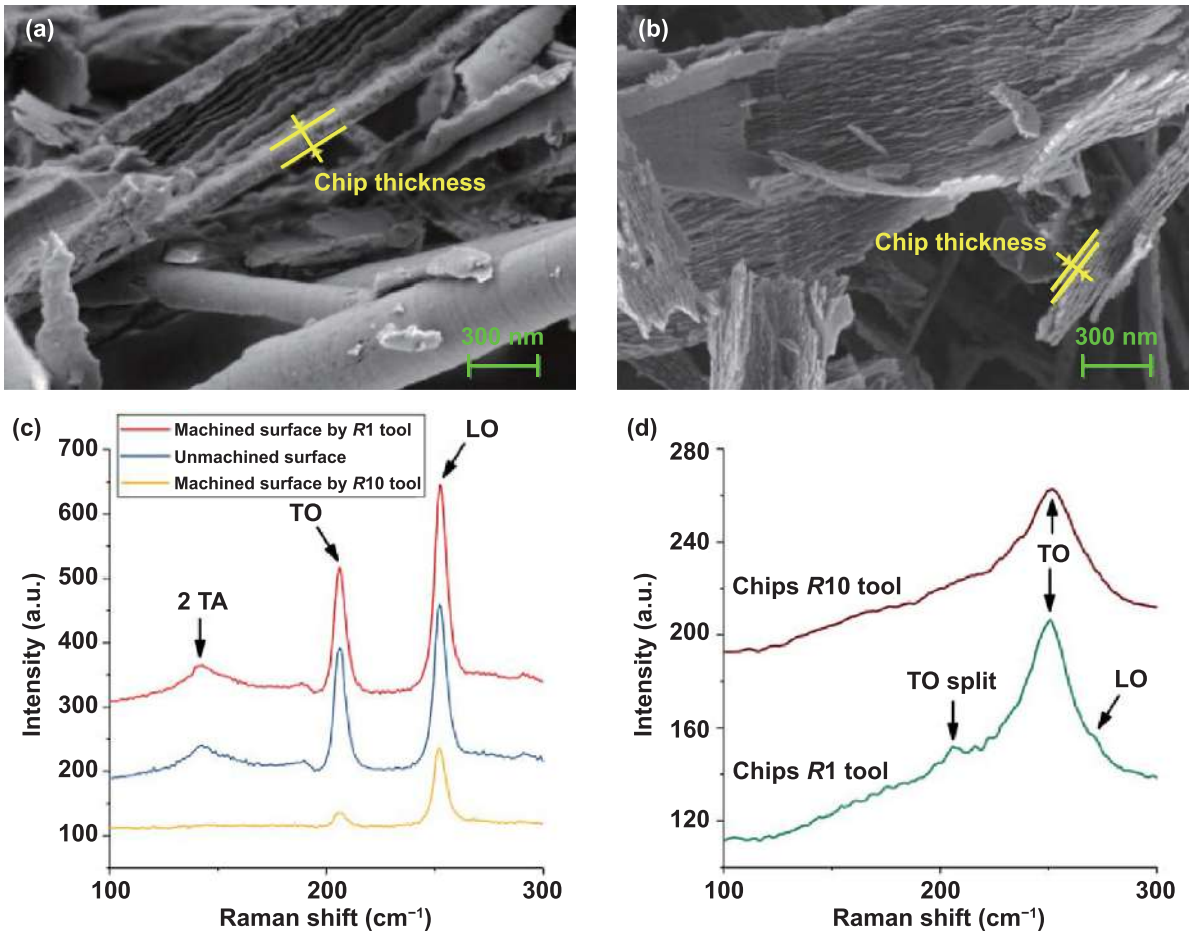

Figure 7. Cutting of ZnSe poly-crystal: high-magnification SEM images of the cutting chips generated by using (a) *R*1 tool and (b) *R*10 tool; Raman spectra of (c) unmachined surface and the machined surfaces by using *R*1 and *R*10 tools, and (d) cutting chips by using *R*1 and *R*10 tools [66] (Reproduced with permission from [66]).

removed by the following tool paths. A workpiece with a crack-free surface can be fabricated even if the cracks are generated during the cutting process, provided that the cracks do not extend into the cut surface plane, which enables ductile-regime machining, as illustrated in figure 6(a). This feature of a round-nosed tool allows the feed rate to be increased to a certain extent to achieve ductile machining of brittle materials.

To achieve small t_{eff} without reducing the feed rate, another way is to make use of a cutting tool having a large nose radius, according to equation (1). Figure 6(b) illustrates the ductile regime machining model with a tool having a larger nose radius than the tool in figure 6(a). When using the larger nose radius tool, maximum undeformed chip thickness (h_{m}, or t_{m}) would be reduced, which causes the position of critical chip thickness (h_{c}, or t_{c}) to move towards the top of the uncut shoulder and leads to a wider ductile-regime zone, given those other parameters (i.e. depth of cut and feed rate) are the same [62, 63].

As early as 1986, Fuchs *et al* [64] experimentally studied the influence of tool nose radius on the surface finish of KDP crystal. They found that the larger the nose radius, the better the surface finish, and reducing the feed rate is not as effective as increasing the nose radius in improving the surface finish. To further understand the effect of diamond tool geometry on the finished surface quality of KDP crystal, Zong *et al* [65] performed a three-dimensional finite element simulation. The simulated result is consistent with the experiment report by Fuchs *et al* [64]. Moreover, they found that the principal force increases with increasing tool nose radius, while the thrust force is independent of the tool nose radius. This is different from the diamond turning of germanium, which has higher hardness than KDP crystal. When using a small-radius tool, the principal cutting force is dominant, while using a large-radius tool, the thrust force becomes significant [63]. As a result, the tool service life (cutting distance) decreases when the nose radius increases, causing earlier formation of microfractures on the machined surface.

In the diamond cutting of ZnSe crystal, Huang and Yan [17, 66], Xiao *et al* [67] and Geng *et al* [68] observed that the larger the nose radius, the better the surface finish. High-magnification scanning electron microscope (SEM) images of cutting chips generated by using a tool with a nose radius of 1 mm (*R*1 tool) and a tool with a nose radius of 10 mm (*R*10 tool) were observed, as shown in figures 7(a) and (b) [66]. It can be seen that the chip thickness would be reduced when

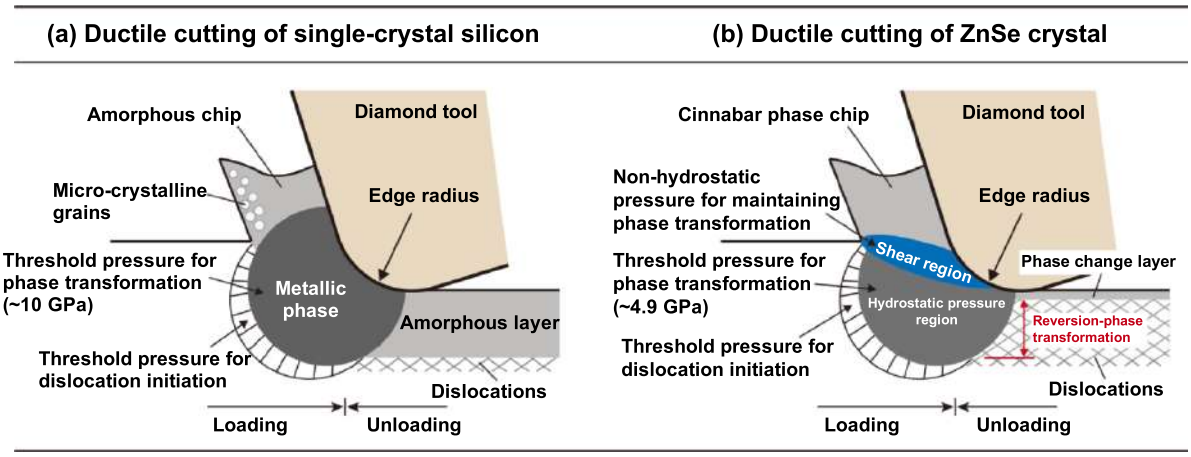

Figure 8. Schematic models of subsurface damage mechanism in the ductile cutting of (a) single-crystal silicon [32] (Reprinted from [32], Copyright (2009), with permission from Elsevier), and (b) ZnSe crystal.

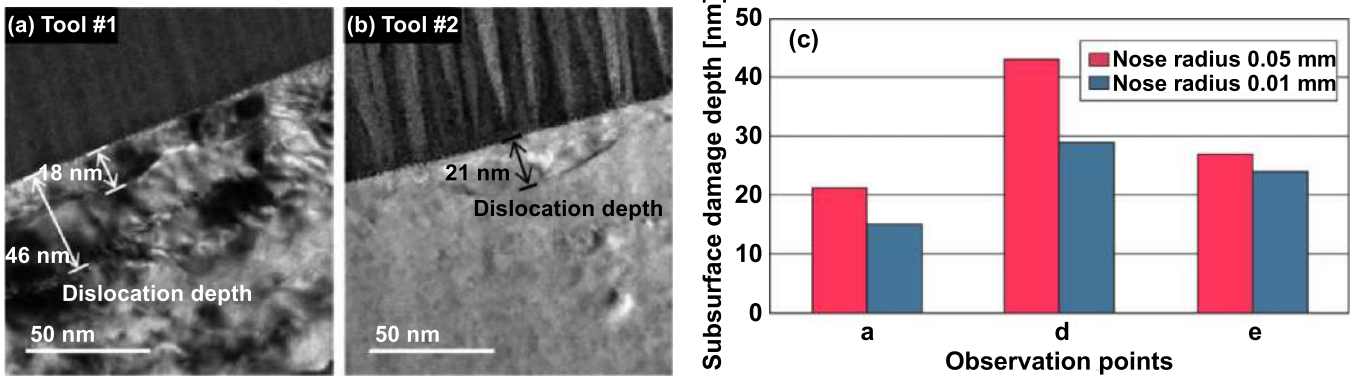

Figure 9. Cutting of CaF_2 crystal: TEM images of subsurface damage caused by (a) tool #1 with a nose radius of 0.2 mm, and (b) tool #2 with a nose radius of 0.05 mm [69] (Reprinted from [69], Copyright (2015), with permission from Elsevier); (c) Relationship between subsurface damage depth and tool nose radius at different observation points [71] (Reprinted from [71], Copyright (2017), with permission from Elsevier).

using a large nose radius tool, which is consistent with the model of maximum undeformed chip thickness. Furthermore, the Raman spectroscopy results indicate that the machining pressure increases with the tool nose radius. Because the machined surface by the *R*1 tool has a spectrum similar to the unmachined surface. In contrast, the spectrum of the machined surface by the *R*10 tool shows low intensities of transversal optical and longitudinal optical phonons and zero intensity of second-order transversal acoustic phonon, as shown in figure 7(c). In addition, the metallization of cutting chips occurs when using the *R*10 tool but rather using the *R*1 tool, as shown in figure 7(d). It is interesting to note that although the *R*1 tool likewise caused a phase transformation of cutting chips, no phase transformation was detected in the machined surface. It is considered that the phase transformation of the machined surface is reversed right after the decompression of tool-induced hydrostatic stress, which had not been reported in hard-brittle materials. The schematic models of the subsurface damage mechanism in the ductile cutting of single-crystal silicon (a typical hard-brittle material) and ZnSe crystal (a typical soft-brittle material) are compared, as shown in figure 8. In the ductile cutting of single-crystal silicon, a hydrostatic pressure-induced phase transformation will be retained in the subsurface after unloading. In contrast, in the ductile cutting of ZnSe crystal, hydrostatic pressure-induced phase transformation will be reversed mostly after unloading, leaving an extremely thin phase change layer in the subsurface that a Raman microscope cannot detect; however, a phase transformation will be retained in the cutting chips that underwent strong shear stress (non-hydrostatic pressure).

Although the finished surface quality of soft-brittle crystal can be improved by using a tool with a relatively large nose radius, the Raman results presented in figure 7(c) also indicate that a large nose radius tool would induce greater subsurface damage of the workpiece, due to the phase transformation in the workpiece. Similarly, Kakimuma *et al* [69] reported that in the diamond turning of CaF_2 crystal, a tool with a smaller nose radius produces more shallow subsurface damage. It can be observed from transmission electron microscope (TEM) images (figures 9(a) and (b)) that the amount and location of the dislocation lines are larger and deeper in the workpiece machined by the larger nose radius tool. Then they

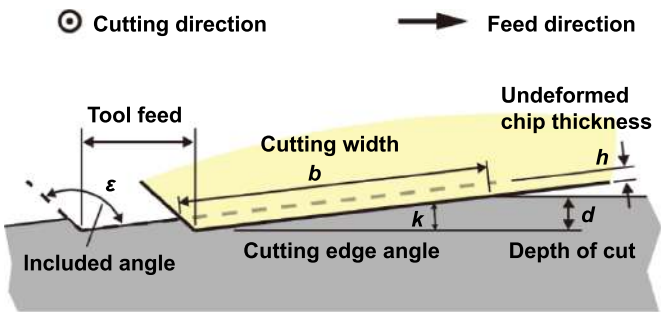

Figure 10. Machining model of a straight-nose tool.

characterized different areas on the CaF_2 workpiece and summarized the relationship between subsurface damage depth and tool nose radius, as shown in figure 9(c) [70].

Unlike cutting crystals, the cutting speed plays a dominant role in surface quality of amorphous polymers because high cutting speed might cause thermally induced softening/melting and high strain-rate induced embrittlement in polymers [72]. These two effects may coexist; as a result, there are reports of better surface finish with a large nose radius tool [73], and also reports of better surface finish with a small nose radius tool [74]. By regulating the cutting speed, feed rate, and depth of cut, several plans are possible to achieve equivalent surface quality.

2.1.2. Straight-nosed tool. The machining model of a straight-nosed tool is presented in figure 10. Compared to the model of the round-nosed tool (see figure 6), it can be seen that undeformed chip thickness (h) is constant along almost the entire main cutting edge. The h can be estimated by the following equation [75]:

$$h = f \cdot \sin\kappa \tag{2}$$

where f is the feed rate, and κ is the cutting edge angle.

According to equation (2), when using the straight-nosed tool, an extremely small h can still be achieved at a large feed rate by setting a small cutting edge angle, which ensures higher efficiency of ductile machining compared to the round-nosed tool [76]. Moreover, the uniform thickness of cutting chips over a wide cutting width b provides a plane strain condition. This plane strain condition will promote the maintenance of hydrostatic pressure in the cutting region, which is necessary for ductile material removal [76]. However, the straight-nosed tool may also cause deeper subsurface damage compared with the round-nosed tool under the same cutting depth and cutting speed, which was revealed by MD simulation [8].

Figure 11(a) shows an SEM image of a CaF_2 surface machined by a straight-nosed tool under a continuously varied feed rate from 40 to 1 μm rev^{-1} (the corresponding undeformed chip thickness ranges from 1 μm to 26 nm) [77]. Two types of microfractures were observed, of which the A-type microfractures generated under a large feed rate due to both the size effect and the crystallographic effect of ductile-brittle transition (DBT). A-type microfractures are the same as the microfractures reported in the cutting of silicon [76]. However, B-type microfractures have never been reported in cutting hard-brittle materials, which are characterized by straight fringes with smooth and flat fractured surfaces and develop to several hundreds of microns in diameter, as shown in figure 11(b). Such microfractures develop when the feed rate is very low and are less dependent on crystal orientation. The critical feed rate f_{c1} (above f_{c1} A-type microfractures generated) and the critical feed rate f_{c2} (below f_{c2} B-type microfractures generated) are summarized in figure 11(c), when using different rake angle tools. Moreover, it was found that B-type microfractures only occurred during the wet cutting with a low tool feed, while they disappeared during low tool feed dry cutting. Therefore, thermal effect is one possible reason for generating B-type microfractures because the thermal conductivity of CaF_2 is extremely low (0.06 times that of silicon), and the thermal expansion coefficient is extremely high (5.8 times that of silicon) [77]. A schematic model for mechanisms of thermal fracturing occurring during low tool feed wet cutting is illustrated in figure 11(d).

2.1.3. V-shaped tool. The machining model of a V-shaped tool (see figure 12) is similar to the model of the straight-nosed tool in which the undeformed chip thickness (h) is unvarying along the main cutting edge, except that the V-shaped tool has two symmetrical main cutting edges. Moreover, using a V-shaped tool to machine micro-structured surfaces, in particular micro V-shaped grooves, on soft-brittle materials is more challenging for the following reasons [78]: first, when using a tool with a specific included angle (ε), the undeformed chip thickness is only determined by the feed rate, and thus the feed rate must be controlled precisely to achieve ductile machining. Second, high stress concentration occurs at the apex of the groove edge. Owing to the soft and brittle qualities of the material, cracks are likely to initiate at this region, causing material spalling, as illustrated in figure 12. Third, the crystallographic effect is more significant than when using round-nose and straight-nosed tools. Because the left side (L-side) and right side (R-side) surfaces of a V-shaped groove have different relative positions with respect to the cleavage and slip planes of a crystal grain, as illustrated in figure 12.

To avoid spalling at the apex of the groove edge when microgrooving ZnSe poly-crystal, Huang and Yan [78] applied a coating of photosensitive resin over the workpiece surface and then cured the resin with ultraviolet light before the machining process. Results showed that the pre-coating layer significantly suppressed brittle fractures at the edge of the groove, as shown in figure 13. The finite element method (FEM) simulation results suggest that the resin coating can make the tensile stresses along the cutting direction and the direction normal to the workpiece surface distributed away from the edge of the groove and the workpiece surface. In the diamond turning of CaF_2 crystal, it is likewise found that the pre-coating can improve the DBT of material [79].

When microgrooving ZnSe poly-crystal, Huang and Yan [78] also observed a strong crystallographic effect on the left-side (L-side) and right-side (R-side) surfaces of the groove

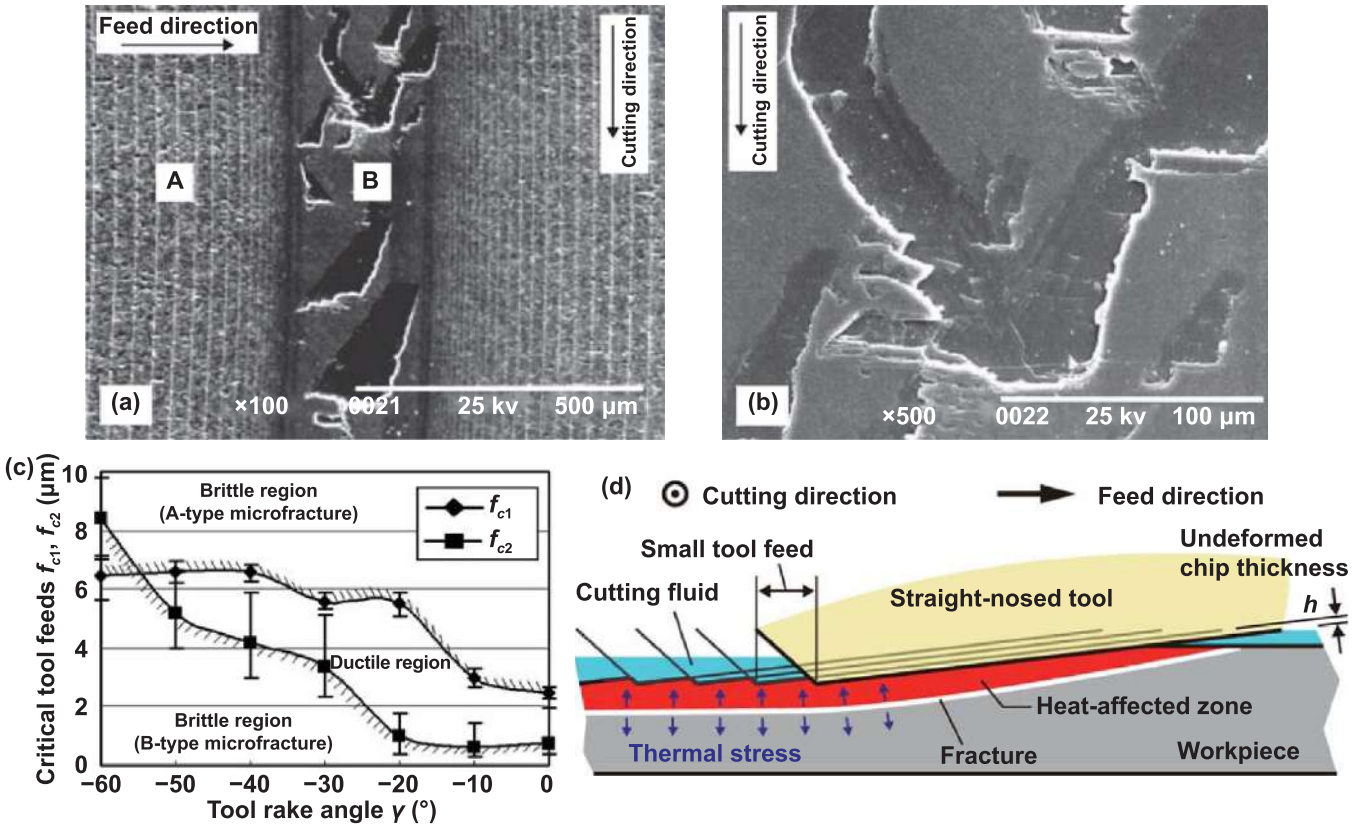

Figure 11. Cutting of CaF_2 crystal: SEM images of (a) surface machined at continuously varied feed rate and (b) close-up view of B-type microfractures [77]. (c) Variation in the critical tool feeds f_{c1} and f_{c2} with respect to the tool rake angle [77] (Reprinted by permission from Springer Nature Customer Service Centre GmbH: Springer Nature, The International Journal of Advanced Manufacturing Technology. [77], Copyright 2004). (d) Schematic model for mechanisms of thermal fracturing occurring during small tool feed wet cutting.

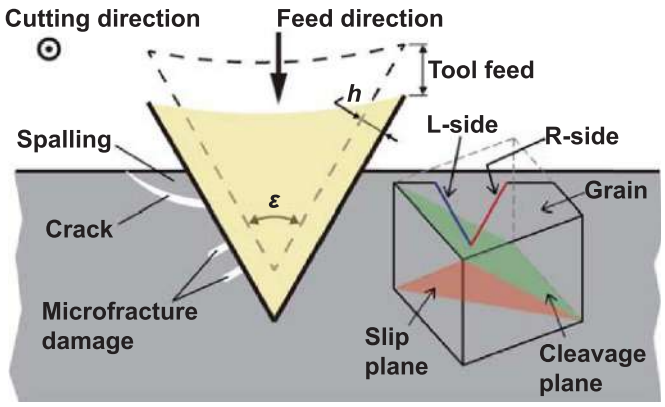

Figure 12. Machining model of a V-shaped tool.

by machining double groove, as shown in figure 14. Under the same cutting conditions, in grain A the microfractures only formed on the L-side surface, while in grain B the microfractures only formed on the R-side surface. The strong crystallographic effect in the micro-grooving of soft-brittle materials is attributed to the fact that in the cutting process the low hardness of the material leads to low machining pressure, and thus there is no amorphous layer formation in the subsurface. This is different from the cutting of hard-brittle materials, where the amorphization would occur in the subsurface due to the high hardness-induced high machining pressure. And as a result, the amorphous layer can decrease the anisotropy of the crystal. The schematic models of surface formation mechanisms in the micro-grooving of ZnSe crystal (a typical soft-brittle material) and single-crystal silicon (a typical hard-brittle material) are illustrated in figure 15.

The absence of an amorphous layer in the machined subsurface was also found when plunge grooving CaF_2 crystal, and the effect of the grooving induced stress field is reflected by a lattice misfit or rotation, evidenced by the selected area electron diffraction (SAED) pattern and high-resolution TEM (HR-TEM) image of the deformed layer, reported by Wang *et al* [80]. Moreover, they developed a crystal plasticity finite element method simulation for orthogonal cutting, where the crystal plasticity constitutive model is characterized by the material non-linearity with crystallographic slip governed by Schmid's law, to reveal the mechanism of the anisotropic brittle-ductile transition and stress-induced lattice rotation. Figures 16(a) and (b) show the simulated stress distribution from a different side of the workpiece. The left side is dominated by tensile stress around node c, which is responsible for crack initiation, while the right side presents compressive stress around node b, which is unfavorable for crack initiation, as illustrated in figure 16(c). Moreover, the different stress

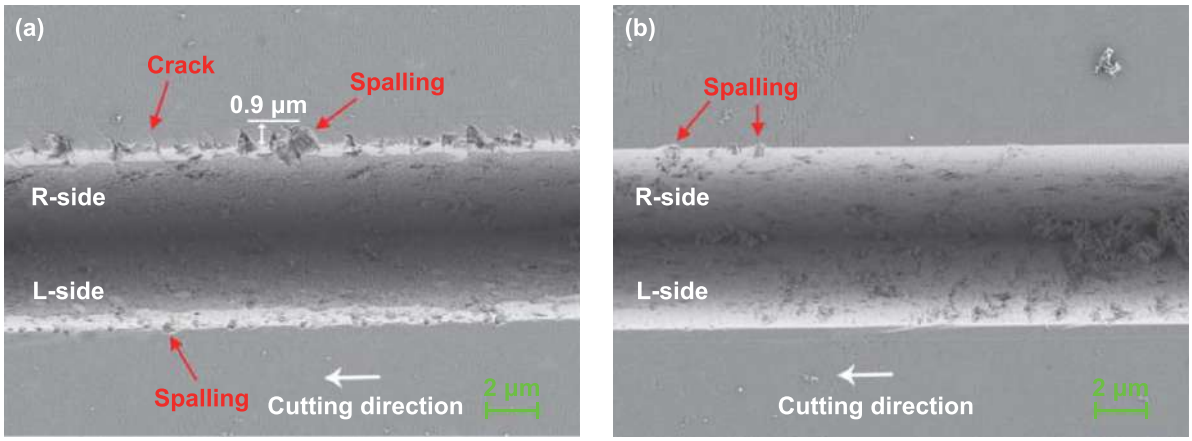

Figure 13. Cutting of ZnSe poly-crystal: SEM images of the V-shaped grooves machined on (a) the uncoated workpiece and (b) the pre-coated workpiece [78] (Reproduced from [78]. CC BY 4.0).

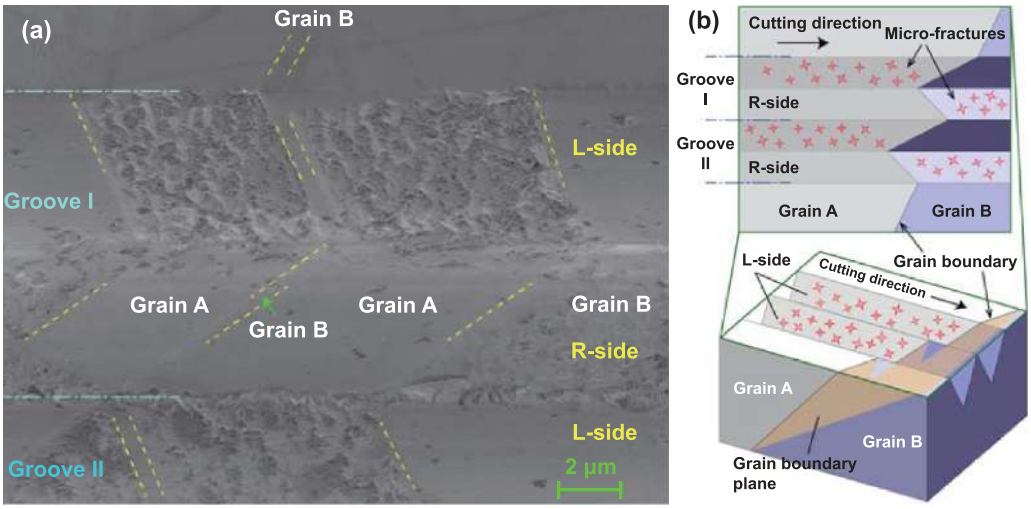

Figure 14. Cutting of ZnSe poly-crystal: (a) SEM image of a typical area in the double groove; (b) schematic of the grain boundary plane which corresponds to the grain boundary in (a) [78] (Reproduced from [78]. CC BY 4.0).

states among nodes cause the lattice rotation, as presented in figure 16(d).

2.2. Edge radius

In ultraprecision diamond turning, the undeformed chip thickness is as small as the edge radius of a single-crystal diamond tool. Therefore, the edge radius cannot be ignored like the conventional cutting process, because the effective rake angle is no longer equal to the nominal rake angle and varies with the ratio of undeformed chip thickness (h) to edge radius (r). The effective rake angle of the cutting tool can be approximated with the following equation:

$$\gamma_e = -\frac{\pi}{2} + \cos^{-1}\left(1 - \frac{h}{r}\right) \qquad (h < r) \qquad (3)$$

where h/r is known as relative tool sharpness (RTS).

With the variation of RTS value, the chip formation mechanisms exhibit four distinct behaviors, including shearing, extruding, plowing, and rubbing, which are independent of one another [81, 82]. It is commonly accepted that there is a stagnation point S (threshold) in nanometric cutting. When the RTS is below the threshold, as shown in figure 17(a), the material is not removed from the workpiece but deforms elastic-plastically and passes the lowest cutting edge point L; after the material has passed through the tool, the elastic portion D_e springs back and the plastic deformed portion Δ leads to a permanent deformation behind the point P. When the RTS is greater than the threshold, as shown in figure 17(b), the material above the threshold will be removed and its accompanying chip formation. Although these models can qualitatively describe the material removal mechanism when the undeformed chip thickness is at atomic or nanometric scale, the specific threshold for a certain material is far from understood, because the real-time observation of chip formation at such scale is very difficult. Therefore, finite elements and MD simulations are common methods to investigate the effects of edge radius [83–85].

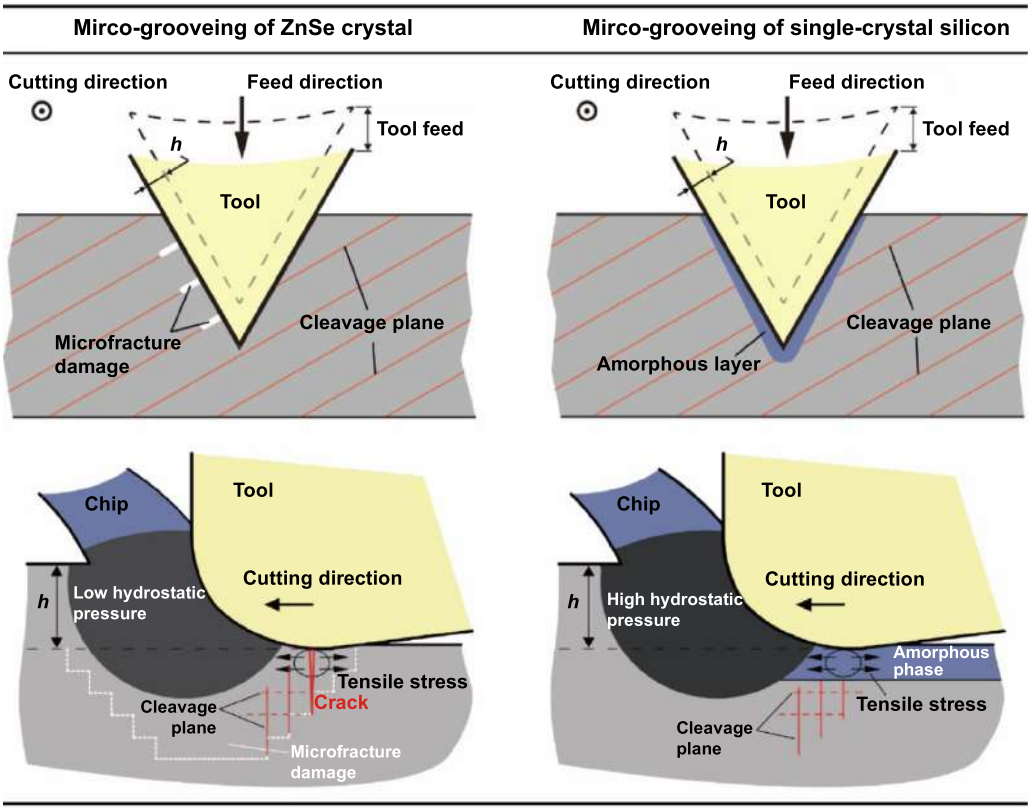

Figure 15. Schematic models of surface formation mechanisms in micro-grooving of ZnSe crystal and single-crystal silicon.

Chen *et al* [87] studied the effects of edge radius on the ductile machining of CaF_2 using a 2D finite element method. The CaF_2 was modeled as an elastic-plastic body. The chip formation was simulated by the remeshing chip separation criterion, and the friction between the tool and chip is defined as the shear type. Their simulation results showed that the cutting forces, especially the thrust force, increase significantly with the edge radius. Additionally, the area of high Von Mises stress in front and beneath the tool tip is extended, but the maximal Von Mises stress and hydrostatic stress in the cutting region is decreased, as the edge radius increases. Therefore, they suggested that a sharper edge radius tool should be used in the ultra-precision cutting of CaF_2. Zong *et al* [65] developed a 3D finite element model to study the effects of edge radius on the ductile machining of KDP crystal. The material constitutive equation was defined by the curve of true flow stress vs. plastic strain obtained from nanoindentation. The thermal effect caused by tool-workpiece friction and material plastic deformation was also considered. They found that a larger edge radius will produce more extrusion between the cutting edge and the chip root, and more friction and burnishing effect between the cutting edge and the machined surface. The maximal machining pressure would be increased with the edge radius, leading to more chip deformation and greater difficulty in chip flow. Consequently, the finished surface quality deteriorated. Although both simulation results indicate that a larger tool edge results in worse machined surface quality, it should be pointed out that these two simulation studies were performed with a constant undeformed chip thickness (h), and the tool edge radius was increased from smaller than the h to larger than the h. In other words, the RTS was reduced as the tool edge radius increased, causing the chip formation mechanisms to change from shearing to plowing. However, if the tool edge radius and undeformed chip thickness are both increased, a degree of ductile mode machining can also be achieved. This situation is usually experienced in the micro end milling process, which will be discussed in detail in section 3.2.

Zhang and Zong [88] characterized the cutting edge defects of a mechanically polished diamond tool using an atomic force microscope. They classified the tool edge defects into blunt-edge, crescent-edge, A-type flat-edge (similar to flank wear), and B-type flat-edge (similar to chamfered edge) micro defects, as shown in figure 18. Then, they modeled these defective tools and used them to machine KDP crystals through smoothed particle hydrodynamics (SPH) simulation. An elastoplastic material model defined by the stress–strain curve of KDP was developed coupled with a minimum pressure failure criterion, i.e. when the pressure of SPH particles is below −500 MPa, the stress states of the SPH particles will be deactivated (stress becomes 0). Moreover, the contact defined for SPH also becomes inactive for these

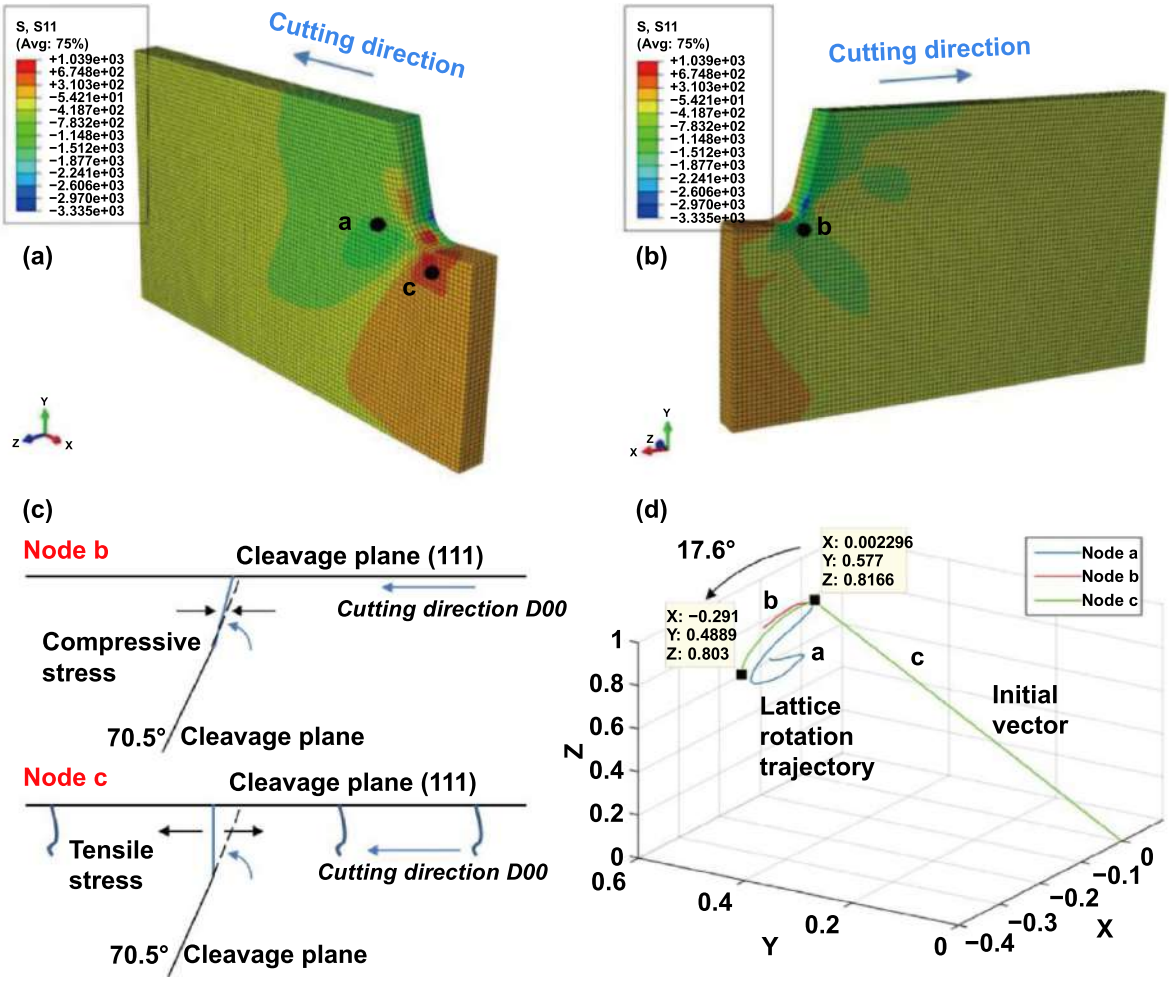

Figure 16. Crystal plasticity finite element method (CPFEM) simulation results of normal stress (in MPa) in the cutting direction D00: (a) left view, and (b) right view; (c) a model of microcrack formation based on the stress state and cleavage plane rotation at nodes (b) and (c); (d) the simulated lattice rotation of nodes (a)–(c) [80] (Reprinted from [80], Copyright (2016), with permission from Elsevier).

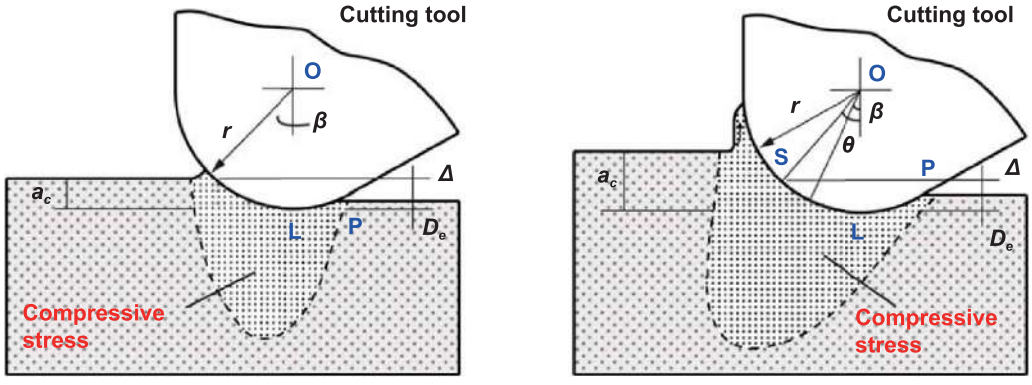

Figure 17. Schematics of cutting models at the relative tool sharpness (a) less than threshold, and (b) greater than threshold [86] (Reprinted from [86], Copyright (2005), with permission from Elsevier).

deactivated particles. Results (see figure 19) show that the machined surfaces by crescent-edge and A-type flat-edge tools are not smooth with large craters due to the disappearance of hydrostatic pressure beneath the tool tip. In contrast, the machined surfaces by blunt-edge and B-type flat-edge tools are smooth with a favorable increment of hydrostatic pressure. This indicates that the negative effects of tool edge micro defects on machining soft-brittle materials could be eliminated by making the tool edge blunt. Nevertheless, when using a relatively large edge radius tool to machine

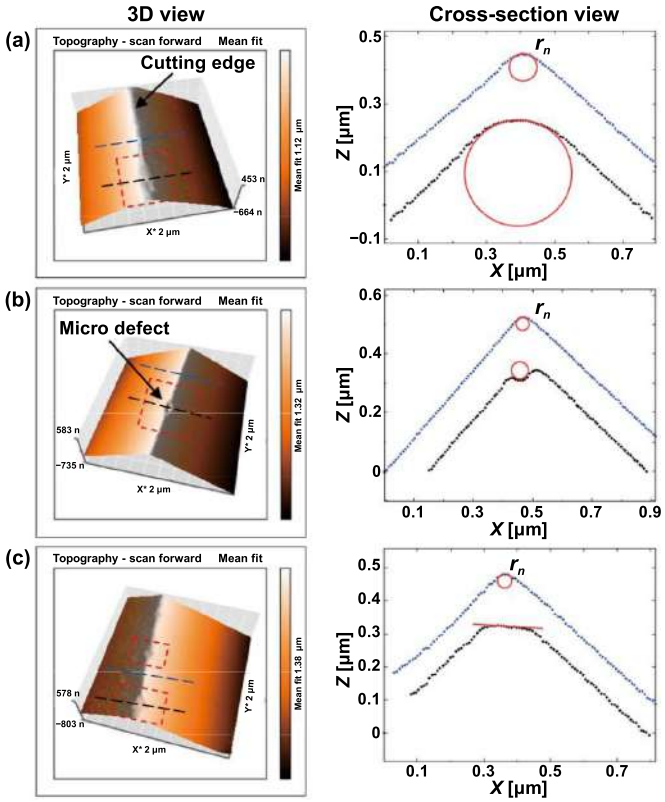

Figure 18. Three-dimensional and cross-section views of edge defects: (a) blunt-edge micro defect, (b) crescent-edge micro defect, and (c) flat-edge micro defect [88] (Reproduced from [88]. CC BY 4.0).

soft-brittle materials, the lower limit of undeformed chip thickness must be taken into account to avoid the plowing effect, which causes micro craters and pits on the machined surface [89]. The negative impact of the small RTS-induced plowing behavior is more significant when cutting soft-brittle crystals than when cutting hard-brittle crystals. This may be attributed to the fact that plowing promotes the phase transformation in hard-brittle crystals, which reduces material brittleness, while the phase transformation does not occur in the cutting of soft-brittle crystals. By contrast, for the cutting of amorphous polymers, the formation of burrs increases with tool edge radius due to the enhanced plowing effect [72].

2.3. Rake/relief angles

As stated in section 2.2, the hydrostatic stress in the cutting region is necessary for ductile machining brittle materials. In addition to the edge radius, the rake angle of the tool has an important influence on the distribution of the hydrostatic stress, which could directly impact the value of critical undeformed chip thickness [90].

In the diamond cutting of CaF_2 crystal, Yan *et al* [77] systematically studied the effects of rake angle on critical tool feed rate by carrying out a series of turning experiments using diamond tools with different rake angles (varied from 0° to −60°) and a constant relief angle (6°). In their study, A-type and B-type microfractures (see figure 11) were observed if the feed rate was above f_{c1} and below f_{c2}, respectively, as introduced in section 2.1.2. Figure 11(c) shows the variation in the critical tool feed rates f_{c1} and f_{c2} with respect to the tool rake angle. It can be seen that the ductile region ($f_{c2} < f < f_{c1}$) is widest when the tool rake angle is −20° and becomes narrow if the rake angle changes to a more negative value. Figure 20 presents the continuous ribbonlike chips produced at a rake angle of −20°, similar to the chips produced by metal cutting. These chips indicate that the material was removed in a completely ductile mode. Through the FEM simulation, Chen *et al* [87] likewise found the optimal rake angle is −20° in the cutting of CaF_2, according to the analysis of the Von Mises stress and tensile stress in the cutting region. At the rake angle of −20°, both the Von Mises stress and tensile stress are minimal. Chen *et al* [91] performed plunge-cut experiments using cutting tools with different rake angles (varied from 0° to −35°) and found the −15° rake angle tool can achieve the largest critical depth of cut for DBT in CaF_2 crystal.

Compared to a zero-rake angle tool, a negative rake angle tool can generate a high hydrostatic pressure in the cutting region, especially after the onset of tool flank wear. It is this high hydrostatic pressure that enables a nominally brittle material to be plastically deformed under a shear stress and removed in a ductile mode, rather than fractured in a brittle manner. Under the high hydrostatic stress state, the resolved tensile stress on the cleavage planes of the crystal will be significantly counteracted and become insufficient to cause cleavage fractures [75]. However, it is worth mentioning that the negative rake angle may have a side effect on the machined surface integrity of a soft brittle material. Because the subsurface damage caused by a negative rake angle tool is more severe than that by a 0° rake angle tool, as reported in the turning of CaF_2 crystal [69]. Therefore, a highly negative rake angle tool, which is usually used for cutting hard-brittle materials, is not suitable for cutting soft-brittle materials because a thick subsurface damage layer will be generated in soft-brittle materials under a highly negative rake angle tool.

In the diamond cutting of KDP crystal, the tool rake angle has a great impact on the distribution of hydrostatic pressure in the cutting chips. According to the simulation results, when the rake angle is −45° and −35°, the hydrostatic compressive stress almost distributes in the entire chip, which is favorable to the formation of continuous chips; while the hydrostatic tensile stress appears in the chip as the rake angle increases from −25° to 0°, resulting in discontinuous chips [92]. Based on the simulation method as well, Zong *et al* [65] found that both the principal and thrust forces are increased as the rake angle varies from 0° to −45°. However, the contact pressure first decreases and then increases; the minimum contact pressure is reached at a rake angle of −25°. According to the fact that the variation trend of surface roughness in the experiment agrees with the simulated contact pressure trend, they believe that a negative rake angle tool has more extruding effect on cutting chip, which in return increases chip accumulation; but only at the rake angle of −25°, the extruding effect of the tool is fully consumed by the plastic deformation,

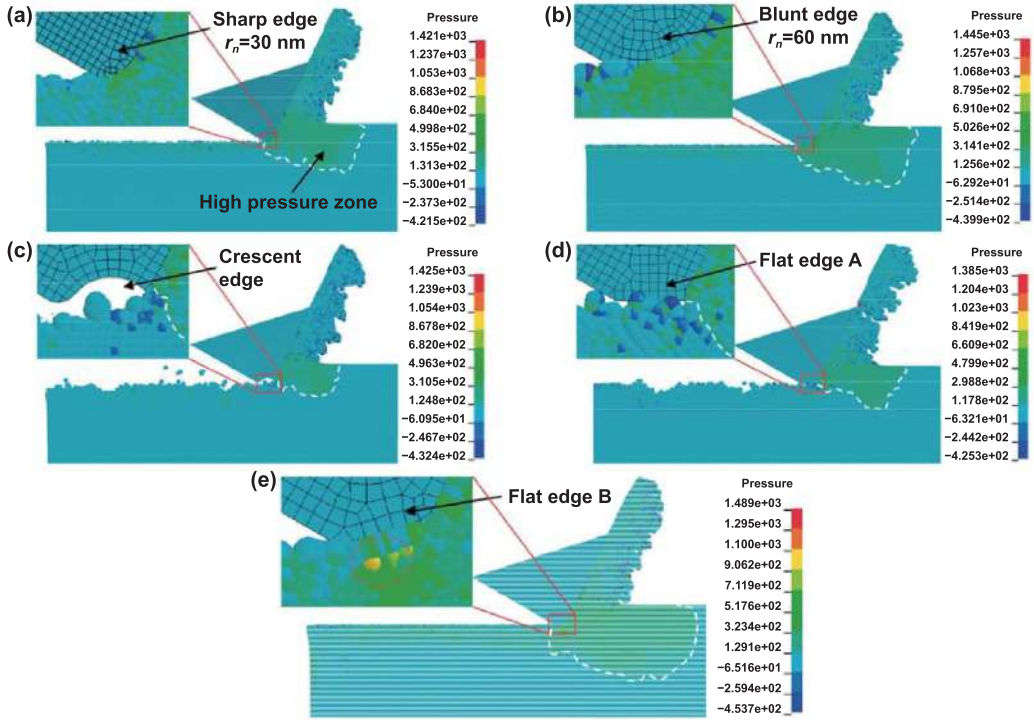

Figure 19. Cutting simulations of KDP crystal showing the distribution of hydrostatic pressure in the cutting region when using tools with different cutting edge geometries: (a) sharp edge with $r_n = 30$ nm, i.e. the ideal condition, (b) blunt edge with $r_n = 60$ nm, (c) crescent edge, (d) A-type flat edge, and (e) B-type flat edge [88] (Reproduced from [88]. CC BY 4.0).

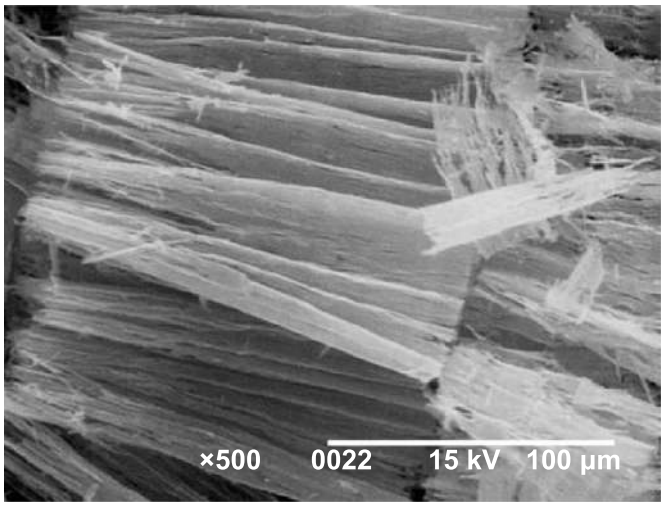

Figure 20. SEM image of continuous CaF_2 chips produced under the rake angle of -20°, indicating ductile-regime material removal [77] (Reprinted by permission from Springer Nature Customer Service Centre GmbH: Springer Nature, The International Journal of Advanced Manufacturing Technology. [77], Copyright (2004)).

consequently facilitating the flow of cutting chip on the tool rake face. Chen [93] *et al* simulated the maximal tensile stress in the cutting region at different rake angle tools. They found that when the rake angle decreased to about -45° the tensile stress reached the minimum, and if the rake angle continued to decrease, the tensile stress became greater. The experimental result that the best surface quality of the KDP crystal was obtained at the rake angle of -45° verified the simulation results. The different conclusions on the optimal tool rake angle between Zong *et al* [65] and Chen *et al* [93] may be attributed to the different edge radii of tools: the former is 70–80 nm, while the latter is 150 nm.

In the diamond cutting of amorphous polymers, Yan [72] used zero-rake angle and positive rake angle tools to cut photoresist. Results show that the zero-rake angle tool can produce a crack-free surface, and the surface fractures increase dramatically with the tool rake angle. They attribute this phenomenon to the fact that a high rake angle enhances tensile stress in the cutting region, causing the material to fracture. Zhou *et al* [94] fabricated micro lens arrays on PMMA with a high-quality surface, and the tool used in the machining had a zero-degree rake angle. The undeformed chip thickness must be less than ∼890 nm to ensure the ductile mode cutting at low cutting speed.

Table 2 summarizes the optimal rake angle of cutting tools for machining different soft-brittle materials. In general, the negative rake angle cutting tools are favorable for ductile machining soft-brittle materials. As expected, in the diamond cutting of ZnSe crystal, a negative rake angle tool is beneficial to ductile machining by improving the value of critical undeformed chip thickness [67, 68]. However, Fang *et al* [95], and Huang and Yan [17] reported that the best surface finish is obtained with a 0° rake angle tool, and microfractures occur on the machined surface when using a negative rake tool. This might be caused by the experimental setup in which the relief angle was increased significantly when the rake angle was set to negative.

Table 2. The recommended rake angle of cutting tools in the ultraprecision diamond turning of soft-brittle materials.

Material	Recommended rake angle γ	Nose radius (mm)	Edge radius (nm)	Method
CaF_2	-20° (relief angle of 6°) [77]	Straight nose	20–40	Experiment
CaF_2	-15° [91]	5	N/A	Experiment
CaF_2	-20° (relief angle of 10°) [87]	N/A	100	2D Simulation
KDP	-45° (relief angle of 8°) [93]	N/A	Ideally sharp	Expt. and 2D Simul.
KDP	-25° (relief angle of 8°) [65]	1	Ideally sharp	Expt. and 3D Simul.
KDP	$-45^\circ < \gamma < -25^\circ$ (relief angle of 8°) [92]	1	~40	Expt. and 3D Simul.
ZnS	$<-25.5^\circ$ (relief angle of 9°) [23]	0.75	25.4	Expt. and 3D Simul.
ZnSe	-25° (relief angle of 12°) [67]	0.2	~20	Experiment
ZnSe	-25° (relief angle of 10°) [68]	1.15	N/A	Experiment
ZnSe	0° [95]	N/A	N/A	Experiment
ZnSe	0° (relief angle of 8°) [17]	1	~50	Experiment
Photoresist	0° (relief angle of 10°) [72]	10	50	Experiment
PMMA	0° (relief angle of 10°) [94]	0.1	N/A	Experiment

Therefore, it can be inferred that the relief angle of the tool likewise affects the ductile machining of soft-brittle materials. In the diamond cutting of KDP crystal, Zong *et al* [65] indicated that both the principal and thrust forces decrease with the increase of relief angle, especially for the thrust force, due to a decreasing contact area between the machined surface and the tool flank face. But the maximum contact pressure shows a trend of decreasing first and then increasing, which comes to be the lowest at the relief angle of 8°. According to the statistics for machined surface roughness, it is believed that both the smallest friction and burnishing effects at a relief angle of 8° contribute to the best surface quality.

3. Micro end milling

Micro end milling is an important manufacturing technique for fabricating three-dimensional surfaces on components [96, 97]. Different from the turning process, during which the tool continues to cut the material and maintain a stable state of cutting force, in the milling process the tool intermittently cuts the material due to the rotation of the tool with multiple cutting edges. As a result, the cut-in and cut-out of materials are repeatedly performed in the milling process, which is more complicated than the turning process. Due to the fact that a micro end milling cutter has an effective diameter of tens to hundreds of microns and an edge radius of about 0.1–10 μm, it can produce a microscale material removal, fabricating components of micrometric dimensions [98]. However, considering that the diameter of end milling cutter is reduced on a scale similar to the diameter of human hair, the cutting forces must be controlled to stay below a very small value, because the miniature end milling cutter is easily broken even if the cutting force is a few tens of millinewtons [99].

Like the diamond turning process, to achieve ductile milling of brittle materials, the undeformed chip thickness should be less than a critical value. Figure 21(a) illustrates a machining model of micro end milling. It can be seen that the undeformed chip thickness (h) gradually increased from zero at the beginning of the cut to a maximal value at the center of the cut, and then decreased to zero again at the end of the cut. The undeformed chip thickness can be approximately estimated by the following equation [100]:

$$h = f_t \sin\theta \quad \text{if} \quad f_t/R << 1 \tag{4}$$

where f_t is feed per tooth, θ is the position angle at the cutting point, and R is tool radius.

Therefore, the cutting zone of micro end milling can be divided into plowing zone, ductile zone, and brittle zone, according to the value of h [101]. However, the cutting area of micro end milling is more complicated than that of turning because different shapes of milling cutters have distinctly different tip radii (r_t), consequently affecting the ratio to the axial depth of cut (a_p). Therefore, a three-dimensional analysis needs to be adopted by considering axial depth of cut and tip radius, which influence the size and direction of the fractures [102]. Figure 21(b) illustrates a 3D machining model of the micro end milling process. Due to the existence of the tool tip radius, the actual cutting area is uneven in the axial direction. When the axial depth of the cut is less than the tool tip radius, as shown in figure 21(c), the actual undeformed chip thickness is smaller than the undeformed chip thickness, and is related to the undeformed chip thickness, tool tip radius, and depth of cut; while when the axial depth of cut is larger than the tool tip radius, as shown in figure 21(d), the actual undeformed chip thickness is relatively uniform in the axial direction and approximately equal to undeformed chip thickness. Both the tool tip radius and axial depth of cut have important effects on the ductile micro milling of brittle material in the micro-scale because the cross-section of the chip greatly affects the cutting force, which in turn determines the chip removal mechanisms of end milling [103, 104]. Moreover, as shown in figure 21(a), since the upper side of the cut experiences a downmilling, while the lower side of the cut experiences upmilling, the two sides of the slot may have different surface quality. In general, the area experiencing upmilling (the entry zone) shows a more ductile behavior than the area experiencing downmilling (the exit zone) [105]. This is because the effective rake angle becomes more negative during upmilling, as shown in

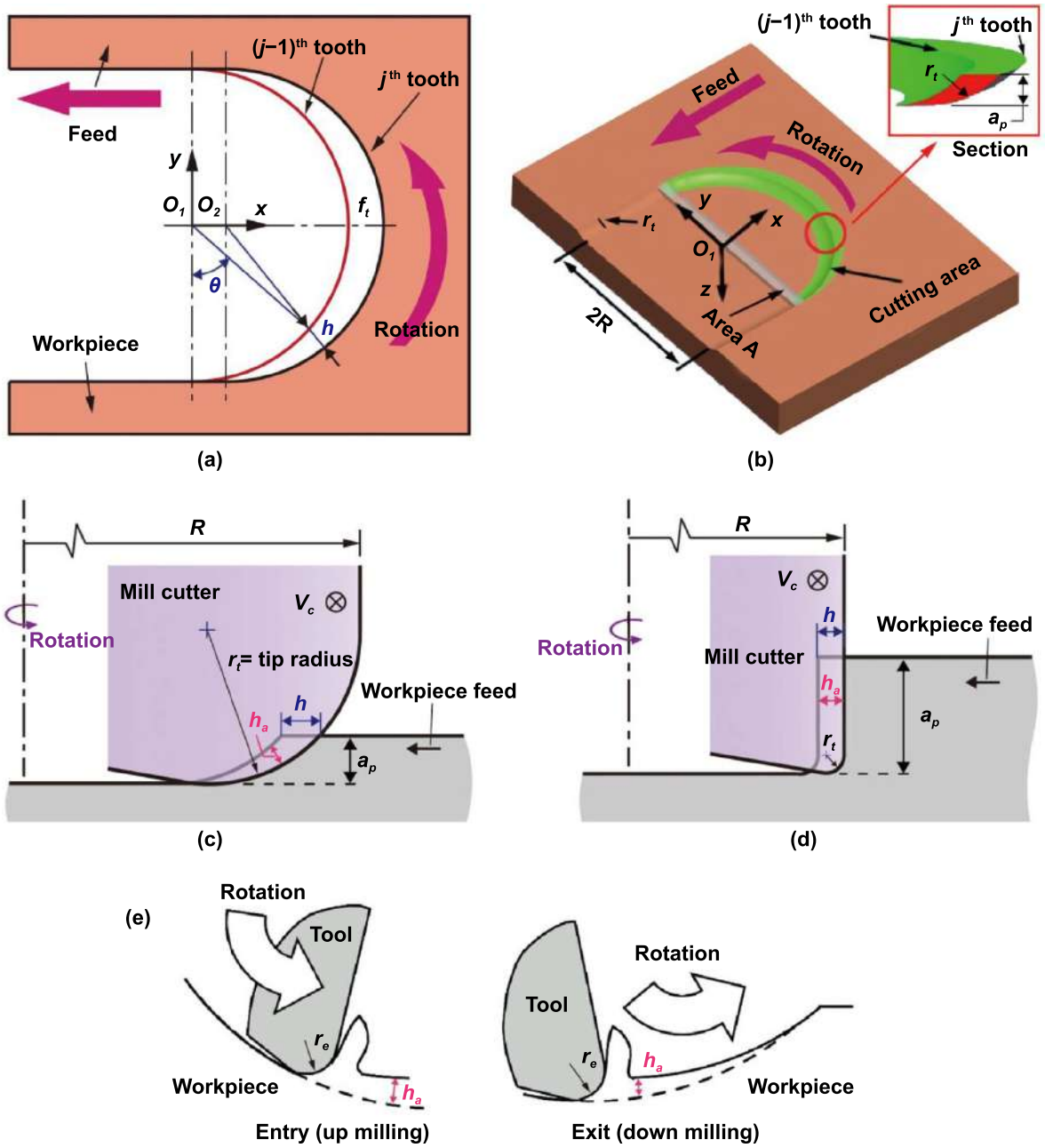

Figure 21. Schematics of micro end milling process: (a) 2D model, and (b) 3D model [100] (Reprinted from [100], Copyright (2017), with permission from Elsevier). The sectional view along the plane normal to v_c, when the axial depth of the cut is (c) smaller, and (d) larger than tool tip radius. (e) The sectional view from the plane parallel to h_a and v_c when upmilling and downmilling [106] (Reprinted from [106], Copyright (2009), with permission from Elsevier).

figure 21(e), and thus stronger compressive stress is generated, facilitating the ductile mode material removal process.

3.1. Tool shape

Researchers and companies have developed and optimized many types of cutter geometries for micro end milling [98, 99, 107]. Figure 22 presents several types of tool geometry, including (a) two-flute flat end cutter, (b) cylindrical end cutter, (c) D-shaped end cutter, (d) two-flute ball-end cutter, and (e) single-flute spherical end cutter. Among them, the former three cutters (see figures 22(a)–(c)) have a flat cutting tool edge on both end and side surfaces, and thus belong to flat end cutters. Such flat-end cutters can generate flat surfaces and slots with sharp perpendicular edges in vertical micro milling. Nonetheless, fabricating intact edges of slots on brittle materials is still challenging. Several attempts have been performed on silicon, but edge chipping is difficult to avoid [108, 109]. Xiao *et al* [104] and Chen *et al* [100] used a flat-end cutter to machine slots on KDP crystal. Although ductile mode machining was achieved on the bottom surface, the integrity of slot edges requires further improvement, as shown in figure 23(a).

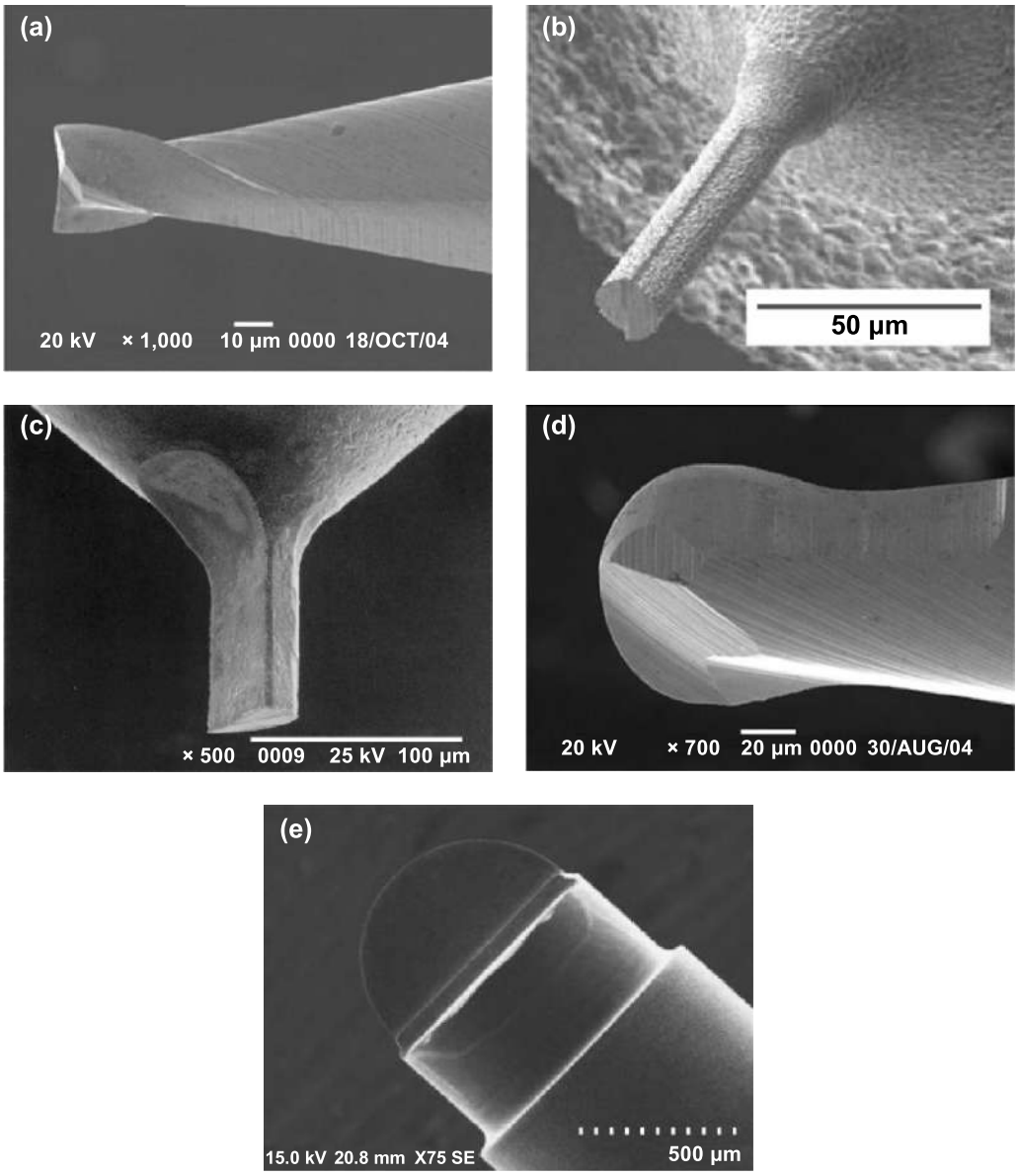

Figure 22. Micro end milling cutters: (a) two-flute flat end cutter with a diameter of 30 μm [97] (Reprinted by permission from Springer Nature Customer Service Centre GmbH: Springer Nature, Micro and Nano Fabrication Technology [97], Copyright (2018)), (b) cylindrical end cutter with a diameter of 20 μm [114] (Reprinted by permission from Springer Nature Customer Service Centre GmbH: Springer Nature, The International Journal of Advanced Manufacturing Technology [114], Copyright (2006)), (c) D-shaped end cutter with a diameter of 50 μm [115] (Reproduced from [115]. © IOP Publishing Ltd. All rights reserved), (d) two-flute ball-end cutter with a diameter of 100 μm [97] (Reprinted by permission from Springer Nature Customer Service Centre GmbH: Springer Nature, Micro and Nano Fabrication Technology [97], Copyright (2018)), and (e) single-flute spherical end cutter with a diameter of 400 μm [116] (Reprinted from [116], Copyright (2013), with permission from Elsevier).

In contrast, the latter two cutters (see figures 22(d) and (e)) have hemispherical cutting edges at the tool end, and hence belong to ball-end cutters. Such ball-end cutters are suitable for machining parts with smooth contoured micro features. Benefiting from this characteristic, micro-milling with a ball-end cutter has been accepted as the most promising method to repair the micro-defects on the surface of large soft-brittle crystals [110, 111]. Because in the ultra-precision machining and laser pre-irradiation processes of large soft-brittle crystals, micro-defects, such as cracks, pits, and ablation, are easily generated on the crystal surfaces, which dramatically reduce both the performance and lifespan of the parts. Considering that growing large crystals is time-consuming and costly, the best solution to remove defects is to repair the crystal by replacing those defects with predesigned smooth contours [112]. Figure 23(b) shows a groove milled by a ball-end cutter in a single path on KDP crystal. The edges of this groove are more intact than the edges of the groove milled by a flat-end cutter. By optimizing the interval of the spiral-milling path, the residual tool marks height along the repaired contour can be reduced, leading to a minimal light intensification inside the micro-milled surface and a better repaired surface [113].

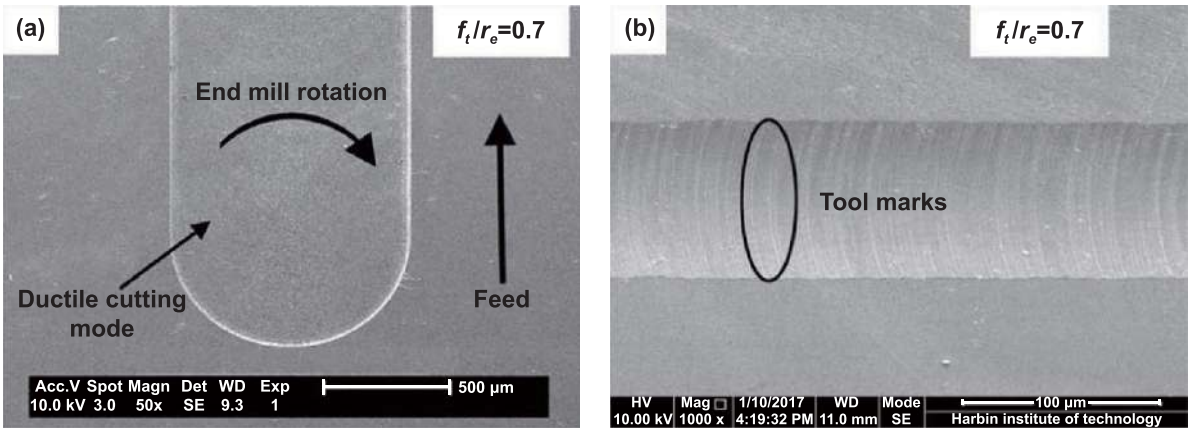

Figure 23. SEM image of the surface machined in ductile mode by using (a) a flat-end cutter [100] (Reprinted from [100], Copyright (2017), with permission from Elsevier), and (b) a ball-end cutter in the slot milling of KDP crystal [117] (Reprinted from [117], Copyright (2017), with permission from Elsevier).

3.2. Edge radius

In the micro end milling of soft-brittle materials, the undeformed chip thickness (h) is usually reduced to smaller than the edge radius to limit the cutting forces that might cause tool failure and the maximum undeformed chip thickness that may cause the brittle fracture of materials. However, as the undeformed chip thickness reduces, material deformation takes place with a highly negative tool rake angle [118], which is the same as the situation in diamond turning discussed in equation (3). Therefore, in micro end milling, if the h is less than a lower critical value $h_{\min}$ (also known as the minimum undeformed chip thickness), the plowing effect will occur; that is, the material will deform but without producing cutting chips, and consequently cause deterioration of machined surface quality and increase of specific cutting force [117]. For example, when using a tool with an edge radius of $\sim$1 μm to cut KDP crystal, the surface machined at undeformed chip thickness (h) = 100 nm was featured with many micro craters and micro pits; while the surface machined under $h = 750$ nm was nearly smooth with a few micro pits [89]. The minimum undeformed chip thickness of material removal for a certain material is closely related to the tool edge radius. By using two cutters with different edge radii to mill KDP crystal, Chen *et al* [100] found that the normalized minimum undeformed chip thickness increases with the edge radius, and the ratio of the minimum undeformed chip thickness to the cutting edge radius (λ_e) is estimated to be $0.43 \leqslant \lambda_e \leqslant 0.48$. They attributed this phenomenon to the enhanced plowing effect at a larger edge radius cutter. The enhanced plowing effect will cause a higher temperature at the cutting region because of a higher force-induced energy dissipation [119]. Consequently, the increased cutting temperature makes the material more ductile, leading to a larger normalized minimum undeformed chip thickness. The machining characteristics of polymers are more sensitive to temperature due to their low melting temperature and glass transition temperature. In the micro milling of PMMA, when the temperature is in the range of 60 °C–70 °C, the material is in the glass state, and it can be removed in the brittle mode. When the temperature increases to 70 °C–120 °C, the material is in the viscoelastic state, and thermoplastic deformation dominates the material removal behavior [120]. Ali *et al* [121] developed an empirical model for predicting the minimum chip thickness of PMMA, indicating that low cutting speed, low feed rate, and depth of cut ranging from 0.5 μm to 0.6 μm could be beneficial to reduce the minimum chip thickness. Considering that the minimum chip thickness is related to the tool edge radius and material properties, Son *et al* [122] proposed an analytical expression of the $h_{\min}$, which is determined by the tool edge radius (r) and the friction angle (β) between the tool and material as follows:

$$h_{\min} = r\left(1 - \cos\left(\frac{\pi}{4} - \frac{\beta}{2}\right)\right). \tag{5}$$

Since the edge radius greatly affects the plowing force and machined surface quality, Chen *et al* [123] developed a new theoretical model, considering the edge radius, for predicting the plowing force in the micro end milling of soft-brittle materials. Results show that the plowing force decreases quickly with the decrease of the edge radius. When the edge radius is smaller than 2.8 μm or the edge radius is larger than 4.2 μm with a feed speed larger than 5 μm z^{-1}, the plowing force can be controlled to less than the shearing force, which is believed to be beneficial to obtain a good surface finish. However, a large edge radius cutter at a large feed speed will cause a large undeformed chip thickness which is likely to exceed the critical undeformed chip thickness of brittle fracture. Therefore, a cutter having a sharp cutting edge is recommended to suppress the plowing effect and promote material shear deformation for achieving smooth machined surfaces in the micro end milling of soft-brittle materials. From this point of view, a single-crystal diamond end cutter is expected to mill soft-brittle materials because single-crystal diamonds can be sharpened to a nanometer-class sharp cutting edge. Yan *et al*

[96] realized a ductile mode milling of hard-brittle material (reaction bonded silicon carbide) by using a single-crystal diamond end cutter, though significant cutter wear was generated rapidly, which leads to deep streaks on the machined surface. In the milling of soft-brittle materials, the cutter wear should not be as severe and fast as when milling hard-brittle materials. Korkmaz *et al* [124] used a single-crystal diamond micro-endmill to machine channels on PMMA. In contrast to the excessive burr formation by using tungsten carbide tools, there is no significant burr formation on the created channels using the diamond cutter, even at high cutting speeds and feed rates. Nevertheless, up to date, the study on the milling of soft-brittle materials by single-crystal diamond end cutters is still limited.

3.3. Rake/relief angles

The milling cutters are similar to the diamond tools of the turning process, which have designed rake and relief angles for better machining performance. Based on the experience of diamond turning of soft-brittle materials, the rake angle of the mill cutters is usually negative. Chen *et al* [119] developed two types of 3D finite element models of ball-end cutters for milling KDP crystal: Type I is the cutters having rake angles from 0° to −70° with an interval of 5° and a constant relief angle of 9°; Type II is the cutters changing relief angles from 20° to 50° and having rake face and relief face which are symmetrical with reference to the axis of the cutter. By considering the distribution of stress and strain in the cutter, peak-to-valley cutting forces, and the maximum tensile stress in the workpiece, the optimal rake angle for Type I cutter and Type II cutter are found to be −25° and −45°. Then they set the Type I cutter with a constant rake angle of −25° and changed the relief angle from 0° to 18° (interval is 3°) to find a recommended relief angle. The result indicated that the relief angle of 9° is optimal, at which the friction effect is almost eliminated, and the maximum tensile stress in the workpiece reaches a minimum. It should be pointed out that in these simulations, the tool edge radius was set at zero to avoid additional influence induced by the tool edge radius. However, in the real end milling process, the undeformed chip thickness is usually less than the tool edge radius, because the undeformed chip thickness must be limited to the submicron level, but the edge radius of the mill cutter, which is made of sintered materials, is of several microns. Thus, in the micro end milling, the soft-brittle material is always machined by a cutter with a highly negative effective rake angle, which can be calculated by equation (3), independent of the nominal rake angle. Therefore, the simulation results reported by Chen *et al* [119] may provide a reference to optimize cutting parameters making the effective rake angle approach the simulated ideal rake angle. Nevertheless, a nominal negative rake angle is necessary to ensure that the effective rake angle remains negative when the tool wear occurs at the flank face. Besides, a negative nominal rake angle enhances the stiffness of the cutter, which in turn helps to obtain the machined surface quality. In general, a large negative rake angle provides a high stiffness of tools, but it does not mean the higher the negative rake angle, the higher the tool stiffness. The optimal rake angle for the highest stiffness varies with the shape of the cutter [125, 126]. In addition, the large negative rake angle and edge radius would increase the difficulty of chip formation, resulting in increased burr sizes. Positive helix angles would guide chips flowing upwards along the rake face, forming large flip burrs, while negative helix angles would suppress the flip burrs [98]. Therefore, Uchiyama *et al* [127] used a zero-rake angle cutter to mill polycarbonate and found that a large relief angle (15°) can enhance the surface finish by suppressing the cutting heat-induced welding, adhesion and unequal spaces of cutter marks.

3.4. Tool inclination angle

In the ball end milling, the cutting speed of the tool edge center is near zero. Therefore, when the cutter axis is normal to the cutting plane, the surface produced by the central cutting edge can be rough owing to the near-zero cutting speed. In this case, adjusting the milling inclination angle between the cutter and the workpiece can improve the machining performance. Figure 24 schematically illustrates the inclination angle of a ball-end cutter to the workpiece. β_{f} and β_n are the milling inclination angles along the feed direction and the direction perpendicular to the feed direction. If β_{f} and β_n are positive, the milling process is a reverse cut; if they are negative, the milling process is a plunge cut [128]. Liu *et al* [129] found that in the micro ball-end milling of KDP crystal, the reverse cut is always preferred to the plunge cut, regardless of whether the cutter is inclined along the feed direction or the direction perpendicular to the feed direction, because the reverse cut is more prone to realize the ductile mode machining. Then they developed a theoretical model, considering inclination angle and direction, for calculating the undeformed chip thickness and cutting speed in the micro ball-end milling process [130]. Results show that inclining the ball-end cutter along the feed direction with a positive angle (reverse cut) produces a smaller undeformed chip thickness than when the cutter is inclined in the opposite direction (plunge cut). Increasing the milling inclination angle will increase the effective cutting speed and decrease the velocity gradient along the engaged cutting edge, which jointly result in a smaller equivalent shear angle and consequently reduce the surface roughness. When micro ball-end milling KDP crystal, a positive inclination angle of 45° was found to obtain a better machined surface roughness.

Foy *et al* [106] investigated the effect of inclination angle on brittle-ductile transition in the micro milling of glass by tilting the cutter 0° to positive 60°. The material removal mode in relation to inclination angle and feed rate is shown in figure 25(a). It can be seen that at a positive inclination angle of 45°, the ductile mode milling can be realized at the largest feed rate. By setting an inclination angle of +45°, Matsumura and Ono [131] successfully machined crack-free orthogonal grooves on glass, as shown in figure 25(b).

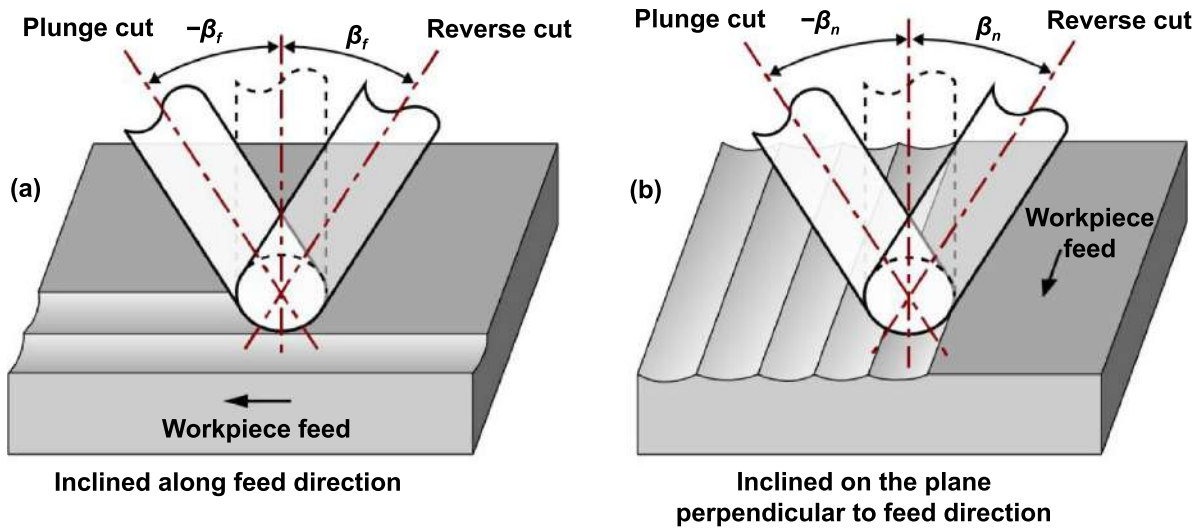

Figure 24. Schematics of inclination methods of ball-end cutter in ball-end milling.

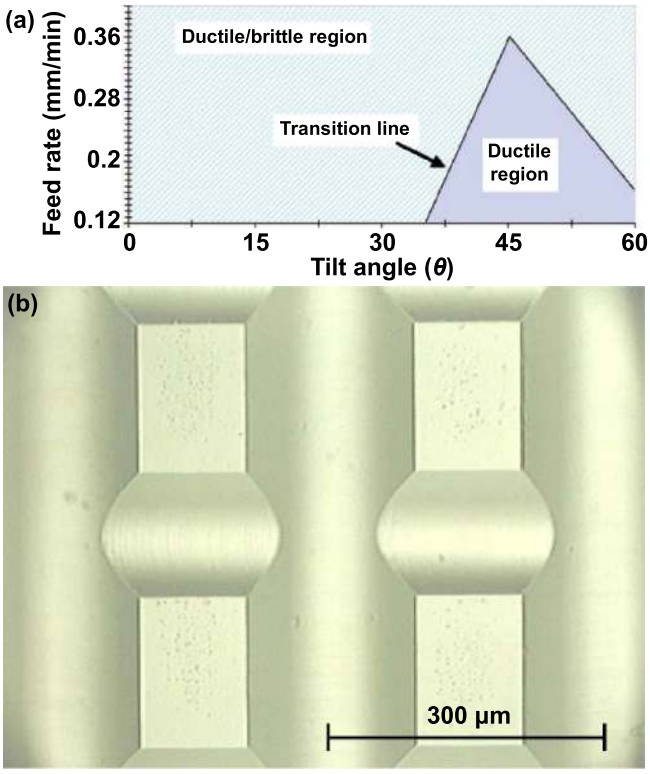

Figure 25. Ball-end milling of glass: (a) material removal mode in relation to inclination angle and feed rate [106] (Reprinted from [106], Copyright (2009), with permission from Elsevier); (b) machined orthogonal grooves by using a ball-end cutter at an inclination angle of 45° [131] (Reprinted from [131], Copyright (2008), with permission from Elsevier).

4. Ultraprecision grinding

Grinding is a complex material removal operation involving cutting, plowing, and rubbing depending on the extent of interaction between the abrasive grits and the workpiece material under the conditions of grinding [52]. Ultraprecision grinding is mostly used to produce high-quality surfaces made from hard-brittle materials. Through the multipoint cutting actions of ultrafine diamond grits, ultraprecision grinding can fabricate parts with high surface finish and high surface integrity at reduced tool wear compared to diamond turning [132]. However, in the grinding of soft-brittle materials, impurity embedding and poor ground surface quality are likely to occur under conventional grinding conditions [44]. To overcome this difficulty, researchers conducted a lot of attempts, including the optimization of grinding parameters [133], development of proper grinding fluid [134], and design of a binderless grinding wheel [135], and so on. Among them, the diamond grit's geometry considerably influences the quality of the machined surface [136].

4.1. Grit size

Diamond grits on grinding wheels inevitably have uneven size distribution and protruding heights. In the ductile grinding of soft-brittle materials, relatively uniform size distribution of grits tends to produce more ductile removal, while a significant protrusion may cause microfractures on the machined surface [137]. Thus, dressing and truing of wheels are necessary to narrow the size distribution and protruding height of diamond grits. Furthermore, diamond grits with a smaller average size, usually several micrometers or even less, are prone to offer a safer ductile grinding process [34].

Namba *et al* [138] used five different mesh sizes of diamond wheels to grind the (001), (111), and (110) planes of CaF_2 wafers. The average grit sizes on the five grinding wheels were 4, 6, 8.5, 11.5, and 18.5 μm, respectively. For each grinding wheel, through a series of experiments with different feed rates, the effects of feed rate and the grit size on the material removal mode were explored. It can be seen from figure 26 that although the absolute ductile grinding can only be achieved under low feed rate and grit size conditions, a finer grit size allows a relatively larger feed rate, especially on the (001) and

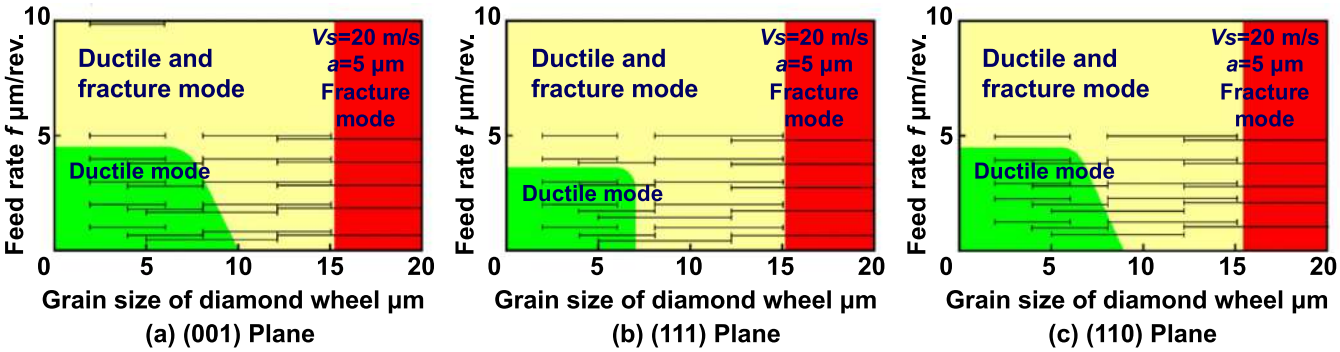

Figure 26. Grinding of CaF_2 crystal: change in material removal mode with feed rates and grit sizes of diamond wheels [138] (Reprinted from [138], Copyright (2005), with permission from Elsevier).

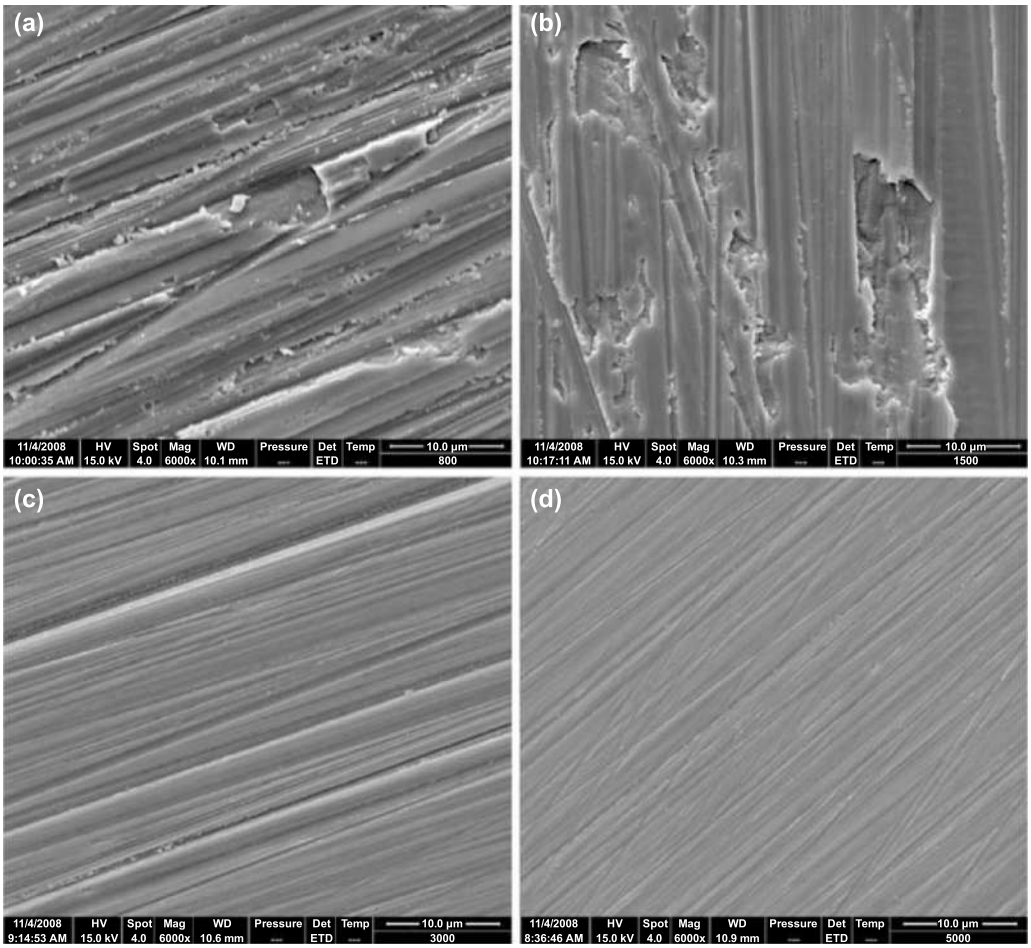

Figure 27. SEM images of the surfaces ground under a diamond wheel with mesh size of (a) #800, (b) #1500, (c) #3000, and (d) #5000 in the grinding of CdZnTe crystal [139] (Reprinted by permission from Springer Nature Customer Service Centre GmbH: Springer Nature, The International Journal of Advanced Manufacturing Technology. [139], Copyright (2010)).

(110) planes. The CaF_2 wafer of the (111) plane is most difficult to obtain a crack-free ground surface.

Zhang *et al* [139] preliminarily explored the ultraprecision grinding of CdZnTe crystal under four diamond wheels with different mesh sizes, including #800, #1500, #3000, and #5000, which corresponds to average grit sizes of 14, 8, 4, and 2.6 μm, respectively. They found that ductile grinding can be realized using #3000 and #5000 grinding wheels, and the best surface finish with average roughness Ra of 5.5 nm was obtained using the #5000 grinding wheel. The SEM images of the machined surfaces are presented in figure 27. Then, Zhang *et al* [140] characterized the subsurface damages of the CdZnTe crystal ground by #1500, #3000, and #5000 grinding wheels via cross-sectional TEM observation, as shown in figure 28. The results indicate that each sample has grinding-induced subsurface damages, but amorphous phases

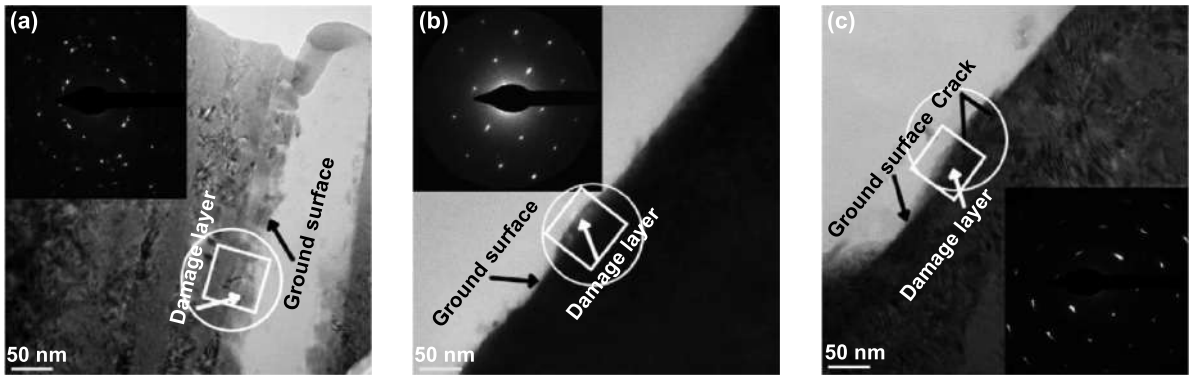

Figure 28. Cross-sectional TEM images of the subsurface ground under a diamond wheel with the mesh size of (a) #1500, (b) #3000, and (c) #5000 in the grinding of CdZnTe crystal. (The insets present their corresponding SAED patterns.) [140] (Reprinted from [140], Copyright (2010), with permission from Elsevier).

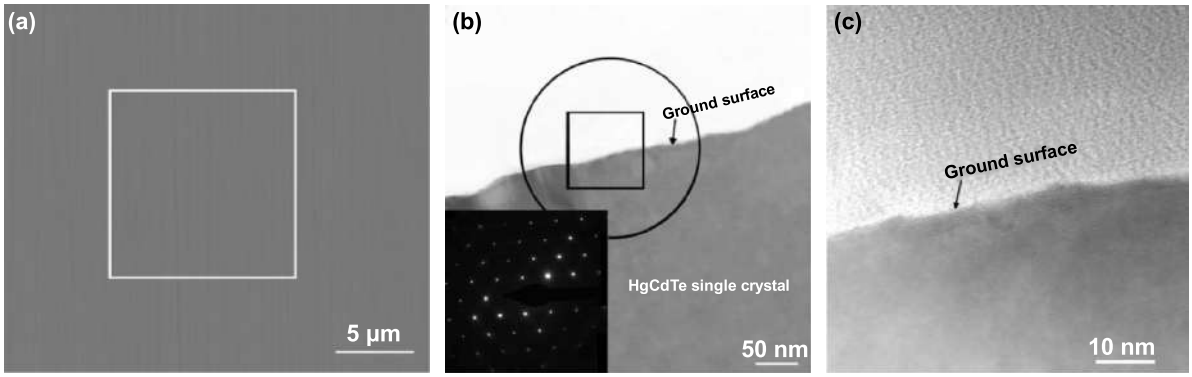

Figure 29. Grinding of HgCdTe crystal with a diamond wheel mesh size #15000: (a) SEM image of the ground surface. Cross-sectional TEM images of the ground subsurface (b) at low magnification (the insets present is SAED patterns), (c) at high magnification [145] (Reprinted by permission from Springer Nature Customer Service Centre GmbH: Springer Nature, Tribology Letters. [145], Copyright (2012)).

have not been formed in the subsurface. This result differs from those reported on grinding hard-brittle materials, such as silicon [141] and gallium oxide [142], in which both amorphous phases and crystallite defects are produced. The HR-TEM analysis revealed that the crystallite defects and nanocrystals are the main elements in the subsurface damage layer, and the extent of the damages in the subsurface layer decreased with decreasing grit size.

For this reason, Zhang *et al* [143] developed an ultrafine diamond wheel with mesh size #15000 (corresponding to an average grit size of 700 nm) to grind HgCdTe crystal. Ultimately, an ultra-smooth ground surface with a roughness 1.7 nm Ra was achieved, as shown in figure 29(a). The cross-sectional TEM images of the ground subsurface show that both the SAED patterns (see figure 29(b)) and monocrystalline lattice (see figure 29(c)) are perfect, indicating that a damage-free subsurface of HgCdTe crystal is achieved. Moreover, Zhang *et al* [144] noticed that the traditional model of maximum undeformed chip thickness (h_m) could not predict the real generated chip thicknesses well under such fine diamond grits; thus, they developed a novel model for calculating the h_m of the face grinding with ultrafine diamond grits, as follows [145]:

$$h_m = \frac{E_1}{E_2}\left[\frac{3}{C^{3/2}\tan\eta}\frac{v_f}{v_s}\right]^{1/2} \tag{6}$$

where E_1 and E_2 are the elastic moduli of the wheel and workpiece. C is a specific number of active surface grits per unit area. η is the half-included angle of the cross-section of a chip. v_f is the feed rate of the wheel, and v_s is the speed of the wheel.

4.2. Grit shape and orientation

Restricted by the dressing and truing techniques of diamond grit and the thermal conductivity of the bond of the grinding wheel, the size of diamond grit has a lower limit. Therefore, optimization of grit shape is another important way to enhance the ductile grinding of soft-brittle materials. Since a large number of abrasive grits of unknown shape and orientation participate in the grinding process and remove material from the workpiece, and the number of grits passing through the grinding zone per unit time is extremely large, it is necessary to use probabilistic statistics to analyze the machining mechanism of the grinding process. Because the sharp contact and blunt contact between grit and workpiece would cause a stress field of a

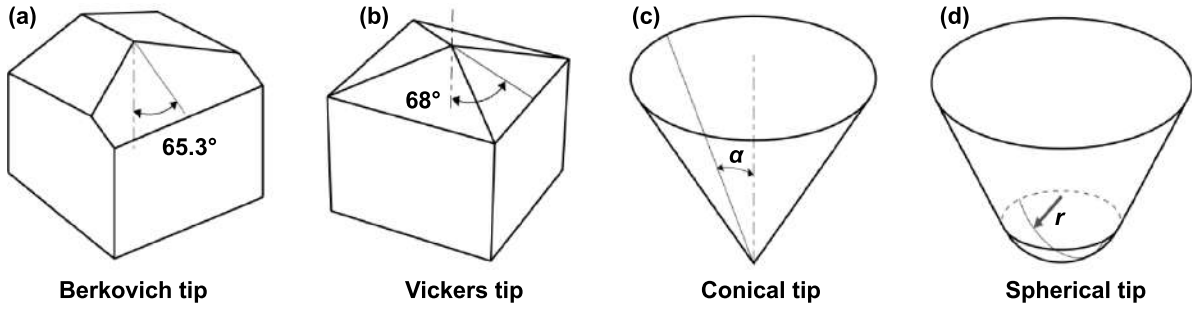

Figure 30. Schematic illustrations of four types of diamond stylus tools.

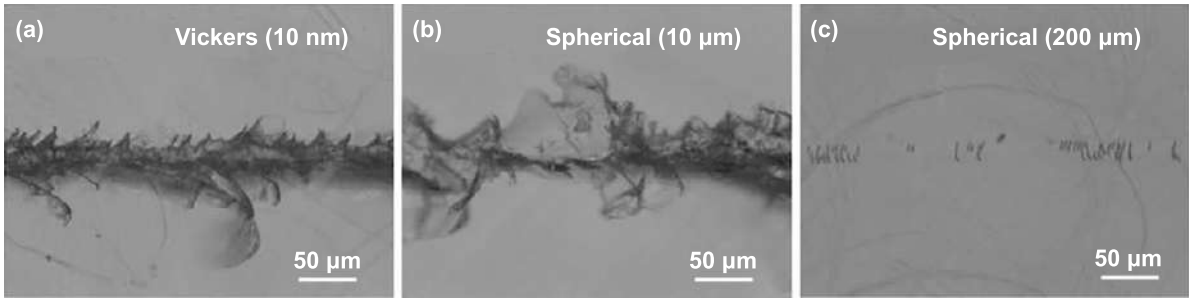

Figure 31. Optical images of the scratched grooves at a load of 500 mN by a Vickers tip and two spherical tips in the scratching of CaF_2 crystal. Reprinted from [147], Copyright (2020), with permission from John Wiley & Sons.

predominantly plastic (or quasi-plastic) response and predominantly elastic response, respectively, in the subsurface of the workpiece [37]. From this point of view, grits can be simply classified into two categories, namely, sharp grit and blunt grit. Although the plastic response tends to derive in sharp contact, at the same time, the stress concentrations are more intense and are thereby more likely to initiate crack growth in the brittle materials [146]. Therefore, it is necessary to conduct exploratory experiments to understand the effect of each grit shape on grinding soft-brittle materials.

Nanoscratching tests have been widely recognized as an effective method to explore material's DBT, fractures, and removal mechanisms. Since grit geometries are not identical, the diamond stylus tools with typical tip shapes, such as pyramidal, conical, and spherical tools, are usually used to simulate the different sharpness of grits. In this way, the machining characteristics related to the grit shape in the ultra-precision grinding of soft-brittle materials can be investigated. Figure 30 illustrates the schematics of four types of diamond stylus tools, which are commonly used in nanoscratching tests. Clearly, it is recognized that the Berkovich, Vickers, and conical tools with tip radius on the submicron scale are sharp. Material removal in terms of cutting and plowing can be realized in nanoscratching, using such sharp tools. By contrast, the spherical tool with a tip radius of several microns or larger is blunt. In nanoscratching, blunt tools can remove material through plowing and rubbing. Through analyzing the material deformation behavior caused by these shapes of indenter, it is possible to understand the role that various abrasive grit shapes play during grinding. Combining statistical analysis helps to optimize the number and distribution of various shapes of abrasive grits.

In the scratching of CaF_2 crystal, Suratwala *et al* [147] reported that a spherical tip (with a tip radius of 10 μm) generates comparable or greater damages to the workpiece compared with a sharp Vickers tip (with a tip radius of $\sim$10 nm), as shown in figures 31(a) and (b). However, when using a spherical tip having a larger radius ($\sim$200 μm) to scratch CaF_2 crystal, the damaged area of the workpiece is significantly reduced, and the scratched groove is so shallow that it is hardly visible, as shown in figure 31(c). This indicates that when the tool tip is below a certain sharpness value, a sharper tip will remove materials in a more ductile manner; however, if the tool tip is beyond a certain sharpness value, the deformation behavior of material will change to plowing-induced plastic deformation, that is, the material plastically flows down the tip, also resulting in material deformation in a ductile manner.

Similarly, in the nanoscratching of KDP crystal [148–150], at the normal force of 0.5 mN, a Berkovich tip (with a tip radius of $\sim$150 nm) generates the highest coefficient of friction (CoF, the ratio of measured lateral force to applied normal force); a conical tip (with a tip radius of $\sim$500 nm) generated a moderate CoF; while a spherical tip (with a tip radius of $\sim$1.22 μm) generated the smallest CoF. The corresponding morphology of the scratched grooves indicates that, at a lower load, the sharp tip can easily generate a strong stress field, facilitating the material removal in ductile mode; in contrast, the stress fields induced by the blunt tips are prone to cause plowing deformation of the material. However, when further increasing the normal load, the CoF of the blunt tip exceeds that of the sharp

Table 3. The critical load/depth of ductile-brittle transition of soft-brittle materials in nanoscratching tests.

Material	Tip geometry	Critical load/depth	Note
KDP	Conical (radius 0.5 μm)	1840 μN [151]	(001) plane Scratching direction [100]
KDP	Spherical (radius unknown)	1670 nm [a] 2850 nm [b] 1510 nm [c] [157]	(001) plane [a] Scratching direction [100] [b] Scratching direction [110] [c] Scratching direction [010]
KDP	Spherical (radius 5 μm)	420 nm [d] 3610 nm [e] [158]	Doubler plane Scratching direction $\perp$ [110] [d] At a temperature of 23 °C [e] At a temperature of 170 °C
CaF_2	Spherical (radius 2.5 μm, cone angle 45°)	3.25 mN [f] 2.5 mN [g] 0.25 mN [h] [159]	[f] Direction of 60° on (111) plane [g] Direction of 90° on (110) plane [h] Direction of 30° on (001) plane

tip, which indicates that the plowing effect weakens gradually with increasing scratching depth/load. Therefore, compared to a sharp tip, a blunt tip would produce higher tensile stress and cause a more severe brittle fracture of the material.

The tip-induced stress fields in the workpiece are not only determined by the tip radius, and the shape of the tip itself is equally important. Li *et al* [151] proposed a factor, equivalent half cone angle, to describe the combined effect of tool shape and tip radius, and then developed a predictive model for a critical load of ductile-to-brittle transition of KDP crystal. The predicted and experimental results show that the tip having a larger equivalent half-cone angle leads to a higher critical load of brittle fracture. Axinte *et al* [152] proposed a concept of an active number of cutting edges (NoCE) for diamond grit, ignoring the tip radius to investigate the influence of grit geometry on the grinding behavior of materials. Based on this concept, the conical and spherical tips belong to the circular frustum (active NoCE = 0), the Vickers tip and Berkovich tip belong to the square frustum (active NoCE = 2), and the triangular frustum (active NoCE = 3), respectively.

Active NoCE of 0 means circular symmetry, and hence the conical and spherical tips are commonly used for exploring the effect of crystal anisotropy on the values of critical load/depth of DBT and the friction coefficient [153–155]. Several representative experimental studies are listed in table 3. Through the MD simulation of nanoindentation and nanoscratching of KDP crystal, Yang *et al* [156] found that owing to the fact that all hydrogen bonds (H-bonds) are parallel with the (001) plane, but only 50% H-bonds are parallel with the (100) plane, the (001) plane has stronger resistance to deformation than the (100) plane in the normal direction. Thus, the atoms are much easier to compress on the (100) surface than on the (001) surface, as shown in figure 32. This clarifies, at an atomic level, why the extent of subsurface damages and elastic recovery of the material are highly sensitive to crystal planes.

However, a tip with large active NoCE is preferred to better simulate the irregular diamond gits on the grinding wheel. Therefore, the Berkovich tip having three side faces (also having three edges) is thought to be closer than other tips to the geometry of the grits [160]. Huang and Yan [161] used a Berkovich tip to conduct nanoscratching tests along the face-forward (FF) and edge-forward (EF) directions on the ZnSe poly-crystal. The morphologies of the grooves scratched in the two directions are shown in figure 33. It can be seen that material removal in a ductile mode was obtained in the EF scratching direction, while brittle fractures occurred in the FF scratching direction. The Raman spectra indicate that tensile residual stress and compressive residual stress are dominant in the subsurface of the scratched groove in the FF and EF directions, respectively. Besides, in both grooves, dense and clear fishbone-like patterns caused by stick-slip motion between the tip and the material can be observed even under an extremely small load. This is quite different from the fishbone-like patterns reported in hard-brittle materials [162–165] and is supposed to be caused by the low hardness of ZnSe crystal.

5. Micro/nano burnishing

Most soft-brittle materials in table 1 are highly toxic to the human body. Table 4 presents the potential health effects/symptoms associated with their toxicity. Ultraprecision turning, grinding, and end milling processes will generate submicron scale powder-type chips, which are easily inhaled and can cause severe health hazards to operators. Therefore, the machine tools must be equipped with chip collection vacuum systems, and the operators must wear protective equipment during those material removal processes, which greatly increases the production costs and process complexity; even then, health risks to operators still exist.

Burnishing is a surface finishing method that plastically deforms the workpiece surface without material removal [173, 174]. A schematic diagram of a ball burnishing process is shown in figure 34. Conventional burnishing is usually conducted on metals for making surface conditioning, such as enhancing surface smoothness, wear resistance, and corrosion resistance; closing porosity; and creating compressive residual stresses [175, 176], in which a ball-shaped tool with

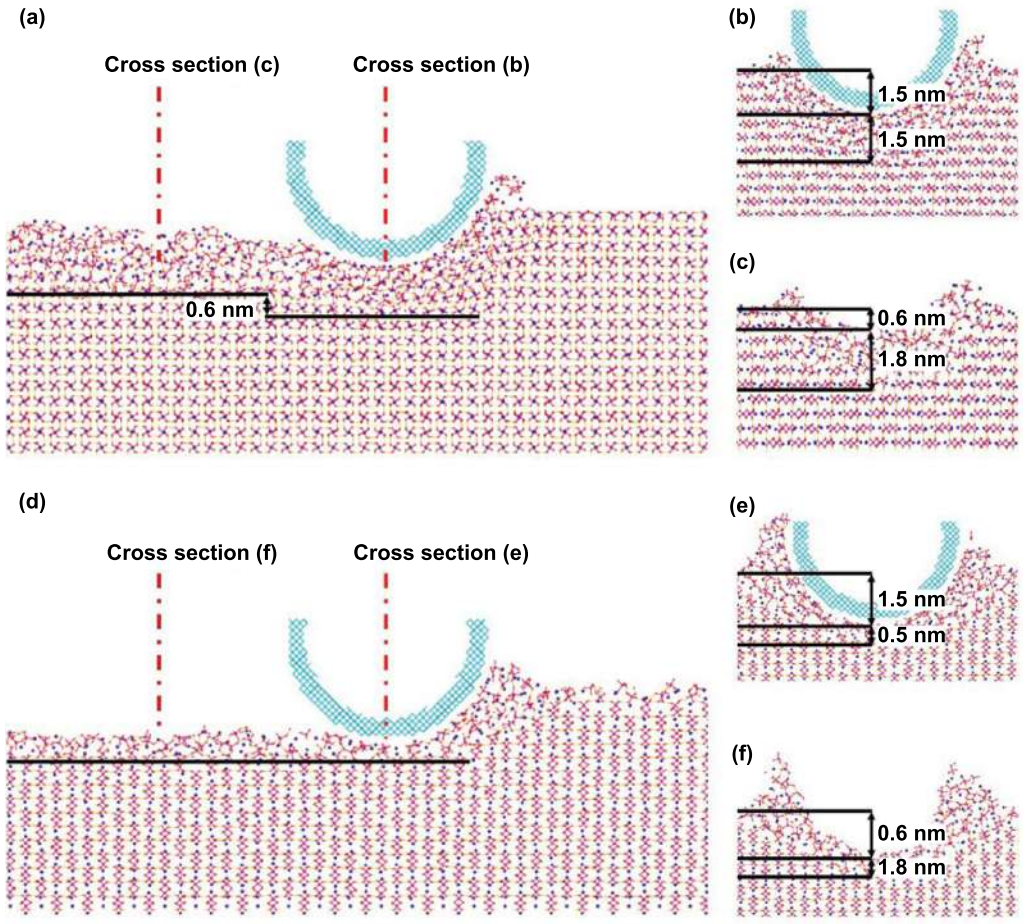

Figure 32. Atomic distribution of KDP crystal: (a) side view, (b) cross-section during the scratching, and (c) cross-section after scratching, when nanoscratching on (100) surface; and (d) side view, (e) cross-section during the scratching, and (f) cross-section after scratching, when nanoscratching on (001) surface [156] (Reprinted from [156], Copyright (2021), with permission from Elsevier).

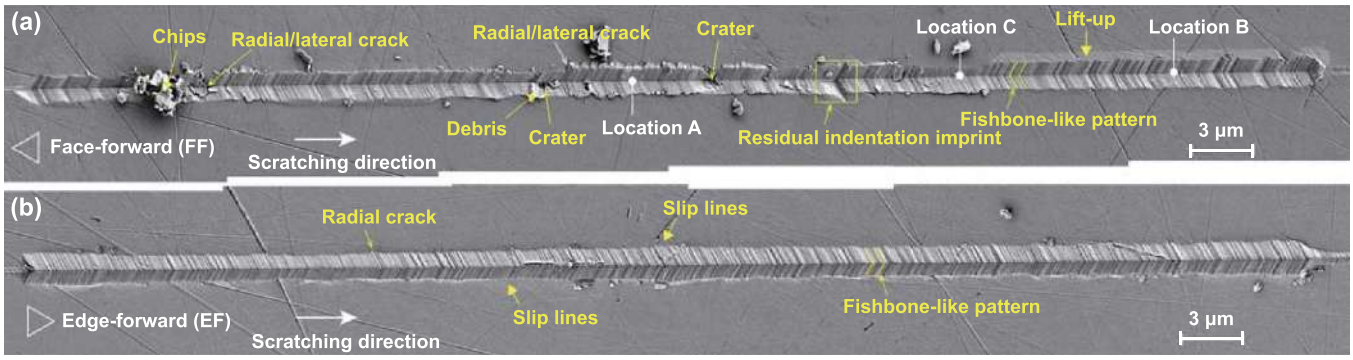

Figure 33. Scratching of ZnSe poly-crystal: SEM images of the groove morphologies resulting from Berkovich tip scratching at the load of 1 mN in the (a) face-forward direction and (b) edge-forward direction [161] (Reprinted from [161], Copyright (2021), with permission from Elsevier).

a millimeter-level radius is used, and the burnishing force is up to several tens of Newtons [177, 178]. Under these conditions, local plastic deformation of workpiece material occurs below the ball tool without any burr or chip formation due to the extremely small ratio of burnishing depth to tool tip radius.

In ultraprecision machining, where the undeformed chip thickness is usually smaller than or comparable to the cutting tool edge radius, chip formation may also not occur, i.e. no material removal happens, due to the highly negative rake angle of the tool. This situation is very similar to conventional burnishing and tends to happen when the tool edge radius is on

Table 4. The potential health effects/symptoms of toxic soft-brittle materials.

Material	Potential health effects/symptoms	References
CdZnTe	Toxic if swallowed. Fatal if inhaled. May cause cancer. Suspected of damaging fertility or the unborn child. Causes damage to organs through prolonged or repeated exposure.	[166]
HgCdTe	Mercury mainly affects the nervous system. Acute inhalation of cadmium fumes results in metal fume fever. Ingestion of cadmium causes vomiting and diarrhea.	[167]
BaF_2	Effects on reproductive health. Symptoms of somnolence (general depressed activity).	[168]
ZnSe	Toxic if swallowed. Toxic if inhaled. Acute toxicity. Causes damage to organs through prolonged or repeated exposure.	[169]
KDP	Skin symptoms: redness. Respiratory symptoms: cough. Symptoms of somnolence (general depressed activity). Functional changes in the gastrointestinal system.	[170]
CaF_2	Effects on fertility. Alters teeth and supporting structures. Induces a change in blood or tissue levels.	[171]
ZnS	Brain and coverings: changes in circulation. Blood: changes in leukocyte (WBC) count.	[172]

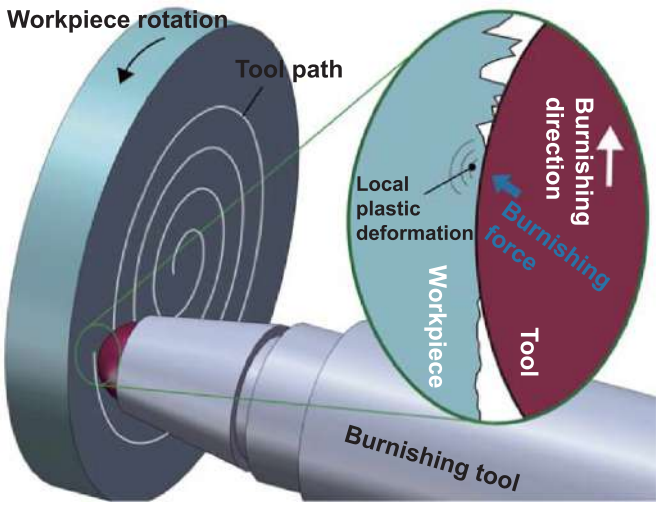

Figure 34. Machining model of ball burnishing process.

a micrometer-level and undeformed chip thickness is on a nano scale. Therefore, in micro-nano scale, burnishing can deform soft-brittle materials without brittle fractures and can create shapes on workpiece surfaces like machining. At the same time, the roughness of the machined surface can be improved. Therefore, in the micro-nano scale, burnishing is an important extension of machining.

By using a spherical diamond stylus tool with a radius of 10 μm, under the burnishing force of 2 mN, Huang and Yan [179] successfully made a groove-crossing grid and groove-overlapping grid patterns on the surface of ZnSe polycrystal, as shown in figure 35, demonstrating the possibility of manufacturing microstructures on toxic soft-brittle materials without chip generation. The deepest part of the patterns reached about 30 nm. When the burnishing force increased to 5 mN (the corresponding depth was around 120 nm), cracks started to grow on the surface. When the burnishing force increased to 10 mN (the corresponding depth was around 208 nm), though more cracks appeared on the burnished surface, the material was still plastically deformed without chip generation. The subsurface damages of the burnished surface at the load of 10 mN were characterized via cross-sectional TEM observation, as shown in figure 36(a). It was found that lattice distortions and dislocations occurred within the shallow subsurface due to the micro/nano burnishing, but no amorphization was observed. Moreover, the workpiece material directly beneath the tip suffered a combined effect of shear stress and tensile stress, and as a result, crack propagation not only occurred along the direction parallel to the slip band but also tended to deflect in the direction perpendicular to the burnishing direction, as highlighted in the red box. According to electron backscatter diffraction analysis (see figures 36(b)–(d)), it is clear that the extent of subsurface damage in each grain was different due to the varied grain orientations and the blocking of grain boundaries. This preliminary experiment indicated the feasibility of burnishing soft-brittle materials, but the brittle fracture could occur before material removal. In other words, the brittleness of the material largely determines the depth of ductile burnishing.

6. Comparison of machining mechanisms

The machining characteristics of soft-brittle materials are affected by processing methods with different geometries of tools. The main features of turning, end milling, grinding, and burnishing processes for the ultraprecision machining of soft-brittle materials are listed in figure 37. Specifically, the cutting tools for turning and end milling have similar geometry of tool edge, though their tool tip has different shapes; therefore, the mechanisms of material removal and surface formation during turning and end milling are similar. In general, a tool with a negative rake angle (-20° to -45°) and a relief angle ($\sim 9^\circ$) is recommended to enhance the hydrostatic pressure beneath

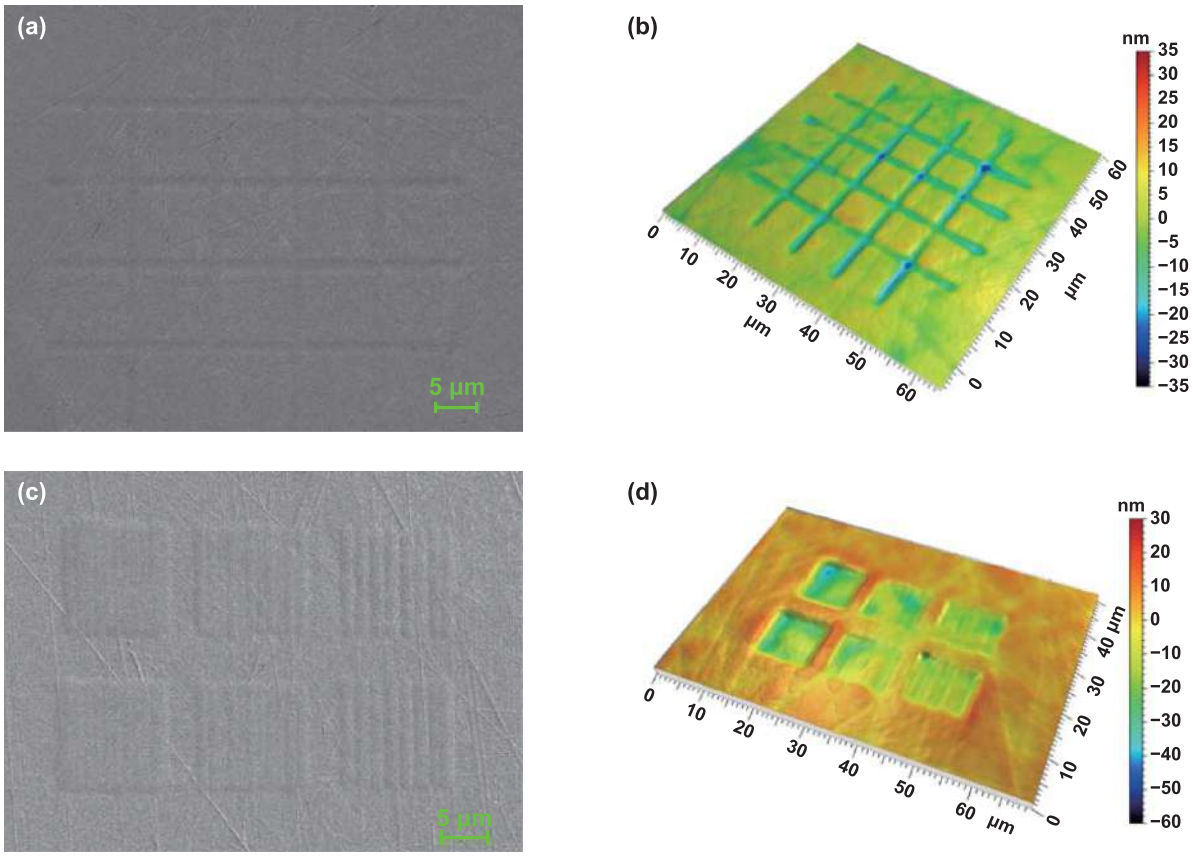

Figure 35. Micro/nano burnishing of ZnSe poly-crystal: (a) SEM image and (b) 3D topography of a groove-crossing grid microstructure; (c) SEM image and (d) 3D topography of a groove-overlapping grid microstructure [179] (Reprinted from [179], Copyright (2021), with permission from Elsevier).

the tool during turning and end milling, which leads to ductile mode machining of soft-brittle materials [92, 119]. Furthermore, a sharp cutting edge is preferred because it promotes shear deformation of workpiece material and suppresses the plowing effect during cutting. It is important to note, however, that the cutting edge of a milling cutter is much blunter than that of a single-point diamond tool for turning due to the restrictions of tool materials (e.g. sintered materials). Hence, the roughness of a milled surface is not as good as that of a diamond-turned surface. A blunt edge induces a highly negative effective rake angle, causing a significant plowing effect that deteriorates the surface finish. Nonetheless, given the fact that the milling cutter performs a rotary movement (primary motion), the burrs due to the plowing effect may be removed by the multiple tool passes of a rotating tool with a transverse feed motion. As a result, microgrooves with a very smooth surface can be created due to the cross-smoothing effect, even though the tool edge itself is not smooth with protrusions or wear marks [96].

Different from the tools of turning and end milling processes, which have well-defined edge geometry, the grits of grinding have random geometries and edge/face orientations. In general, fine, and uniform diamond grits are more likely to cause material removal in a ductile mode [138]. Additionally, the orientation of grit greatly affects the deformation behavior of the material, as demonstrated by nanoscratching tests. In particular, shear deformation in front of the tool tip is the predominant deformation behavior in the scratch in the FF direction, whereas the side flow of the material dominates the deformation behavior during scratching in the EF direction. Consequently, tensile residual stress was dominant in the subsurface of the scratched groove in the FF direction. In contrast, compressive residual stress was dominant in the subsurface of the scratched groove in the EF direction [161]. However, the surface is enveloped by multiple passes of randomly distributed/oriented grains in an actual grinding process. Thus, the sharp grits-induced large ratio of machining depth to tool edge radius may produce material shearing and extrusion; the blunt grits-induced small ratio of machining depth to tool edge radius may cause a plowing and rubbing effect. By optimizing the grinding conditions, the statistical nature of grinding can make a surface smooth and uniform.

From diamond turning to micro end milling, the tool edge radius is increased, and the material removal behavior changes from shearing and extrusion to extrusion and plowing. If the tool edge radius is significantly increased, the tool can be used for burnishing. In the burnishing process, no material will be removed from the workpiece, i.e. no chip/debris formation, but the material undergoes local plastic deformation [179]. This is realized by an extremely small ratio of burnishing depth to tool edge radius; meanwhile, the burnishing depth is controlled at tens to hundreds of nanometers. After the burnishing process,

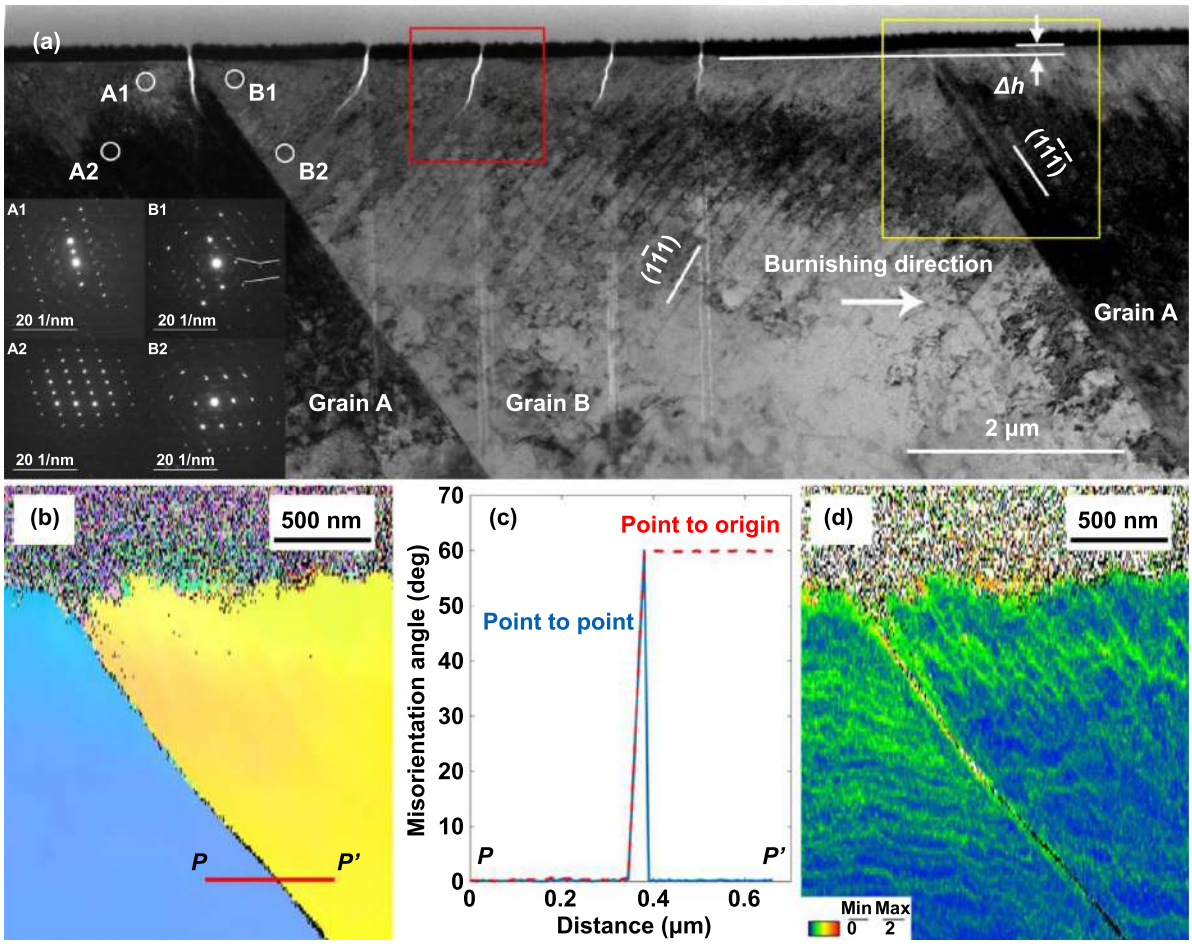

Figure 36. Results of micro/nano burnishing of ZnSe poly-crystal: (a) an overall cross-sectional TEM image of the subsurface of burnished groove; figures A1, 2, and B1, 2 are SAED patterns of corresponding areas circled in (a). (b) IPF map of the region outlined by the yellow box in (a). (c) Misorientation angle profile along Line PP′ marked in (b). (d) KAM map of the region outlined by the yellow box in (a) [179] (Reprinted from [179], Copyright (2021), with permission from Elsevier).

compressive residual stresses in the subsurface will be created, and the smoothness of the surface can be improved.

Although soft-brittle and hard-brittle materials can be machined in ductile mode, they exhibit distinct hardness, leading to different machining characteristics. Table 5 compares the differences between the machining characteristics of soft-brittle and hard-brittle materials. For processing soft-brittle materials, there are few reports on the amorphization of machined subsurfaces. Their subsurface damage includes mainly dislocations, nanocrystals, and lattice distortions [69, 80, 140, 179]. Figure 38(a) shows a TEM image for the subsurface of CaF_2 crystal as an example. In contrast, the amorphous phase in the machined subsurface of hard-brittle materials is significant, and the thickness of the amorphous layer is affected by the geometry of cutting tools [32, 141]. Figure 38(b) shows a TEM image for the subsurface of Si crystal as an example. The reason why the soft-brittle materials can hardly generate an amorphous phase may be attributed to the relatively low hydrostatic pressure during machining, which is caused by the low hardness of the workpiece material [17]. As a result, the phase stability of the lattice structure cannot be broken at low hydrostatic pressure. Therefore, the phase transformation of the material may not occur or be reversible after decompression [180], but the damages in terms of dislocations, nanocrystals, and lattice distortions are formed and remain in the subsurface. Besides, the low hardness of soft-brittle materials can also cause different surface morphology. In the nanoscratching tests using a sharp Berkovich tip, dense and clear fishbone-like patterns start to form on soft-brittle material at an extremely small load, as shown in figure 38(c) [161]. This is because stick-slip behavior occurs during nanoscratching. In the stick state, the creep deformation is significant due to the low hardness of the material. Therefore, the fluctuation of the penetration depth of the indenter is significant when the stick and slip state alternate. However, for the nanoscratching of hard-brittle materials; though stick-slip behavior occurs as well, the creep deformation is not significant. Therefore, the critical load for the formation of fishbone-like patterns is higher, and the formed patterns are sparse and shallower (see figure 38(d)) [162–165]. As affected by different hardness, some other material properties, such as thermal conductivity, thermal expansion coefficient, elastic modulus, etc, may become more influential in the formation of microfractures. Consequently,

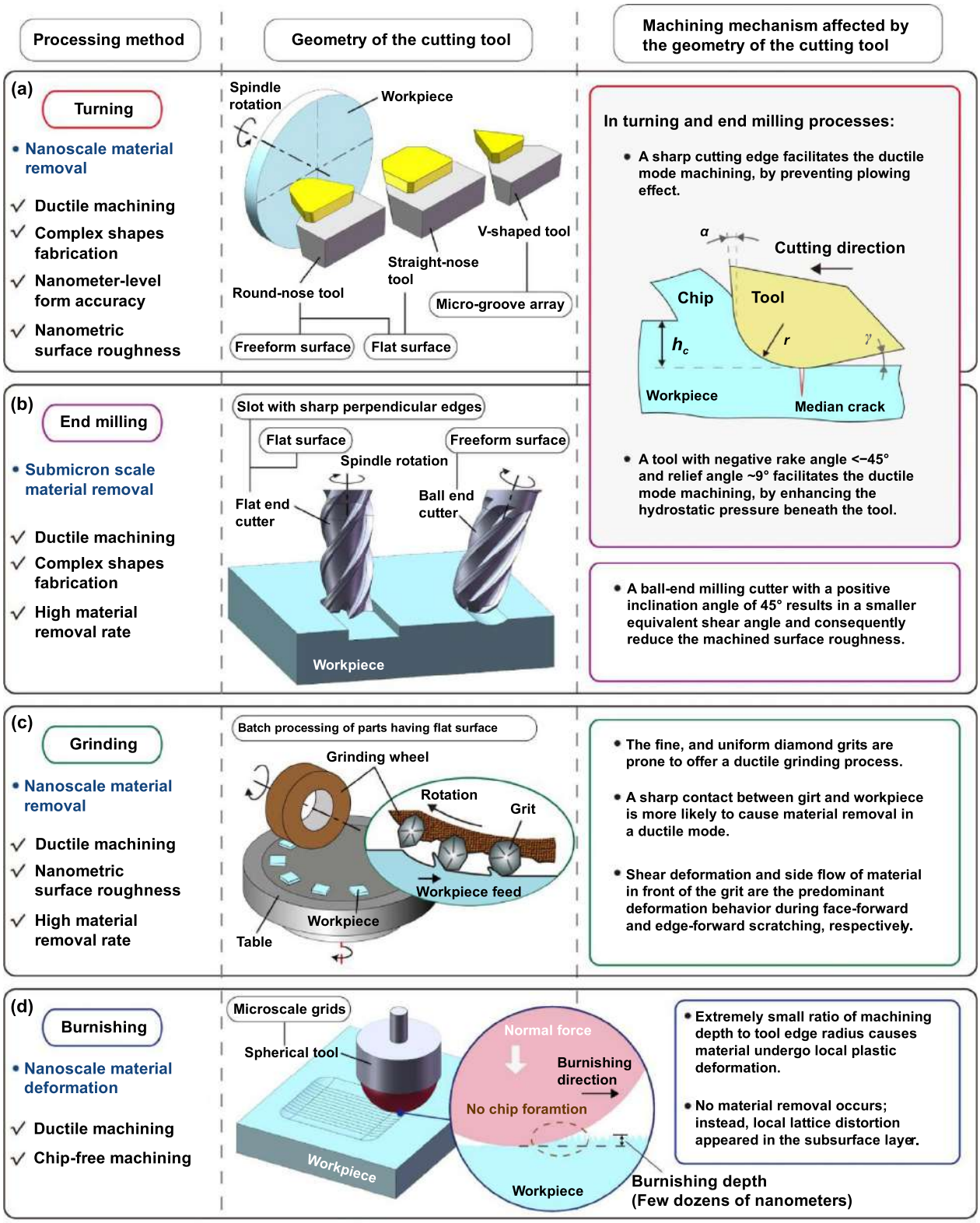

Figure 37. The main features of various processing methods for the ultraprecision machining of soft-brittle materials.

in addition to generating micron-sized craters, which are similar to those defects observed in hard-brittle materials, on the machined surface of soft-brittle materials, hundreds of microns of craters and submicron pits could also be formed under certain special machining conditions. For example, the former can be generated on CaF_2 crystal, as shown in figure 38(e), when cutting fluid is applied and the tool feed rate is low. This is caused by the thermal effects because of the low thermal conductivity and high thermal expansion coefficient of the material [77]. The latter can be generated on ZnSe

Table 5. Comparison of the differences between machining characteristics of soft-brittle and hard-brittle materials.

Types of materials		Subsurface damages and surface morphologies		
		Microstructural changes	Surface patterns	Microfracture types
Soft-brittle materials	Phenomena	No phase transformation during turning [17, 69, 80], and grinding [140]	Low critical load for the formation & dense distribution in nanoscratching [161]	Submillimeter-sized crater [77] & submicron pits [17] in turning
	Features	Dislocations without amorphous phase (see figure 38(a)) 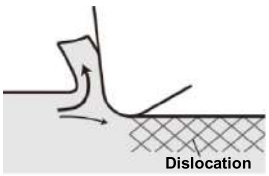	Dense fishbone-like patterns (see figure 38(c)) 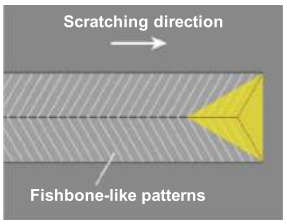	Submillimeter-sized crater (see figure 38(e)), and submicron pits (see figure 38(f)) 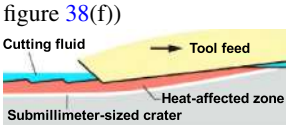 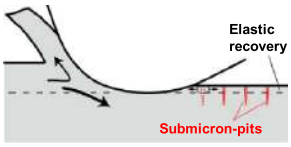
	Mechanisms	Low machining pressure is produced due to the low hardness of material. Phase stability of the lattice structure cannot be broken at the low machining pressure.	Stick-slip behavior occurs during nanoscratching. Creep deformation is significant due to the low hardness of material.	Submillimeter-sized crater is caused by the thermal effects. Submicron pits are caused by the tearing effects during material elastic recovery.
Hard-brittle materials	Phenomena	Phase transformation during turning [32, 181] and grinding [141, 142]	High critical load for the formation & Sparse distribution in nanoscratching [162–165]	Few microns craters [76, 91, 182] in turning
	Features	Dislocations with amorphous phase (see figure 38(b)) 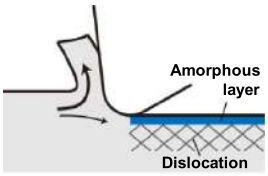	Sparse fishbone-like patterns (see figure 38(d)) 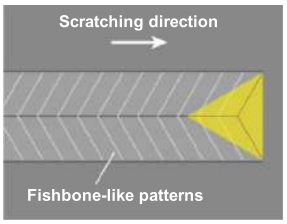	Few microns craters (see figure 38(g)) 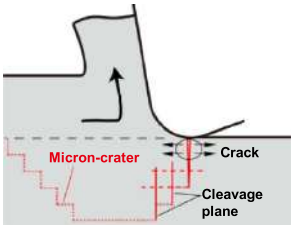
	Mechanisms	High machining pressure is produced due to the high hardness of material. Phase stability of the lattice structure is broken at the high machining pressure.	Stick-slip behavior occurs during nanoscratching. Creep deformation is insignificant due to the high hardness of material.	Large tensile stress is concentrated in the vicinity of the cutting edge, and cleavage fractures initiate as the tool advances.

crystals, as shown in figure 38(f), when a large relief angle tool is used, and the tool feed rate is low. This is caused by the tearing effects during the elastic recovery of the material, because of the significant plastic flow of material beneath the tool [17]. By contrast, for hard-brittle materials, the surface damages are usually micron-sized craters (see figure 38(g)), which are formed under a large feed rate. Because large tensile stress is concentrated in the vicinity of the cutting edge, and cleavage fracture initiates as the tool advances due to the low fracture toughness of the material.

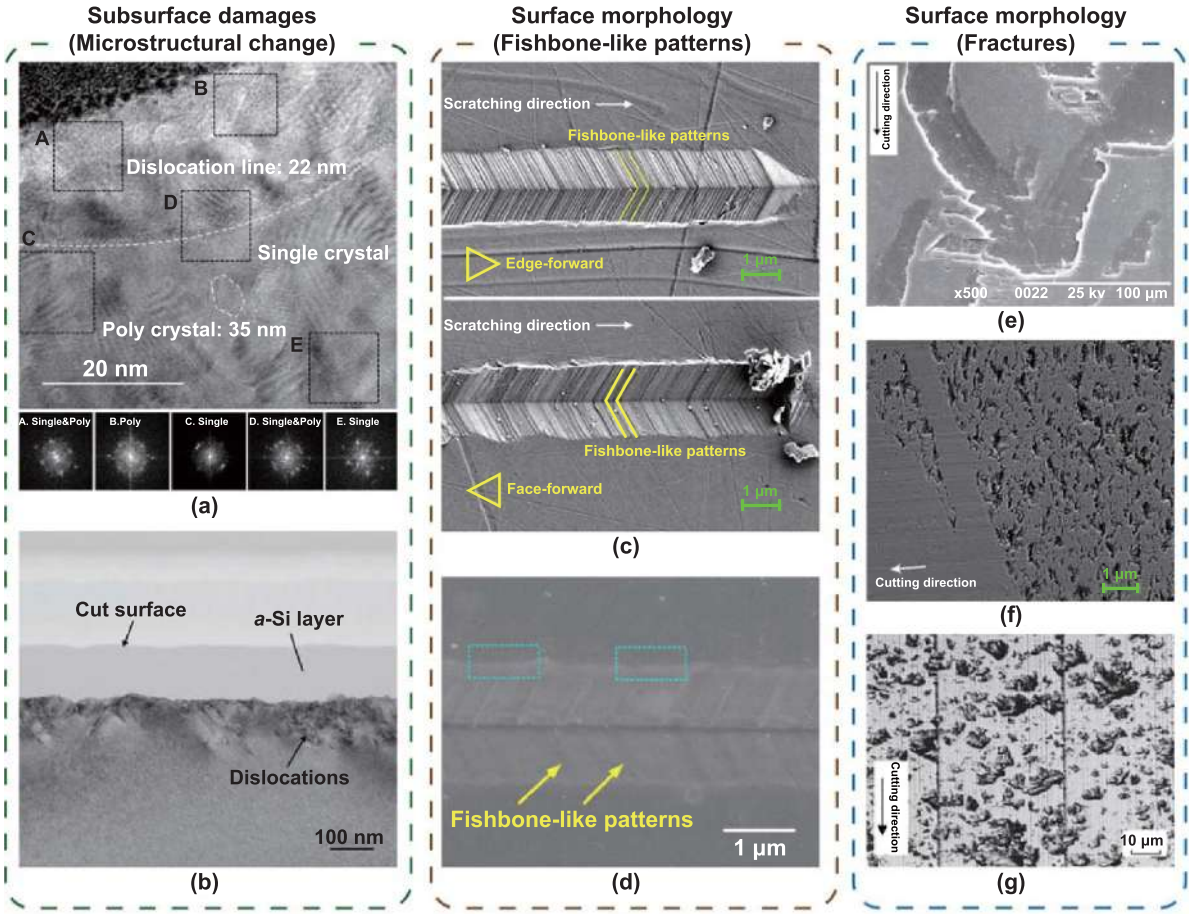

Figure 38. Typical features of the subsurface damages and surface morphologies of soft-brittle and hard-brittle materials: (a) dislocation in CaF_2 subsurface [69] (Reprinted from [69], Copyright (2015), with permission from Elsevier), (b) phase transformation in Si subsurface [32] (Reprinted from [32], Copyright (2009), with permission from Elsevier), (c) dense fishbone-like patterns on polycrystalline ZnSe surface [161] (Reprinted from [161], Copyright (2021), with permission from Elsevier), (d) sparse fishbone-like patterns on Lu_2O_3 surface [164] (Reprinted from [164], Copyright (2018), with permission from Elsevier), (e) hundreds-of-microns sized crater on CaF_2 surface [77] (Reprinted by permission from Springer Nature Customer Service Centre GmbH: Springer Nature, The International Journal of Advanced Manufacturing Technology [77], Copyright (2004)), (f) submicron pits on polycrystalline ZnSe surface [17] (Reprinted from [17], Copyright (2020), with permission from Elsevier), (g) few microns craters on Si surface [76] (Reprinted from [76], Copyright (2002), with permission from Elsevier).

7. Summary and outlook

7.1. Summary

Soft-brittle materials have important applications in optic and optoelectronic industries, but their ultraprecision machining is difficult. Due to the low hardness, the machining characteristics of soft-brittle materials differ from those of hard-brittle materials. Moreover, the machining mechanisms of soft-brittle materials in various processing methods are different. In this article, major types of ultra-precision machining technologies of soft-brittle materials, which utilize tools with different geometries, were reviewed and compared. The special features of the machining mechanisms of soft-brittle materials and the different/common aspects among different processing methods were identified.

Some key points for the individual processing methods are listed below.

- In ultraprecision diamond turning, a tool with a large tool nose radius, negative rake angle, and small edge radius is beneficial to the ductile machining of soft-brittle materials. However, this tool geometry may also cause more serious subsurface damages, such as dislocations and phase transformation. Nonetheless, no subsurface amorphous layer is generated on the machined surface of soft-brittle materials because the phase transformation generated in machining is reversible after decompression. This results in a stronger anisotropy behavior in the machining of soft-brittle materials. Thermally-induced cracks occur for soft-brittle materials but do not occur for hard-brittle materials.
- In micro end milling, a cutter with a ball-end shape and a sharp cutting edge is desired, which is useful for repairing micro-defects in soft-brittle materials. A negative rake angle cutter with a positive inclination angle is beneficial for the ductile mode machining of soft-brittle materials.

Table 6. Summary of machining characteristics of various processing methods for ultraprecision machining soft-brittle materials.

Machining method	Tool geometry	Machining mechanism	Applications
Diamond turning	Specific shape, rake angle, and relief angle Sharp edge radius	Material removal at the nanoscale by shear deformation and extrusion	Fabricating flat and complex-shape surfaces, such as freeform surfaces and microgroove structures
Micro end milling	Specific shape, rake angle, and relief angle Moderate edge radius	Material removal at submicron scale by extrusion and plowing	Fabricating slot with sharp perpendicular edges Repairing micro-defects on the large-size parts
Ultraprecision grinding	Random shape, size, and orientation	Material removal at the nanoscale by multiple passes of grits through shear deformation and side flow	Batch processing of parts having a flat surface Fabricating microgroove structures
Micro/nano burnishing	Specific shape and blunt tip radius	Nanoscale local plastic deformation of material occurs below the tool without material removal	Producing micro/nanoscale surface structures

- In ultraprecision grinding, the extent of the damages in the machined subsurface layer decreases with decreasing grit size. Amorphous phase has not been formed in the subsurface of ground soft-brittle material, which is different from that in the grinding of hard-brittle materials. Nanoscratching tests indicate that dense and clear fishbone-like patterns will form on soft-brittle material even under extremely small loads due to its low hardness.
- In micro/nano burnishing, soft-brittle materials can be plastically deformed without generating cutting chips, which is useful for preventing health hazards when machining toxic soft-brittle materials. Micro/nanoscale surface structures can be fabricated on soft-brittle materials in a ductile mode under the condition that a ball-shaped tool has a micrometer-level radius and the burnishing depth is controlled on the nanometer scale. Local lattice distortion appears in the subsurface layer due to plastic deformation, but no phase transformation occurs.

Based on the review of individual processing methods, a comparison of tool geometries, process mechanisms, and applications can be made, as summarized in table 6.

Ultraprecision diamond turning, micro end milling, and ultraprecision grinding are material removal processes. Among them, turning and grinding can achieve nanometric surface roughness by nanoscale material removal, which results from the single-point cutting actions of an extremely sharp cutting edge (tens of nanometers) and the multipoint cutting actions of ultrafine diamond grits (a few microns), respectively. For ductile mode diamond turning, the material is mainly removed by shear deformation and extrusion, being jointly determined by the undeformed chip thickness and edge radius of the tool. In contrast, for ductile mode grinding, the material is removed by shear deformation and side flow, which depends on the orientation of the grits. Since the material is scratched by multiple passes of the randomly distributed and orientated grits, the statistical nature of grinding can make a surface smooth and uniform. Milling generates submicron-scale material removal using relatively blunt cutting edges, which has a higher material removal rate but causes rougher machined surfaces. This is because, in addition to shearing and extrusion deformation like turning, the material may undergo plowing deformation due to the relatively small ratio of undeformed chip thickness to tool edge radius.

Turning and milling can fabricate complex shapes on soft-brittle materials, and their machining mechanisms are similar, though their tool edge radius is different. A sharp tool edge and a negative tool rake angle are generally preferred in cutting and milling to achieve ductile mode machining. Grinding is suitable for batch-processing flat surfaces on soft-brittle materials using many diamond grits with random shapes and sizes. Since a sharp contact between grit and workpiece within a subthreshold (crack-free) yield zone is prone to offer a ductile mode material removal, fine and uniform diamond grits are preferred to achieve ductile mode machining.

Micro/nano burnishing is a surface layer deformation process without material removal, and thus is an eco-friendly machining method for toxic soft-brittle materials. During the burnishing of soft-brittle material, local plastic deformation of material occurs below the tool without any burr or chip formation by using a ball-shaped tool having a micrometer-level radius and controlling the burnishing depth at a nanoscale. This method can be applied to producing micro/nanoscale surface structures on soft-brittle materials.

7.2. Future perspectives

To advance the engineering applications of ultraprecision machining of soft brittle materials, a few future perspectives are given as follows:

7.2.1. Process optimization. Although several works have focused on the ultraprecision machining of soft-brittle materials, the fundamental research is still limited compared to that of hard-brittle materials. Currently, the machining conditions are usually selected empirically based on those of hard-brittle materials. Additionally, many auxiliary machining methods have been developed for machining hard-brittle materials, such as ion implantation-assisted machining and laser-assisted machining [183]. However, since the essential purpose of these methods is to reduce the hardness of the materials, they are not very effective for processing innately soft materials. There are many different machining characteristics between soft-brittle and hard-brittle materials, as presented in table 5. For example, one important difference is that hydrostatic pressure in the machining region of soft-brittle material is relatively lower, which makes the material more susceptible to tensile stress during processing, resulting in brittle fractures. Developing an enhanced localized hydrostatic pressure-assisted machining device may be helpful for the ductile machining of soft-brittle materials. Therefore, the optimization of machining conditions and developing auxiliary machining methods for soft-brittle materials based on their special features is an important task.

7.2.2. Chip disposal. Most soft-brittle materials listed in table 4 are highly toxic. Due to the soft brittle nature of the material, the chips are easily broken into submicron scale powders. Submicron scale powder-type chips generated in turning, milling, and grinding processes are easily inhaled and cause severe health hazards to operators. Therefore, chip disposal in machine tools must be considered to prevent the operators from inhaling or exposing to those toxic powders. This is a major factoring limiting the advance of the machining technology of soft brittle materials. A higher-standard laboratory environment is required when performing experiments on these materials. Therefore, a portable, universal, and efficient chip collection unit is necessary for machine tools in the laboratory and would consequently promote the research from the institution's side. After releasing the health hazards and pollution concerns, the effects of temperature and cutting fluids on the material removal behaviors need to be systematically investigated.

7.2.3. Cutting fluids. In the machining of metals and hard brittle materials, cutting fluids can decrease tool-chip friction and flush away chips, thus providing better dimensional accuracy and finish on the workpiece [184]. However, cutting fluids may deteriorate the machined surface quality of soft-brittle materials. This is because thermal cracks can occur during the wet machining of CaF_2 crystal and other soft-brittle materials that possess low thermal conductivity and a high thermal expansion coefficient. In addition, KDP crystal and some halogenide single crystals, such as LiF and NaCl, are hygroscopic and deliquescent. Condensation of water vapor onto the crystals will cause surface degradation [185]. Although it has been reported that light mineral oil can be used as the cutting fluid and subsequently cleaned by toluene [186], the processing environment is not eco-friendly and is a hazard to operators. Today, dry cutting conditions with precise humidity control are usually used in the diamond turning of hygroscopic and deliquescent materials. As an alternative, there is a demand for the development of special cutting fluids for machining hygroscopic and deliquescent materials. For the machining of polymers, the chip adhesion on the cutting tool, which is caused by the low melting point of the material and the high temperature generated in the heat-affected zone during machining, would inevitably produce adhesive tool wear and a poor surface finish on the machined part. Developing cutting fluids that is highly effective in cooling and lubricating has been considered the key to lowering the adhesive tool wear [187].

7.2.4. Edge chipping prevention. Owing to the low hardness property, when cutting tools start machining the workpiece from the edge to the center, chippings are easily formed along the edge, though the inner area can be machined in ductile mode. The cracks that extend from the edge will greatly reduce the usable area of lenses and decrease the optical performance and lifespan of the functional parts. Similarly, fabricating sharp edge structures, such as groove arrays, on soft-brittle materials without chipping is also challenging, as mentioned in figures 13 and 23. Preliminary experiments have shown that workpiece pre-coating effectively prevents crack formation at the groove edges when cutting micro V-shaped grooves on the soft-brittle material [78]. However, the coated material may also bring other problems, such as causing tool chatter and being difficult to clean off the workpiece. Therefore, further development of workpiece pre-coating to help inhibit edge chipping is desired. In addition, vibration-assisted machining is an effective method to reduce instantaneous cutting force; thus, this method may be helpful in suppressing the formation of chipping on sharp edge structures of soft-brittle materials. However, this opinion has yet to be verified, because little research has been done so far on the vibration-assisted machining of soft-brittle materials.

7.2.5. Workpiece chucking. A vacuum chuck or wax mounting is usually used to hold the workpiece for ultraprecision machining. However, it has been reported that vacuum suction deformation is an important error source affecting the fabricated form error of soft-brittle materials, and the magnitude of the error depends on vacuum suction pressure and datum figure accuracy [188]. Therefore, optimization of vacuum suction pressure and layout of vacuum suction positions based on datum figure accuracy, as well as compensation of the tool path are necessary for improving the form accuracy of the machined surface. Furthermore, vacuum chucking and wax mounting are only effective when holding a wafer with a large flat surface area to thickness ratio, but not suitable for holding a rod, such as optical microcavity [71], which has a large length-diameter ratio. In nano-cutting of a rod-shaped soft-brittle material, chatter vibration can occur due to the low stiffness of the material [69]. Obviously, rod-shaped soft-brittle materials cannot be clamped with a three-jaw universal chuck like that used in clamping steel rods. Therefore, developing a

clamping technique for turning rod-shaped soft-brittle materials is also needed. The workpiece unbalance, deflection, and surface scratch/contamination in the chucking stage are critical issues for ultraprecision machining soft-brittle materials.

7.2.6. Noncontact measurement. After obtaining a high-quality surface finish on soft-brittle materials, the workpiece must be carefully stored and prevented from generating scratches in the transportation process. However, there are occasions when the finished surface must come into contact with another object. For example, the contact measurement of surface topography, during which the probe will scan the workpiece surface in a contact mode, may cause scratches on the finished surface. Although some light interference-based non-contact measurements exist, the measurement range is relatively small. Contact measurement is still the primary method for measuring a large workpiece. How to avoid scratches in contact measurement or develop non-contact equipment for large-size workpiece measurement should be considered.

7.2.7. Process modeling. Some phenomena observed in machining soft-brittle materials, such as the reverse phase transformation in cutting ZnSe, and subsurface damages without amorphous phase in cutting CaF_2 and grinding CdZnTe, differ from those in machining hard-brittle materials. So far, there is no report of MD simulation revealing the process of reversible phase transformation in the machining of soft-brittle materials. Therefore, the new models for soft-brittle materials that have reliable interatomic force definition, proper types of bonding, and correct crystal structure are expected to be established, and thus accurately describe the constitutive variations of the atomic structures of the soft-brittle materials. This will help illuminate the subsurface defect formation and phase changes of soft-brittle materials at the atomic scale through MDs simulation.

ORCID iDs

Weihai Huang https://orcid.org/0000-0003-3918-3644
Jiwang Yan https://orcid.org/0000-0002-5155-3604

References

[1] Ohmori H and Nakagawa T 1995 Analysis of mirror surface generation of hard and brittle materials by ELID (electronic in-process dressing) grinding with superfine grain metallic bond wheels *CIRP Ann.* **44** 287–90
[2] Agarwal S and Rao P V 2008 Experimental investigation of surface/subsurface damage formation and material removal mechanisms in SiC grinding *Int. J. Mach. Tools Manuf.* **48** 698–710
[3] Li C, Piao Y, Meng B B, Hu Y X, Li L Q and Zhang F H 2022 Phase transition and plastic deformation mechanisms induced by self-rotating grinding of GaN single crystals *Int. J. Mach. Tools Manuf.* **172** 103827
[4] Santailler J L *et al* 2020 From 5" CdZnTe ingots to high quality (111) CdZnTe substrates for SWIR 2K2 15 μm pitch infrared focal plane arrays manufacturing *Proc. SPIE* **11407** 114070G
[5] Szeles C 2004 Advances in the crystal growth and device fabrication technology of CdZnTe room temperature radiation detectors *IEEE Trans. Nucl. Sci.* **51** 1242–9
[6] Dwivedi A D D 2011 Analytical modeling and numerical simulation of P^{+}-$Hg_{0.69}Cd_{0.31}Te$/n-$Hg_{0.78}Cd_{0.22}Te$/CdZnTe heterojunction photodetector for a long-wavelength infrared free space optical communication system *J. Appl. Phys.* **110** 043101
[7] Gavrishchuk E M and Yashina É V 2004 Zinc sulfide and zinc selenide optical elements for IR engineering *J. Opt. Technol.* **71** 822–7
[8] Chen W Q, Liang Y C, Luo X C, Sun Y Z and Wang H R 2014 Multi-scale surface simulation of the KDP crystal fly cutting machining *Int. J. Adv. Manuf. Technol.* **73** 289–97
[9] Li Y, Kang R K, Gao H, Wang J H and Lang Y J 2009 Nanomechanical behaviors of (110) and (111) CdZnTe crystals investigated by nanoindentation *Rare Met.* **28** 570–5
[10] Broult T, Kerlain A, Destefanis V, Guinedor P, Bourhis E L and Patriarche G 2021 Development of a cryogenic indentation tool with *in situ* optical observation, application to the mechanical characterization of II–VI semiconductors *Semicond. Sci. Technol.* **36** 035015
[11] Irwan R, Huang H, Zheng H Y and Wu H 2013 Mechanical properties and material removal characteristics of soft-brittle HgCdTe single crystals *Mater. Sci. Eng.* A **559** 480–5
[12] Lei W, Antoszewski J and Faraone L 2015 Progress, challenges, and opportunities for HgCdTe infrared materials and detectors *Appl. Phys. Rev.* **2** 041303
[13] Deadmore D L and Sliney H E 1987 Hardness of CaF_2 and BaF_2 Solid Lubricants at 25–670 °C *NASA Technical Memorandum 88979* (Cleveland, Ohio)
[14] Schultz R A, Jensen M C and Bradt R C 1994 Single crystal cleavage of brittle materials *Int. J. Fract.* **65** 291–312
[15] Hahn D 2014 Calcium fluoride and barium fluoride crystals in optics *Opt. Photon.* **9** 45–48
[16] Grillo S E, Ducarroir M, Nadal M, Tourni E and Faurie J P 2002 Nanoindentation of Si, GaP, GaAs and ZnSe single crystals *J. Phys. D: Appl. Phys.* **36** L5–9
[17] Huang W H and Yan J W 2020 Surface formation mechanism in ultraprecision diamond turning of coarse-grained polycrystalline ZnSe *Int. J. Mach. Tools Manuf.* **153** 103554
[18] Fang T and Lambropoulos J C 2002 Microhardness and indentation fracture of potassium dihydrogen phosphate (KDP) *J. Am. Ceram. Soc.* **85** 174–8
[19] Mizumoto Y, Aoyama T and Kakinuma Y 2011 Basic study on Ultraprecision machining of single-crystal calcium fluoride *Proc. Eng.* **19** 264–9
[20] Julie L L, James J P, John D H and William R R 2005 Hardness, elastic modulus, and fracture toughness bulk properties in corning calcium fluoride *Proc. SPIE* **5754** 1329–38
[21] Canon Optron, Inc 2021 Products CaF2 (fluorite) (available at: https://optron.canon/en/fluorite/products_caf2.html)
[22] Lawn B R and Marshall D B 1979 Hardness, toughness, and brittleness: an indentation analysis *J. Am. Ceram. Soc.* **62** 347–50
[23] Zong W J, Cao Z M, He C L and Xue C X 2016 Theoretical modelling and FE simulation on the oblique diamond turning of ZnS crystal *Int. J. Mach. Tools Manuf.* **100** 55–71
[24] Aldabib J M and Ishak Z A M 2020 Effect of hydroxyapatite filler concentration on mechanical properties of poly (methyl methacrylate) denture base *SN Appl. Sci.* **2** 732
[25] Khadraoui S, Hachemi M, Allal A, Rabiei M, Arabi A, Khodja M, Lebouachera S E I and Drouiche N 2021 Numerical and experimental investigation of hydraulic

fracture using the synthesized PMMA *Polym. Bull.* **78** 3803–20
[26] Mukaida M and Yan J W 2017 Ductile machining of single-crystal silicon for microlens arrays by ultraprecision diamond turning using a slow tool servo *Int. J. Mach. Tools Manuf.* **115** 2–14
[27] Giredmet Company. CdZnTe substrate (available at: https://giredmet.ru/ru/production/podlozhki-cdznte/)
[28] Sumitomo Electric Industries, Ltd ZnSe lens (available at: www.sumitool.com/products/laser-optics/co2laser/lens.html)
[29] Canon Optron, Inc History of fluorite lenses (available at: https://optron.canon/ja/domain/fluorite/history.html)
[30] Zhang Y, Hou N and Zhang L C 2020 Effect of ultra-precision fly-cutting on the surface integrity of potassium dihydrogen phosphate crystals *Opt. Mater. Express* **10** 971–80
[31] Fang F Z and Chen L J 2000 Ultra-precision cutting for ZKN7 glass *CIRP Ann.* **49** 17–20
[32] Yan J W, Asami T, Harada H and Kuriyagawa T 2009 Fundamental investigation of subsurface damage in single crystalline silicon caused by diamond machining *Precis. Eng.* **33** 378–86
[33] Antwi E K, Liu K and Wang H 2018 A review on ductile mode cutting of brittle materials *Front. Mech. Eng.* **13** 251–63
[34] Huang H, Li X L, Mu D K and Lawn B R 2021 Science and art of ductile grinding of brittle solids *Int. J. Mach. Tools Manuf.* **161** 103675
[35] You K Y, Yan G P, Luo X C, Gilchrist M D and Fang F Z 2020 Advances in laser assisted machining of hard and brittle materials *J. Manuf. Process.* **58** 677–92
[36] Wang J J, Zhang J F, Feng P F and Guo P 2018 Damage formation and suppression in rotary ultrasonic machining of hard and brittle materials: a critical review *Ceram. Int.* **44** 1227–39
[37] Lawn B R, Borrero-Lopez O, Huang H and Zhang Y 2021 Micromechanics of machining and wear in hard and brittle materials *J. Am. Ceram. Soc.* **104** 5–22
[38] Zhang T, Jiang F, Huang H, Lu J, Wu Y Q, Jiang Z Y and Xu X P 2021 Towards understanding the brittle–ductile transition in the extreme manufacturing *Int. J. Extreme Manuf.* **3** 022001
[39] Zhang B and Yin J F 2019 The 'skin effect' of subsurface damage distribution in materials subjected to high-speed machining Int. *J. Extreme Manuf.* **1** 012007
[40] Guo X G, Li Q, Liu T, Kang R K, Jin Z J and Guo D M 2017 Advances in molecular dynamics simulation of ultra-precision machining of hard and brittle materials *Front. Mech. Eng.* **12** 89–98
[41] Goel S, Luo X C, Agrawal A and Reuben R L 2015 Diamond machining of silicon: a review of advances in molecular dynamics simulation *Int. J. Mach. Tools Manuf.* **88** 131–64
[42] Zhu W L and Beaucamp A 2020 Compliant grinding and polishing: a review *Int. J. Mach. Tools Manuf.* **158** 103634
[43] Luo H, Ajmal K M, Liu W, Yamamura K and Deng H 2021 Polishing and planarization of single crystal diamonds: state-of-the-art and perspectives *Int. J. Extreme Manuf.* **3** 022003
[44] Qu M N, Xie G Z, Jin T, Cai R and Lu A G 2019 Realization of high efficiency and low damage machining of anisotropic KDP crystal by grinding *Precis. Eng.* **55** 464–73
[45] Zhang Y, Hou N and Zhang L C 2019 Understanding the formation mechanism of subsurface damage in potassium dihydrogen phosphate crystals during ultra-precision fly cutting *Adv. Manuf.* **7** 270–7
[46] Zhang Z Y, Xu C G, Zhang X Z and Guo D M 2012 Mechanical characteristics of nanocrystalline layers containing nanotwins induced by nanogrinding of soft-brittle CdZnTe single crystals *Scr. Mater.* **67** 392–5
[47] Wang S F, An C H, Zhang F H, Wang J, Lei X Y and Zhang J F 2016 An experimental and theoretical investigation on the brittle ductile transition and cutting force anisotropy in cutting KDP crystal *Int. J. Mach. Tools Manuf.* **106** 98–108
[48] Azami S, Kudo H, Mizumoto Y, Tanabe T, Yan J W and Kakinuma Y 2015 Experimental study of crystal anisotropy based on ultra-precision cylindrical turning of single-crystal calcium fluoride *Precis. Eng.* **40** 172–81
[49] Yao L X, Zhang L, Jiang Q Q and Yang C F 2020 Prediction of critical undeformed chip thickness for ductile mode to brittle transition in the cutting of single-crystal silicon *Semicond. Sci. Technol.* **35** 095010
[50] Gao H, Wang X, Guo D M and Chen Y C 2017 Research progress on ultra-precision machining technologies for soft-brittle crystal materials *Front. Mech. Eng.* **12** 77–88
[51] Momma K and Izumi F 2011 VESTA3 for three-dimensional visualization of crystal, volumetric and morphology data *J. Appl. Crystallogr.* **44** 1272–6
[52] Hou Z B and Komanduri R 2003 On the mechanics of the grinding process—part I. Stochastic nature of the grinding process *Int. J. Mach. Tools Manuf.* **43** 1579–93
[53] Kumar S, Tong Z and Jiang X Q 2022 Advances in the design and manufacturing of novel freeform optics *Int. J. Extreme Manuf.* **4** 032004
[54] Zhou T F, He Y P, Wang T X, Zhu Z C, Xu R Z, Yu Q, Zhao B, Zhao W X, Liu P and Wang X B 2021 A review of the techniques for the mold manufacturing of micro/nanostructures for precision glass molding *Int. J. Extreme Manuf.* **3** 042002
[55] Nagayama K and Yan J W 2021 Deterministic error compensation for slow tool servo-driven diamond turning of freeform surface with nanometric form accuracy *J. Manuf. Process.* **64** 45–57
[56] Yan J W, Tamaki J, Syoji K and Kuriyagawa T 2004 Ductile regime machining of single-crystal CaF_2 for aspherical lenses *Key Eng. Mater.* **257–258** 95–100
[57] Chen Y H, Sun L H and Wu Y B 2022 Improving the machining performance in single-point diamond turning of curved Zerodur optics by using straight-nosed cutting tools *J. Mater. Process. Technol.* **310** 117777
[58] Jasinevicius R G, Duduch J G, Cirino G A and Pizani P S 2013 Diamond turning of small Fresnel lens array in single crystal InSb *J. Micromech. Microeng.* **23** 055025
[59] Gao X, Xue C X, Chao Y and Liu Y 2021 Optimization method of manufacturing for diamond turning soft-brittle materials' harmonic diffractive optical elements *Appl. Opt.* **60** 162–71
[60] Yan J W, Maekawa K, Tamaki J and Kuriyagawa T 2005 Micro grooving on single-crystal germanium for infrared Fresnel lenses *J. Micromech. Microeng.* **15** 1925–31
[61] Blake P N and Scattergood R O 1990 Ductile-regime machining of germanium and silicon *J. Am. Ceram. Soc.* **73** 949–57
[62] Heidari M, Akbari J and Yan J W 2019 Effects of tool rake angle and tool nose radius on surface quality of ultraprecision diamond-turned porous silicon *J. Manuf. Process.* **37** 321–31
[63] Ohta T, Yan J W, Yajima S, Takahashi Y, Horikawa N and Kuriyagawa T 2007 High-efficiency machining of single-crystal germanium using large-radius diamond tools *Int. J. Surf. Sci. Eng.* **1** 374–92
[64] Fuchs B A, Hed P P and Baker P C 1986 Fine diamond turning of KDP crystals *Appl. Opt.* **25** 1733–5

[65] Zong W J, Li Z Q, Zhang L, Liang Y C, Sun T, An C H, Zhang J F, Zhou L and Wang J 2013 Finite element simulation of diamond tool geometries affecting the 3D surface topography in fly cutting of KDP crystals *Int. J. Adv. Manuf. Technol.* **68** 1927–36

[66] Huang W H and Yan J W 2021 Effect of tool shape on the machined surface integrity of polycrystalline ZnSe *In Proc. 21st Int. Conf. European Society for Precision Engineering and Nanotechnology, EUSPEN 2021* (EUSPEN) pp 387–90 (available at: www.euspen.eu/knowledge-base/ICE21236.pdf)

[67] Xiao H P, Liang R G, Spires O, Wang H R, Wu H and Zhang Y Y 2019 Evaluation of surface and subsurface damages for diamond turning of ZnSe crystal *Opt. Express* **27** 28364–82

[68] Geng R W, Yang X J, Xie Q M, Zhang W Q, Kang J, Liang Y Q and Li R 2021 Ultra-precision diamond turning of ZnSe ceramics: surface integrity and ductile regime machining mechanism *Infrared Phys. Technol.* **115** 103706

[69] Kakinuma Y, Azami S and Tanabe T 2015 Evaluation of subsurface damage caused by ultra-precision turning in fabrication of CaF_2 optical micro resonator *CIRP Ann.* **64** 117–20

[70] Mizumoto Y, Kangawa H, Nakagawa Y, Itobe H, Tanabe T and Kakinuma Y 2016 Influence of nose radius on surface integrity in ultra-precision cylindrical turning of single-crystal calcium fluoride *Proc. CIRP* **45** 139–42

[71] Mizumoto Y, Kangawa H, Itobe H, Tanabe T and Kakinuma Y 2017 Influence of crystal anisotropy on subsurface damage in ultra-precision cylindrical turning of CaF_2 *Precis. Eng.* **49** 104–14

[72] Yan J 2011 Ultraprecision cutting of photoresist/gold composite microstructures *CIRP Ann.* **60** 133–6

[73] Mahajan K A, Pawade R S and Mishra V 2022 Tool vibration effect on surface roughness of polymethylmethacrylate in diamond turning *Mater. Manuf. Process.* **37** 271–82

[74] Bodlapati C, Dow T, Wong A and Garrard K 2018 Surface finish and diamond tool wear when machining PMMA and PC optics *Proc. SPIE* **10742** 107420D

[75] Yan J W, Syoji K and Tamaki J I 2004 Crystallographic effects in micro/nanomachining of single-crystal calcium fluoride *J. Vac. Sci. Technol.* B **22** 46–51

[76] Yan J W, Syoji K, Kuriyagawa T and Suzuki H 2002 Ductile regime turning at large tool feed *J. Mater. Process. Technol.* **121** 363–72

[77] Yan J W, Tamaki J I, Syoji K and Kuriyagawa T 2004 Single-point diamond turning of CaF_2 for nanometric surface *Int. J. Adv. Manuf. Technol.* **24** 640–6

[78] Huang W H and Yan J W 2021 Fundamental investigation of diamond cutting of micro V-shaped grooves on a polycrystalline soft-brittle material *J. Manuf. Mater. Process.* **5** 17

[79] Lee Y J, Senthil Kumar A and Wang H 2021 Beneficial stress of a coating on ductile-mode cutting of single-crystal brittle material *Int. J. Mach. Tools Manuf.* **168** 103787

[80] Wang H, Riemer O, Rickens K and Brinksmeier E 2016 On the mechanism of asymmetric ductile–brittle transition in microcutting of (111) CaF_2 single crystals *Scr. Mater.* **114** 21–26

[81] Fang F Z and Xu F F 2018 Recent advances in micro/nano-cutting: effect of tool edge and material properties *Nanomanuf. Metrol.* **1** 4–31

[82] Rahman M A, Amrun M R, Rahman M and Kumar A S 2017 Variation of surface generation mechanisms in ultra-precision machining due to relative tool sharpness (RTS) and material properties *Int. J. Mach. Tools Manuf.* **115** 15–28

[83] Xie W K and Fang F Z 2020 Effect of tool edge radius on material removal mechanism in atomic and close-to-atomic scale cutting *Appl. Surf. Sci.* **504** 144451

[84] Yan J W, Zhao H W and Kuriyagawa T 2009 Effects of tool edge radius on ductile machining of silicon: an investigation by FEM *Semicond. Sci. Technol.* **24** 075018

[85] Ameli Kalkhoran S N, Vahdati M and Yan J W 2020 Effect of relative tool sharpness on subsurface damage and material recovery in nanometric cutting of mono-crystalline silicon: a molecular dynamics approach *Mater. Sci. Semicond. Process.* **108** 104868

[86] Fang F Z, Wu H and Liu Y C 2005 Modelling and experimental investigation on nanometric cutting of monocrystalline silicon *Int. J. Mach. Tools Manuf.* **45** 1681–6

[87] Chen M J, Jiang W B and Li M Q 2011 Effects of tool edge radius and rake angle on ductile machining process of CaF_2 *Int. J. Nanomanuf.* **7** 350–60

[88] Zhang S and Zong W J 2020 Micro defects on diamond tool cutting edge affecting the ductile-mode machining of KDP crystal *Micromachines* **11** 1102

[89] Liu Q, Liao Z R, Cheng J, Xu D D and Chen M J 2021 Mechanism of chip formation and surface-defects in orthogonal cutting of soft-brittle potassium dihydrogen phosphate crystals *Mater. Des.* **198** 109327

[90] Yan J W, Asami T, Harada H and Kuriyagawa T 2012 Crystallographic effect on subsurface damage formation in silicon microcutting *CIRP Ann.* **61** 131–4

[91] Chen X, Xu J F, Fang H S and Tian R J 2017 Influence of cutting parameters on the ductile-brittle transition of single-crystal calcium fluoride during ultra-precision cutting *Int. J. Adv. Manuf. Technol.* **89** 219–25

[92] Zhang S, Zhang H J and Zong W J 2019 Modeling and simulation on the effect of tool rake angle in diamond turning of KDP crystal *J. Mater. Process. Technol.* **273** 116259

[93] Chen M J, Wang J H, Liang Y C and Yuan D Y 2007 Research on influence of the cutter rake angle to the surface quality during SPDT machining of crystal KDP *Key Eng. Mater.* **339** 1–5

[94] Zhou T F, Ruan B S, Zhou J, Dong X B, Liang Z Q and Wang X B 2019 Mechanism of brittle fracture in diamond turning of microlens array on polymethyl methacrylate *Adv. Manuf.* **7** 228–37

[95] Fang F Z, Venkatesh V C and Zhang G X 2002 Diamond turning of soft semiconductors to obtain nanometric mirror surfaces *Int. J. Adv. Manuf. Technol.* **19** 637–41

[96] Yan J W, Zhang Z Y, Kuriyagawa T and Gonda H 2010 Fabricating micro-structured surface by using single-crystalline diamond endmill *Int. J. Adv. Manuf. Technol.* **51** 957–64

[97] Matsumura T 2018 Micro milling for functional surface *Micro and Nano Fabrication Technology* 1st edn ed J W Yan Micro/Nano Technologies (Singapore: Springer) pp 1–34

[98] Chen N, Li H N, Wu J M, Li Z J, Li L, Liu G Y and He N 2021 Advances in micro milling: from tool fabrication to process outcomes *Int. J. Mach. Tools Manuf.* **160** 103670

[99] Fang F Z, Wu H, Liu X D, Liu Y C and Ng S T 2003 Tool geometry study in micromachining *J. Micromech. Microeng.* **13** 726–31

[100] Chen N, Chen M J, Wu C Y, Pei X D, Qian J and Reynaerts D 2017 Research in minimum undeformed chip thickness and size effect in micro end-milling of potassium dihydrogen phosphate crystal *Int. J. Mech. Sci.* **134** 387–98

[101] Arif M, Rahman M and San W Y 2011 Ultraprecision ductile mode machining of glass by micromilling process *J. Manuf. Process.* **13** 50–59

[102] Rusnaldy N, Ko T J and Kim H S 2007 Micro-end-milling of single-crystal silicon *Int. J. Mach. Tools Manuf.* **47** 2111–9

[103] Oliaei S N B and Karpat Y 2018 Polycrystalline diamond end mill cutting edge design to improve ductile-mode machining of silicon *Precis. Eng.* **51** 403–14

[104] Xiao Y, Chen M J, Yang Y T and Cheng J 2015 Research on the critical condition of brittle-ductile transition about micro-milling of KDP crystal and experimental verification *Int. J. Precis. Eng. Manuf.* **16** 351–9

[105] Ono T and Matsumura T 2008 Influence of tool inclination on brittle fracture in glass cutting with ball end mills *J. Mater. Process. Technol.* **202** 61–69

[106] Foy K, Wei Z, Matsumura T and Huang Y 2009 Effect of tilt angle on cutting regime transition in glass micromilling *Int. J. Mach. Tools Manuf.* **49** 315–24

[107] Aurich J C, Reichenbach I G and Schüler G M 2012 Manufacture and application of ultra-small micro end mills *CIRP Ann.* **61** 83–86

[108] Choong Z J, Huo D H, Degenaar P and O'Neill A 2019 Micro-machinability and edge chipping mechanism studies on diamond micro-milling of monocrystalline silicon *J. Manuf. Process.* **38** 93–103

[109] Huo D H, Lin C, Choong Z J, Pancholi K and Degenaar P 2015 Surface and subsurface characterisation in micro-milling of monocrystalline silicon *Int. J. Adv. Manuf. Technol.* **81** 1319–31

[110] Liu Q, Cheng J, Liao Z R, Yang H, Zhao L J and Chen M J 2019 Incident laser modulation by tool marks on micro-milled KDP crystal surface: numerical simulation and experimental verification *Opt. Laser Technol.* **119** 105610

[111] Chen N, Chen M J, Guo Y Q and Wang X B 2015 Effect of cutting parameters on surface quality in ductile cutting of KDP crystal using self-developed micro PCD ball end mill *Int. J. Adv. Manuf. Technol.* **78** 221–9

[112] Spaeth M L *et al* 2016 Optics recycle loop strategy for NIF operations above UV laser-induced damage threshold *Fusion Sci. Technol.* **69** 265–94

[113] Liu Q, Cheng J, Yang H, Xu Y F, Zhao L J, Tan C and Chen M J 2019 Modeling of residual tool mark formation and its influence on the optical performance of KH_2PO_4 optics repaired by micro-milling *Opt. Mater. Express* **9** 3789–807

[114] Ali M Y and Ong A S 2006 Fabricating micromilling tool using wire electrodischarge grinding and focused ion beam sputtering *Int. J. Adv. Manuf. Technol.* **31** 501–8

[115] Yan J W, Uchida K, Yoshihara N and Kuriyagawa T 2009 Fabrication of micro end mills by wire EDM and some micro cutting tests *J. Micromech. Microeng.* **19** 025004

[116] Zhang Z Y, Peng H M and Yan J W 2013 Micro-cutting characteristics of EDM fabricated high-precision polycrystalline diamond tools *Int. J. Mach. Tools Manuf.* **65** 99–106

[117] Chen N, Chen M J, Wu C Y and Pei X D 2017 Cutting surface quality analysis in micro ball end-milling of KDP crystal considering size effect and minimum undeformed chip thickness *Precis. Eng.* **50** 410–20

[118] O'Toole L, Kang C W and Fang F Z 2021 Precision micro-milling process: state of the art *Adv. Manuf.* **9** 173–205

[119] Chen N, Chen M J, Wu C Y, Guo Y Q and Wang Y N 2016 The design and optimization of micro polycrystalline diamond ball end mill for repairing micro-defects on the surface of KDP crystal *Precis. Eng.* **43** 345–55

[120] Yan Y, Zhou P, Wang H P and Mao Y 2020 Thermal effect on poly(methyl methacrylate) (PMMA) material removal in the micromilling process *Polymers* **12** 2122

[121] Ali M Y, Khan A A, Mohamad Asharaf A B and Abdul Wahab A 2012 Prediction of minimum chip thickness in tool based micro end milling *Int. J. Integr. Eng.* **4** 6–10 (available at: https://publisher.uthm.edu.my/ojs/index.php/ijie/article/view/147)

[122] Son S M, Lim H S and Ahn J H 2005 Effects of the friction coefficient on the minimum cutting thickness in micro cutting *Int. J. Mach. Tools Manuf.* **45** 529–35

[123] Chen N, Li L, Wu J M, Qian J, He N and Reynaerts D 2019 Research on the ploughing force in micro milling of soft-brittle crystals *Int. J. Mech. Sci.* **155** 315–22

[124] Korkmaz E, Onler R and Ozdoganlar O B 2017 Micromilling of poly(methyl methacrylate, PMMA) using single-crystal diamond tools *Proc. Manuf.* **10** 683–93

[125] Cheng X, Wang Z G, Nakamoto K and Yamazaki K 2010 Design and development of PCD micro straight edge end mills for micro/nano machining of hard and brittle materials *J. Mech. Sci. Technol.* **24** 2261–8

[126] Cheng X, Wang Z G, Nakamoto K and Yamazaki K 2009 Design and development of a micro polycrystalline diamond ball end mill for micro/nano freeform machining of hard and brittle materials *J. Micromech. Microeng.* **19** 115022

[127] Uchiyama R, Inoue Y, Uchiyama F and Matsumura T 2021 Optimization in milling of polymer materials for high quality surfaces *Int. J. Autom. Technol.* **15** 512–20

[128] Ko T J, Kim H S and Lee S S 2001 Selection of the machining inclination angle in high-speed ball end milling *Int. J. Adv. Manuf. Technol.* **17** 163–70

[129] Liu Q, Cheng J, Xiao Y, Yang H and Chen M J 2018 Effect of milling modes on surface integrity of KDP crystal processed by micro ball-end milling *Proc. CIRP* **71** 260–6

[130] Liu Q, Cheng J, Xiao Y, Chen M J, Yang H and Wang J H 2018 Effect of tool inclination on surface quality of KDP crystal processed by micro ball-end milling *Int. J. Adv. Manuf. Technol.* **99** 2777–88

[131] Matsumura T and Ono T 2008 Cutting process of glass with inclined ball end mill *J. Mater. Process. Technol.* **200** 356–63

[132] Zhang Z Y, Yan J W and Kuriyagawa T 2019 Manufacturing technologies toward extreme precision *Int. J. Extreme Manuf.* **1** 022001

[133] Namba Y, Yoshida K, Yoshida H and Nakai S 1998 Ultraprecision grinding of optical materials for high-power lasers *Proc. SPIE* **3244** 320–30

[134] Katagiri M and Namba Y 1999 Optical surface generation of KDP inorganic nonlinear optical crystals by ultraprecision surface grinding *J. Japan Soc. Precis. Eng.* **65** 888–92

[135] Qu M N, Jin T, Xie G Z and Cai R 2020 Developing a novel binderless diamond grinding wheel with femtosecond laser ablation and evaluating its performance in grinding soft and brittle materials *J. Mater. Process. Technol.* **275** 116359

[136] Qu M N, Jin T, Xie G Z, Cai R and Lu A G 2020 Design of binderless grinding wheel with positive rake angle and fabrication used femtosecond laser ablation for grinding soft and brittle crystals *Opt. Lasers Eng.* **124** 105803

[137] Wang Q G, Gao H, Zhang Q Z, Cao X S and Kang R K 2008 Experimental researches on precision grinding of KDP crystal *Key Eng. Mater.* **359–360** 113–7

[138] Namba Y, Yoshida T, Yoshida S, Yoshida K and Iwata K 2005 Surfaces of calcium fluoride single crystals ground with an ultra-precision surface grinder *CIRP Ann.* **54** 503–6

[139] Zhang Z Y, Meng Y W, Guo D M, Wu L L, Tian Y J and Liu R P 2010 Material removal mechanism of precision

grinding of soft-brittle CdZnTe wafers *Int. J. Adv. Manuf. Technol.* **46** 563–9
[140] Zhang Z Y, Wu Y Q and Huang H 2010 New deformation mechanism of soft-brittle CdZnTe single crystals under nanogrinding *Scr. Mater.* **63** 621–4
[141] Wang Y, Zou J, Huang H, Zhou L, Wang B L and Wu Y Q 2007 Formation mechanism of nanocrystalline high-pressure phases in silicon during nanogrinding *Nanotechnology* **18** 465705
[142] Gao S, Wu Y Q, Kang R K and Huang H 2018 Nanogrinding induced surface and deformation mechanism of single crystal β-Ga_2O_3 *Mater. Sci. Semicond. Process.* **79** 165–70
[143] Zhang Z Y, Zhang X Z, Xu C G and Guo D M 2013 Characterization of nanoscale chips and a novel model for face nanogrinding on soft-brittle HgCdTe films *Tribol. Lett.* **49** 203–15
[144] Zhang Z Y, Song Y X, Xu C G and Guo D M 2012 A novel model for undeformed nanometer chips of soft-brittle HgCdTe films induced by ultrafine diamond grits *Scr. Mater.* **67** 197–200
[145] Zhang Z Y, Song Y X, Huo F W and Guo D M 2012 Nanoscale material removal mechanism of soft-brittle HgCdTe single crystals under nanogrinding by ultrafine diamond grits *Tribol. Lett.* **46** 95–100
[146] Lawn B 1993 *Fracture of Brittle Solids* 2nd edn (Cambridge: Cambridge University Press)
[147] Suratwala T, Steele R, Shen N, Ray N, Wong L, Miller P E and Feit M 2020 Lateral cracks during sliding indentation on various optical materials *J. Am. Ceram. Soc.* **103** 1343–57
[148] Hou N, Zhang Y, Zhang L C and Wang M H 2021 Material removal mechanisms and characteristics of potassium dihydrogen phosphate crystals under nanoscratching *Adv. Manuf.* **9** 558–67
[149] Zhang Y, Zhang L C, Liu M, Zhang F H, Mylvaganam K and Liu W D 2015 Understanding the friction and wear of KDP crystals by nanoscratching *Wear* **332–333** 900–6
[150] Rahaman M L and Zhang L C 2021 An investigation on the friction, wear and deformation of potassium dihydrogen phosphate *Wear* **476** 203624
[151] Li C, Zhang Y, Zhou G Z, Wei Z J and Zhang L C 2020 Theoretical modelling of brittle-to-ductile transition load of KDP crystals on (001) plane during nanoindentation and nanoscratch tests *J. Mater. Res. Technol.* **9** 14142–57
[152] Axinte D, Butler-Smith P, Akgun C and Kolluru K 2013 On the influence of single grit micro-geometry on grinding behavior of ductile and brittle materials *Int. J. Mach. Tools Manuf.* **74** 12–18
[153] Zhou H X, Qiu S, Zhang X Z and Xu C G 2012 Mechanical characteristics of soft-brittle HgCdTe single crystals investigated using nanoindentation and nanoscratching *Appl. Surf. Sci.* **258** 9756–61
[154] Li Y, Kang R K, Gao H and Wu D J 2010 Effect of mechanical anisotropy on grinding of CdZnTe wafers *Mater. Manuf. Process.* **25** 412–7
[155] Yang S Y, Zhang L C and Wu Z H 2021 An investigation on the nano-abrasion wear mechanisms of KDP crystals *Wear* **476** 203692
[156] Yang S Y, Zhang L C, Xie H T and Liu W D 2021 Interaction potential function for the deformation analysis of potassium dihydrogen phosphate using molecular dynamics simulation *Comput. Mater. Sci.* **187** 110122
[157] Zhang C L, Feng P F and Wang D 2012 The effect of crystallographic orientation on material removal behavior of (001) plane KDP crystal in nano-scratch test Proc. ASME 2012 Int. Mechanical Engineering Congress and Exposition. Volume 3: Design, Materials and Manufacturing, Parts A, B, and C (Houston, Texas, USA, 9–15 November 2012) (New York: ASME) pp 1883–9
[158] Liu Q, Liao Z R and Axinte D 2020 Temperature effect on the material removal mechanism of soft-brittle crystals at nano/micron scale *Int. J. Mach. Tools Manuf.* **159** 103620
[159] Chen L, Hu L C, Xiao C, Qi Y Q, Yu B J and Qian L M 2017 Effect of crystallographic orientation on mechanical removal of CaF_2 *Wear* **376–377** 409–16
[160] Wu Y Q, Huang H and Zou J 2011 Transmission electron microscopy characterization of the deformation of CdZnTe single crystals induced by nanoscratching *Scr. Mater.* **65** 392–5
[161] Huang W H and Yan J W 2021 Deformation behaviour of soft-brittle polycrystalline materials determined by nanoscratching with a sharp indenter *Precis. Eng.* **72** 717–29
[162] Zhang S H, Guo X G, Jin Z J, Kang R K and Guo D M 2020 Material removal characteristics of precorroded Lu_2O_3 laser crystals and elastic deformation model during nanoscratch process *Tribol. Int.* **143** 106027
[163] Huang L, Bonifacio C, Song D, Benthem K V, Mukherjee A K and Schoenung J M 2011 Investigation into the microstructure evolution caused by nanoscratch-induced room temperature deformation in M-plane sapphire *Acta Mater.* **59** 5181–93
[164] Li C, Zhang F H, Wu Y Q and Zhang X 2018 Influence of strain rate effect on material removal and deformation mechanism based on ductile nanoscratch tests of Lu_2O_3 single crystal *Ceram. Int.* **44** 21486–98
[165] Li C, Zhang F H and Piao Y 2019 Strain-rate dependence of surface/subsurface deformation mechanisms during nanoscratching tests of GGG single crystal *Ceram. Int.* **45** 15015–24
[166] LTS Research Laboratories, Inc 2021 Safety data sheet cadmium zinc tellurium (available at: www.ltschem.com/msds/CdZnTe.pdf)
[167] The Toxin and Toxin Target Database 2021 Mercury cadmium telluride (T3D0347) (available at: http://www.t3db.ca/toxins/T3D0347)
[168] National Center for Biotechnology Information 2022 PubChem compound summary for CID 62670, barium fluoride (available at: https://pubchem.ncbi.nlm.nih.gov/compound/Barium-fluoride)
[169] National Center for Biotechnology Information 2022 PubChem compound summary for CID 4298215, zinc selenide (ZnSe) (available at: https://pubchem.ncbi.nlm.nih.gov/compound/Zinc-selenide-_ZnSe)
[170] National Center for Biotechnology Information 2022 PubChem compound summary for CID 516951, potassium dihydrogen phosphate (available at: https://pubchem.ncbi.nlm.nih.gov/compound/516951)
[171] National Center for Biotechnology Information 2022 PubChem compound summary for CID 84512, calcium fluoride (available at: https://pubchem.ncbi.nlm.nih.gov/compound/Calcium-fluoride)
[172] National Center for Biotechnology Information 2022 PubChem compound summary for CID 14821, zinc sulfide (available at: https://pubchem.ncbi.nlm.nih.gov/compound/ZINC-sulfide)
[173] Korzynski M 2007 Modeling and experimental validation of the force-surface roughness relation for smoothing burnishing with a spherical tool *Int. J. Mach. Tools Manuf.* **47** 1956–64
[174] Korzynski M, Lubas J, Swirad S and Dudek K 2011 Surface layer characteristics due to slide diamond burnishing with a cylindrical-ended tool *J. Mater. Process. Technol.* **211** 84–94
[175] Li F L, Xia W, Zhou Z Y, Zhao J and Tang Z Q 2012 Analytical prediction and experimental verification of

surface roughness during the burnishing process *Int. J. Mach. Tools Manuf.* **62** 67–75
[176] Teramachi A and Yan J W 2019 Improving the surface integrity of additive-manufactured metal parts by ultrasonic vibration-assisted burnishing *J. Micro Nano-Manuf.* **7** 024501
[177] Chueca De Bruijn A, Gómez-Gras G and Pérez M A 2021 On the effect upon the surface finish and mechanical performance of ball burnishing process on fused filament fabricated parts *Addit. Manuf.* **46** 102133
[178] Attabi S, Himour A, Laouar L and Motallebzadeh A 2021 Mechanical and wear behaviors of 316L stainless steel after ball burnishing treatment *J. Mater. Res. Technol.* **15** 3255–67
[179] Huang W H and Yan J W 2021 Chip-free surface patterning of toxic brittle polycrystalline materials through micro/nanoscale burnishing *Int. J. Mach. Tools Manuf.* **162** 103688
[180] Pu C, Dai L D, Li H P, Hu H Y, Liu K X, Yang L F and Hong M L 2019 Pressure-induced phase transitions of ZnSe under different pressure environments *AIP Adv.* **9** 025004
[181] Lai M, Zhang X D, Fang F Z and Bi M H 2017 Fundamental investigation on partially overlapped nano-cutting of monocrystalline germanium *Precis. Eng.* **49** 160–8
[182] Wang J S, Fang F Z and Zhang X D 2015 An experimental study of cutting performance on monocrystalline germanium after ion implantation *Precis. Eng.* **39** 220–3
[183] Fang F Z, Lai M, Wang J S, Luo X C, Yan J W and Yan Y D 2022 Nanometric cutting: mechanisms, practices and future perspectives *Int. J. Mach. Tools Manuf.* **178** 103905
[184] Xu W H *et al* 2022 Electrostatic atomization minimum quantity lubrication machining: from mechanism to application *Int. J. Extreme Manuf.* **4** 042003
[185] Kozlowski M R, Thomas I M, Edwards G J, Stanion K A, Fuchs B A and Latanich L 1991 Influence of diamond turning and surface cleaning processes on the degradation of KDP crystal surfaces *Proc. SPIE* **1561** 59–69
[186] Montesanti R C and Thompson S L 1995 A procedure for diamond turning KDP crystals *USDOE Economic Regulatory Administration* (Washington, DC) (https://doi.org/10.2172/105024)
[187] Li L H, Wong H C and Lee R B 2020 Evaluation of a novel nanodroplet cutting fluid for diamond turning of optical polymers *Polymers* **12** 2213
[188] Tie G, Dai Y F, Guan C L, Zhu D C and Song B 2013 Research on full-aperture ductile cutting of KDP crystals using spiral turning technique *J. Mater. Process. Technol.* **213** 2137–44